IMAGING PERFORMANCE OF SCANNING SLOT X-RAY DETECTORS FOR
DIGITAL MAMMOGRAPHY

By

ZHENXUE JING

A DISSERTATION PRESENTED TO THE GRADUATE SCHOOL
OF THE UNIVERSITY OF FLORIDA IN PARTIAL FULFILLMENT
OF THE REQUIREMENTS FOR THE DEGREE OF
DOCTOR OF PHILOSOPHY

UNIVERSITY OF FLORIDA

1997

Dedicated to Guoying, my wife, and Xiaoshan, my son –

for the happiness they bring to my life

ACKNOWLEDGMENTS

TABLE OF CONTENTS

LIST OF TABLES

LIST OF FIGURES

IMAGING PERFORMANCE OF SCANNING SLOT X-RAY DETECTORS FOR
DIGITAL MAMMOGRAPHY

By

Zhenxue Jing

May, 1997

Chairman: Walter Huda
Cochair: Edward V. Staab
Major Department: Nuclear and Radiological Engineering

Scanning slot x-ray imaging systems are currently under investigation for digital
mammography. Two main technical problems associated with a scanning slot
mammography system are the choice of the slot detector width which affects the presence
of scattered radiation and x-ray tube heating that may be associated with a particular
detector design, and the choice of x-ray detection material which places a limit on the
ultimate image quality which can be achieved. In this study, slot detector width was
optimized based on the presence of scattered radiation. It was found that scatter to
primary (S/P) ratios depend strongly on the slot detector width. The combination of a 10
mm slot detector width with a 3 cm air gap can provide both efficient scatter rejection and
efficient use of x-ray tube output. The typical x-ray detection material in the current
designs of scanning slot detectors is a rare earth phosphor (Gd_2O_2S:Tb) screen. The delay
in scintillation light emission from Gd_2O_2S:Tb phosphor causes a large spread of light

over the scanning direction thereby reducing spatial resolution. Two novel x-ray detection materials with very short scintillation decay time can be used to replace Gd_2O_2S:Tb phosphor. They are high Z element loaded plastic scintillating fiber screens (SFS) and a Thallium activated CsI screen (CsI:Tl) which has CsI crystals grown in a columnar structure like fiber. These fiber structures in scintillation screens permit the use of relatively thick screen to improve x-ray interaction efficiency without significantly sacrificing spatial resolution. In this study, the imaging performances of slot detectors using various SFSs and the CsI:Tl screen were investigated by theoretical analysis, Monte Carlo simulations, and experimental measurements. It was found that spatial resolution and detective quantum efficiency (DQE) of a slot detector based on a high Z element (tin or lead) loaded SFS exceed those of both CsI:Tl screen and Gd_2O_2S:Tb phosphor screen based slot detectors. Spatial resolution and DQE of the CsI:Tl screen based slot x-ray detector were also found to be higher than those when a Gd_2O_2S:Tb phosphor screen was used. Compared to a SFS, CsI:Tl screen based slot x-ray detector has higher image signal-to-noise ratio due to its higher energy conversion efficiency. Nevertheless, the use of either a high Z element loaded SFS or the CsI:Tl screen in scanning slot digital mammography could provide improved mammography imaging performance, and could play a role in increasing the accuracy of breast cancer detection and thereby reduce breast cancer mortality.

CHAPTER 1
INTRODUCTION

1.1. Background

1.1.1. Breast Cancer Screening

Breast cancer is the most common form of cancer and the second leading cause of cancer death for women in the United States (Sickles, 1985; Zhou and Gordon, 1989; Yaffe, 1992). In the past 15 years, approximately 150,000 U.S. women have been diagnosed with breast cancer each year, and about 30% of these women have died of this disease. It is estimated that approximately one in eight women (12.6%) will develop breast cancer in their lifetimes (Smith, 1995). There is very little knowledge about the causes of breast cancer. There are several risk factors are known to be associated with breast cancer. These factors include (1) having had a previous breast cancer; (2) laboratory evidence that a woman is carrying a specific mutation or genetic change that increases susceptibility to breast cancer; (3) in families in which multiple family members are affected with breast cancer; (4) having had a diagnosis of other types of breast disease; (5) with 75% or more dense breast tissue on previous mammograms that made mammography reading difficult; and (6) having a first birth at age 30 or older. However, approximately 60% of women diagnosed with breast cancer have none of these known factors.

In the absence of any way to prevent breast cancers, the only way to reduce this mortality lies in the application of broad-based, comprehensive programs for early detection. Screen-film mammography is the only reliable means of detecting nonpalpable

breast cancers at present (Haus, 1987, 1992). When breast cancer is detected earlier, treatment is not only more effective but potentially less disfiguring and toxic. Early detection with screening mammography has been shown to reduce breast cancer mortality rates by about 30% for women over age 50. Demonstration of proof of benefits from screening mammography has been more difficult in women 40 to 50 years of age than in older women. Seemingly conflicting results from screening trials have led to disagreement among experts as to the efficacy of screening before age 50 years. It is generally agreed that breast density is somewhat higher in younger women, potentially masking cancers, in which mammographic appearance is often subtle. Improved mammography imaging technique is necessary to ensure benefits of screening mammography in younger women (Feig and Hendrick, 1992). Recently available evidence from clinical studies indicates a reduction of 17% in breast cancer mortality after about 10 years for women ages 40 to 49.

Clinical requirements for early detection of breast cancer include detection of subtle architectural distortion, masses with densities very close to normal tissue and skin thickening. It is also important to detect microcalcifications which are specks of calcium hydroxyapatite $[Ca_5(PO_4)_3OH]$ that may have diameters as small as 0.1 mm. The importance of microcalcifications in the breast is linked to a large number of cancers detected by this sign and to the fact that due to this sign it is possible to find approximately 50% of noninvasive lesions (Feig, 1995).

In practice, the thickness of the compressed breast can be as large as 10 cm with a average value of about 5 cm. Breasts are mainly composed of adipose and fibroglandular tissues and these compositions vary widely. The fibroglandular tissue begins to develop at puberty and is gradually replaced by fat after maturity. This range of size and composition of the compressed breast places high demands on the screen-film systems (Skubic and Fatouros, 1989; Whitehouse and Leinster, 1985).

A mammography system should allow these detections as early as possible with a minimal exposure to the patient to reduce the risk of radiation induced carcinogenesis. This requires an optimized system with sufficient contrast sensitivity and signal-to-noise ratio (SNR) to image a wide range of lesion sizes (submillimeter to a few centimeters) over a wide range in exposure to the image receptor.

1.1.2. Screen-Film Mammography

Modern mammography is performed on a dedicated x-ray unit designed to allow easy examination of the breast. The patient is examined with her breast compressed against a supporting plate. Compression is applied using a plastic compression paddle to reduce the breast thickness and to hold the breast in position. Compression generally results in greater image sharpness, less scatter, and reduced patient dose (Logan and Norlund, 1979). The breast image is recorded using a screen-film combination contained within a radiographic cassette which is placed in a holder beneath the breast support. An anti-scatter grid is usually placed between the support and cassette to remove scattered radiation from reaching the screen. An automatic exposure control device (AEC) is generally located behind the cassette to permit the production of consistent optimal film optical density on the film. The x-ray tube and screen-film detector assembly are mounted on a support arm which can be rotated to achieve the desired radiographic projection.

In a mammographic x-ray unit, the x-ray field collimation and focal spot are arranged so that the field edge closest to the patient is vertical. The typical focal spot to screen-film detector distance is ~ 60 cm. Measured focal spot size is generally less than 0.5 mm to minimize geometric unsharpness due to focal spot blur. Because there are only small differences in x-ray attenuation between carcinoma and breast parenchyma (Jones and Yaffe, 1987), low x-ray energies about 20 keV are used in mammography to improve image contrast. The most frequently used x-ray spectrum is that output from a

molybdenum (Mo) anode with an added ~ 30 μm Mo filtration. The x-ray tube potential is typically operated in the range from 24 to 32 kV.

Modern mammography screen-film combinations are made of a single gadolinium oxysulphide rare earth phosphor screen (Gd_2O_2S:Tb) used as a back screen in combination with a single emulsion film (Haus, 1992), as shown in Figure 1-1. In this structure, high spatial resolution (~ 20 lp/mm) is achieved by three factors: (1) a thin layer of phosphor with thickness of the order of ~ 50 μm, (2) light absorption dye added in the phosphor layer, and (3) the number of absorbed x-ray photons decreases at increased depth into the phosphor. All three factors reduce the lateral dispersion of light within the phosphor and thereby maximize the achievable spatial resolution.
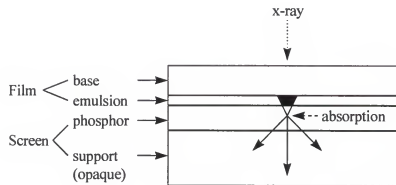
Figure 1-1. Structure of a modern mammography screen-film combination.

1.1.3. Limitations of Screen-Film Mammography

In practice, there are about 10 to 20% of breast cancers which are mis-diagnosed due to the subtlety of the lesion and the limitation of the image quality (Ma et al., 1992). One of the major contributing factors to poor image quality is related to the use of screen-film combinations, which have several technical problems that limit the effectiveness of screening mammography. The major technical limitation is related to the shape of the

film's characteristic curves which necessitate a fundamental compromise between the film's display contrast and exposure latitude (Haus, 1992; Nishikawa and Yaffe 1987). Figure 1-2 shows the characteristic curve of a typical mammography screen-film combination.
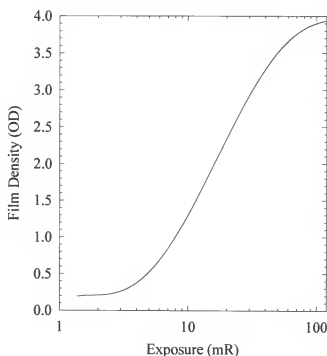
Figure 1-2. Characteristic curve of a typical mammography screen-film combination.

For mammography screen-film combinations, high film contrast is essential to detect subtle lesions with subject contrast in the order of ~1% or less. As a result, the exposure latitudes of conventional mammography screen-film combinations are limited to about 40. Typically, film contrast is about 3.5 for film densities ranging from about 1.0 to 2.0 which only corresponds to a change in x-ray exposure by a factor of about 2. Film contrast reduces quickly below the film optical density of 1.0 and above the film optical density of 2.0 (Haus, 1992). This compromise in film contrast and exposure latitude is optimized to image compressed breasts of average thickness and average density (~ 50%

adipose and 50% glandular tissue composition). It has been shown that a mammography imaging system should record and display information for detector exposures which vary over a factor of 400 in a single image (Maidment et al., 1993a). This is due to the large range in different breast compositions of varying thickness. Conventional mammography uses automatic exposure control (AEC) devices to produce a constant film optical density (~ 1.5) in the uniformly compressed breast region. The film densities around the peripheral of the compressed breast are much greater than 2.0 due to the excessive x-ray exposure to the screen-film cassette in these areas.

Of more important concern are the dense breast regions which are frequently under-exposed, and therefore, displayed with poor film contrast. In practice, between 30 and 60% of mammography screening is performed on breasts composed of dense fibroglandular tissue (Whitehouse and Leinster, 1985). It has been shown that the detection of a lesion surrounded by the dense fibroglandular tissue is more difficult than in a fatty tissue background (Jones and Yaffe, 1987; Ma et al., 1992; Schmitt and Threatt, 1982). Epidemiological studies also have shown that women with dense breasts are at increased risk of developing breast cancer (Brisson et al., 1982; Gravelle et al., 1986). The failure to detect lesions in the dense regions of the breast or in the dense breasts is the major cause of missed early diagnosis of breast cancers (Ma et al., 1992).

Other factors affecting the diagnostic accuracy of screen-film mammography include image noise contribution from film granularity and scattered radiation (Barnes, 1992; Kuhn and Knupfer, 1992). The presence of film granularity significantly reduces the signal-to-noise ratio (SNR) of the film image, and especially degrades the system's ability to demonstrate microcalcification. Therefore, even though mammographic screen/film systems have high limiting spatial resolution of about 20 line pairs per mm (lp/mm), their low-contrast performance is severely limited beyond 5 lp/mm by film granularity. Scattered radiation greatly reduces the displayed contrast and SNR. Conventional scatter removal techniques using grids can lead to a factor of 2 to 4 increase

in mean glandular dose (Dance et al., 1992; Hammerstein et al., 1979; Huda et al., 1990; Skubic and Fatouros, 1989).

Finally, there is a fundamental compromise between the desire to give minimum patient dose through the use of a thick phosphor screen which causes a deterioration of spatial resolution, as shown in Figure 1-3 (a), and the desire to have high spatial resolution through the use of a thin phosphor screen and/or increased light absorbing dye content in the screen which requires a higher patient dose, as shown in Figure 1-3 (b). The high spatial resolution performance of modern mammography screen-film cassettes is achieved at the price of low screen x-ray interaction efficiency (less than 70%) for x-ray energies used in mammography.

x-ray quantum   x-ray quantum

Thick Phosphor Screen   Thin Phosphor Screen

(a)   (b)
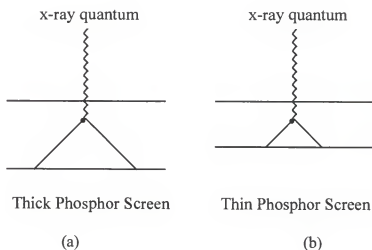
Figure 1-3. Light dispersion in (a) a thick phosphor screen, and (b) a thin phosphor screen.

1.2. Digital Mammography

1.2.1. Digital Mammography and Its Advantages

Digital mammography has the potential to overcome the limitations of conventional screen-film mammography and to improve the sensitivity of breast cancer detection. Digital mammography is a technique in which the screen-film detector is replaced by a digital x-ray detector which absorbs the x-rays penetrated through the compressed breast and converts the absorbed x-ray energy into electronic signals (Yaffe, 1992).

Unlike screen-film mammography in which an image is obtained, viewed, and stored using the same piece of film, the image acquisition, storage, and display are decoupled into three separate stages in digital mammography. The acquired image contrast is independent of the x-ray exposure to the detector because the dynamic range of a digital imaging system is usually larger than the exposure variations after the primary x-ray beam penetrating through the breasts. Image display contrast is no longer determined by the exposure techniques used to acquire a digital mammogram and can be optimized by adjusting the window and level of the display monitor. Storage and retrieval of digital images will likely be convenient, fast, and eliminate lost films.

Digital mammography and associated image processing and pattern recognition offers the most fruitful avenue for improving the detection of nonpalpable breast cancers (Schmidt et al., 1995). Digital mammography will promote digital image processing and other computer assisted diagnosis (CAD) methods, which have the potential to reduce the screening load and improve the diagnostic accuracy by reducing the number of false negative diagnosis. Teleradiology could be implemented to allow remote diagnoses using high quality digital mammograms.

It is possible that about 10% to 20% false negative diagnoses from mammography screening could be reduced using digital mammography and appropriate CAD method(s). The problems of imaging the dense breasts could also be solved using digital mammography systems. Unnecessary patient exposures due to film processor failure, overexposure, and underexposure are likely to be eliminated with digital mammography. By decoupling image acquisition, storage, and display, allowing optimization of each. Image contrast will then be adjustable under the control of the radiologist viewing the image.

In addition to providing potentially improved diagnostic accuracy in breast cancer screening, digital mammography systems can offer unique advantages in the other methodologies where manipulations of images in real time are required. These areas include digital subtraction dual energy mammography, digital subtraction angiography of the breast, and real time needle biopsy. Dual energy subtraction imaging removes the structure background on breast images and soft tissue and calcified tissue to be displayed in separate images. It has been shown that dual energy subtraction improved the detection of microcalcifications (Boone et al., 1990; Boone, 1991, Johns et al., 1985). By applying digital subtraction angiography technology to breast imaging, Carumbaya et al. (1996) found that the most common and difficult task of differentiating benign lesions from malignant cancers can be achieved by studying the abnormal vascularization of a lesion. This is done by observing the kinetics of iodinated contrast material. Core needle breast biopsy plus pathologic examination represents the most accurate method for differentiating between benign and malignant lesions (Jackson and Bassett, 1990). A digital mammography system can be used to localize the abnormality and guide the needle system to remove cells or tissue in real or near-real time thereby reducing patient discomfort.

1.2.2. Cost-Effectiveness of Digital Mammography

It is very difficult to estimate the cost-effectiveness of digital mammography at present. The costs of digital imaging systems currently being developed are expected to be ranging from $150,000 to $250,000, which is about twice as much as that of a screen-film system. Although the capital cost consideration may not favor a digital mammography system, the advantage of initial lower equipment costs of screen-film mammography diminishes as its clinical usage increases. For example, assuming 5000 patients are examined each year for one screen-film mammography unit, a minimum of 20,000 films at ~ $1.00 per film are needed. This will add to ~ $100,000 over a five years period for film cost alone. In addition, other costs, including film processing chemicals, storage cost, etc., also accumulate to a large amount over five years. The cost-effectiveness of digital mammography needs to be determined by how efficient the systems will be used, and needs to be judged from its clinical use over a reasonable period of time, say 5 to 10 years.

Many of the advantages of digital mammography which may improve the diagnoses of breast cancers also offer potentials to reduce the operational costs of clinical mammography screening. The storage cost of digital mammography is low and should get lower. This is to be compared to the added film and film storage cost for screen-film systems. About 10% screening mammographies must be repeated due to automatic exposure control (AEC) failure and film processor problems. It is probable that this image repeat rate will be largely eliminated by digital mammography. This will result in savings of films used and time required to perform mammographic procedures.

Using digital mammography, it is possible to acquire and display digital mammograms in almost real time. With associated CAD methods, it is also feasible for radiologists to make accurate diagnoses faster than with conventional mammography. Therefore, a digital mammography system may be used in a more efficient manner than

screen-film mammography. This means less mammography equipment may be needed for mammography screening. Through the use of a teleradiology system, diagnoses could be made by radiologists specialized in mammography at remote locations. The availability of interpreting radiologists may reduce the labor costs in establishing new mammography facilities. This could also increase the use of mammography. Expensive follow-up procedures such as biopsy may be avoided as a result of the improved accuracy in the detection of breast cancers from the use of digital mammography systems. Breast core biopsy is an example of how digital imaging systems can improve breast cancer diagnosis at reduced costs.

On the other hand, there are a few obstacles to the use of digital mammography regarding its cost-effectiveness. The number of dedicated mammography units installed has grown explosively in the 90s. It is nearly impossible for hospitals to replace existing systems with digital mammography systems. This may delay the wide application of digital mammography. Some digital mammography systems are designed to only replace the screen-film cassettes in image acquisition. However, the costs of the digital x-ray image detectors themselves are too expensive to justify the savings from the use of the existing x-ray tube and generator assemblies. Although remote diagnosis is attractive, it depends on a teleradiology system which most hospitals do not have at present time. The expense of installing a teleradiology system prohibits the benefits of digital mammography to be realized, hence, reduce the cost effectiveness of digital mammography.

It is expected that digital mammography systems will gradually replace conventional mammography systems for general breast cancer screening. It is not surprising that this transition may take up to 10 years in the United States. The use of high quality digital screening mammography has the potential to improve the sensitivity and specificity of breast cancer detection and, at the same time, provide reduced costs to both hospitals and patients.

1.3. Literature Review

1.3.1. Current Approaches to Digital Mammography

To realize the benefits of digital mammography, x-ray imaging detectors with appropriate characteristics must be developed. Various configurations for the acquisition of digital mammograms have been proposed: (a) different detector geometry such as point, line, slot and area; (b) different x-ray detectors such as photostimulable phosphor, amorphous selenium, and traditional phosphor screens optically coupled to charge-coupled devices (CCDs).

In the simplest geometry, a point detector could be used where a pencil beam of x-rays is raster-scanned across the breast and a single detector is used to record the image. In principle, this point geometry can produce images with (1) extremely high spatial resolution as determined by the scanning position accuracy; (2) excellent contrast as virtually all the scattered radiation are eliminated; (3) ~100% x-ray detection efficiency as very thick detection material can be used to absorb all the x-rays penetrating the breast. However, this point-to-point scanning process is extremely slow and may take hours to produce a single image. In addition, most of the x-rays produced at the x-ray tube are removed by the collimator which results in very inefficient use of x-ray output and an unacceptably high x-ray tube loading required to produce an image. A natural extension of the point detector geometry may be the use of a very thin line detector with x-ray beam collimated to cover the line detector. This approach was investigated by Bjorkholm at AS&E and abandoned eventually as a result of the long scan time imposed by the line geometry (Yaffe, 1996).

At present, two types of digital mammography detectors have been investigated, the area detector and slot detector.

Like screen-film mammography, an area detector approach efficiently utilizes the x-ray tube output and produces an image from a single exposure of x-rays in typically less than 1 second of time. Various approaches are being taken to develop a full area detector for digital mammography. One company (Cheung and Coe, 1995) uses multiple modules of the type of phosphor-demagnifying fiber optical image guide-charge-coupled device (CCD) camera that has been used clinically in the stereotactic biopsy system (Karellas and Harris, 1992; Krupinski and Roehrig, 1994). To cover a sufficiently large image area, a full field mammography detector requires a matrix of 3 x 4 of these cameras which results in a very high detector cost of ~ \$300,000. This approach has been shown to provide fast image acquisition. The limiting spatial resolution at the center of this large area detector is about 13 lp/mm. At present, this digital mammography system is under clinical evaluation.

Computed radiography (CR) systems using stimulable phosphor imaging plates have been used to produce general radiographic images in digital form (Kato, 1994). The dynamic range of typical stimulable phosphor imaging plates is in the order of 10^4:1. The limiting spatial resolution of modern stimulable phosphor imaging plates is, however, only approximately 5 lp/mm. This spatial resolution is much less than the about 20 lp/mm of mammography screen-film combinations. For several years, computed radiography CR systems have been investigated as a method for digital mammography. Cowen et al. (1992) compared the imaging performance of a CR imaging plate (0.1 mm pixel size) with a screen-film combination (~ 15 lp/mm spatial resolution) on the detection of low contrast discs on a uniform background. As a result of the adjustable CR image contrast, they found that CR images had a greater range of contrast detail presentation than screen-film images. In another study, Brettle et al. (1994) conducted an observer performance study to compare the noise, sharpness, and contrast performance of the two methods using clinical mammograms. Again, it was found that CR images provide greater contrast than film, and that spatial resolution of CR is lower than for film. One observer found CR

images were noisier than film images. In addition, an ROC study in evaluating the observer confidence of correct classification showed a comparable imaging performance for the two methods. Higashida et al. (1992) evaluated the differences in detecting subtle microcalcifications (less than 0.25 mm) using a typical CR imaging plate (0.1 mm pixel size) and the two widely used screen-film combinations (~ 20 lp/mm limiting spatial resolution). The results from their ROC study indicated that detectability of subtle microcalcifications on CR images was significantly lower than on both types of screen-film images. The area under the ROC curve was 0.68 for the CR images and was 0.82 for both screen-film images. They concluded that the use of a CR system with a pixel size of 0.1 mm in detection of small microcalcifications will be problematic. CR system are also being investigated by other investigators (Gagne et al., 1996; Prior et al., 1994). However, its application to mammography is questionable due to its low spatial resolution performance.

Recently, a large area detector using amorphous silicon as the readout device has been developed by G.E. Medical for digital mammography. In such a detector, x-rays are absorbed by a layer of cesium iodide which is deposited directly on a matrix of light sensitive elements (pixels) produced in the amorphous silicon substrate. The pixel size is ~100 μm which limits the achievable spatial resolution. In another approach (Chotas et al., 1995; Fahrig et al., 1995; Neitzel et al., 1994;), a large area photoconductive selenium layer was applied over a similar active matrix readout, which is sensitive to the charges liberated in the selenium layer by absorption of x-rays. This direction of conversion of x-ray to electron signal has the potential to achieve very high detective quantum efficiency. Also, high spatial resolution is achievable with the selenium detector as a result of restricted charge spread by the electric field applied in the selenium layer. If successfully developed, the selenium detector approach could provide significantly improved imaging performance in mammography. The only disadvantage is that the cost of the selenium detectors is likely to be very expensive.

1.3.2. Scanning Slot Digital Mammography

The slot detector approach is a compromise between an area detector, where scattered radiation and system cost are of concern, and a line detector, where imaging time and x-ray tube loading presents difficulties. In their present forms, scanning slot digital mammography utilizes a scanning slot detector geometry in which a slot shaped x-ray conversion plate is optically coupled to CCDs which are operated in the time-delayed integration (TDI) mode while the slot detector is scanned (Henry et al., 1995; Maidment et al., 1993a; Neitzel et al., 1994; Nishikawa et al., 1987; Toker and Piccaro, 1993).

Scanning slot digital mammography systems have been developed and investigated for general mammography screening. Figure 1-4 shows the diagram of a typical scanning slot digital mammography system and its operating principle.
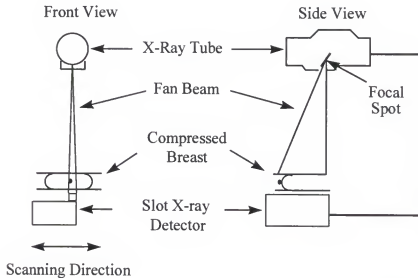
Figure 1-4. Schematic of a scanning slot digital mammography system.

The x-ray generator and x-ray tube is capable of operating continuously for more than five seconds with uniform x-ray output. The x-ray tube employs either a molybdenum (Mo) anode or a tungsten (W) anode with a nominal focal spot size of 0.3

mm. The slot x-ray detector is typically about 20 cm long to cover the whole compressed breast. The width of the x-ray imaging detector varies from 4 mm to 10 mm in the current scanning slot digital mammography system designs. The slot x-ray detector is located about 60 cm from the x-ray tube focal spot and is mounted rigidly relative to the x-ray tube.

A fan shaped beam of x-rays is formed at the x-ray tube output using a lead collimator. This fan x-ray beam covers the entire slot x-ray detector sensitive area. The patient stands still with the breast compressed. During image acquisition, the fan x-ray beam and the slot x-ray detector are scanned across the breast in a direction parallel to the short dimension of the x-ray imaging detector in a distance covering the whole breast in less than five seconds. This short imaging time is necessary to minimize patient inconvenience and movement during the scanning process.

The two major advantages of the scanning slot digital mammography approach are the efficient rejection of scattered radiation from reaching the slot x-ray detector and the relatively inexpensive equipment cost compared to an area detector approach. Figure 1-5 compares the geometry between a slot x-ray detector and an area detector in which scattered x-rays have higher probabilities to miss the slot detector.
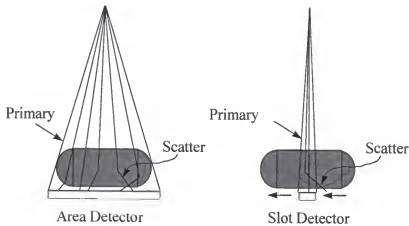
Figure 1-5. Imaging geometry for an area detector and a slot detector.

The initial designs of the slot x-ray detectors in the scanning slot digital mammography systems used a Gd_2O_2S:Tb rare earth phosphor screen optically coupled to charge-coupled devices (CCD) through the use of a tapered glass optical fiber image guide (Maidment et al., 1993a; Toker and Piccaro, 1993). The image guide had an approximately 2:1 input to output ratio. Maidment et al. (1993a) used a slot x-ray detector which was 4.0 mm wide and 21 cm long. Preliminary test images were obtained in 7.8 seconds over a scanning distance of 18 cm. A 40 KV tungsten-target spectrum was produced from a 0.3 mm focal spot. The spatial resolution of this slot x-ray detector was measured to be 9.5 lp/mm. At that slow scan speed of 2.3 cm/second, the imaging performance of this scanning slot digital mammography system were equal to or better than for mammography screen-film systems. Toker and Piccaro (1993) used a 10 mm wide slot x-ray detector and have reported similar results to those of Maidment et al..

However, there are several technical problems which could limit the imaging performance of these phosphor based scanning slot digital mammography systems. First, using a phosphor coupled to CCDs will inevitably reduce the spatial resolution compared to the modern mammography screen-film combinations, for which a single emulsion film is used in combination with a single back-intensifying screen. Second and most importantly, it is necessary that a whole breast image should be acquired in less than five seconds. The afterglow (slow scintillation decaying component) nature of the Gd_2O_2S:Tb phosphor could limit the spatial resolution performance of the scanning slot detectors in mammography. The image acquisition time for each detector pixel in TDI-CCD scanning is about 1 msec (50 μm pixel size moving at 5 cm/sec to cover 20 cm imaging length in 4 seconds). During the 1 msec exposure time, Gd_2O_2S:Tb phosphor emits only 47% of its total scintillation light (Gluer et al., 1989). The rest of the scintillation will spread to adjacent pixels while the charges in the CCD pixels are integrated along the entire TDI column. This could significantly reduce image contrast and detector modulation transfer

function (MTF) at all spatial frequencies. Mainprize and Yaffe (1996) studied the $Gd_2O_2S:Tb$ phosphor afterglow effect on image spatial resolution by varying the scanning speed of a scanning slot digital mammography system. They found the ratios of system MTF at 8 cm/second to the system MTF at 6 cm/second were about 0.95, and 0.92 at 2 and 3 lp/mm spatial frequencies, respectively. Unfortunately, they did not report any measurement of the difference in MTF between about 2 cm/second scanning speed to that at high scanning speeds (> 4 cm/second) where the afterglow effect could be better demonstrated.

Henry et al. (1995) investigated the use of a hybrid photodiode array as the x-ray conversion material in a slot x-ray detector. The hybrid photodiode array directly converts the x-rays into electrons thereby has the potential to provide high signal-to-noise performance. And because the electrons are collected by the bias voltage applied across the photodiode layer, high spatial resolution could also be achieved using thicker photodiode layer. The prototype device was made of a 300 μm thick, 256 x 256 array of 30 μm pixels. Their results showed that the detector MTF was superior to that of mammography screen-film combinations. There are two major problems associated with this design. First, the 300 μm photodiode layer thickness provided very low x-ray interaction efficiency (about 20% at 20 keV). It was found to be necessary to use an approximately 1.5 mm thick photodiode layer to achieve a comparable x-ray interaction efficiency as that of mammography phosphor screens. This large thickness causes significant geometry blur due to obliquely incident x-rays at the edge of the detector. These investigators proposed to curve the slot detector by using a number of photodiode array less than 2 cm long but no progress has been reported by far. The second problem is the noise from dark current generation as a result of large silicon volume. This is potentially a serious obstacle. Other issues include radiation damage to the detector and possible high cost.

1.3.3. Spatial Resolution in Digital Mammography

The imaging requirements for mammography are extremely demanding. To resolve fine microcalcifications in the breast, the imaging system should provide very high spatial resolution. At the same time, to image the extremely subtle differences between tumor and normal breast tissue, the signal-to-noise ratio and contrast performance of the imaging system must be excellent. The detector must combine these resolution and noise properties with a format capable of acquiring a complete breast image, 20 cm x 20 cm at least, in less than 5 seconds. It is also very important that the system must be as efficient as possible in the use of incident x-rays.

The spatial resolution required for an imaging system depends strongly on the type of abnormality to be detected. In mammography, the required resolution is determined by the detection of microcalcifications in the breast. To resolve fine microcalcifications in the breast and permit the study of the morphology of breast microcalcifications, the imaging system must provide very high spatial resolution. Calcifications due to malignancy are generally less than 0.5 mm in size and can be microscopic. The importance of microcalcifications in the breast is linked to a large number of cancers detected by this sign and to the fact that due to this sign it is possible to find approximately 50% of noninvasive lesions. In the framework of the general public, the detection of clustered microcalcifications permits the detection of approximately 50% of cancers in a population. However, the problem of the specificity of this sign has arisen since only 25% of the microcalcification sites are in fact cancers. The precise analysis of clustered microcalcifications can bring about an important reduction in the number of operations in return for a small or nonexistent risk for the patients.

A number of ROC studies have been performed to study the spatial resolution requirement for digital mammography by digitizing screen/film mammograms. Chan et al. (1987) conducted a study to assess the effects of digitization and image processing on

the detectability of subtle breast microcalcifications in digital mammography. Digital images were obtained by digitizing conventional screen-film mammograms with a 0.1 mm x 0.1 mm pixel size. These digitized images were also processed with unsharp-mask filtering. The unprocessed digital images and the unsharp-masked images were then reconstituted back on films. In the study, twenty normal cases and 12 cases with subtle microcalcifications were included. Observer performance experiments were conducted to assess the detectability of subtle microcalcifications in the conventional, unprocessed digital, and unsharp-masked digital mammograms. The authors concluded that digital mammograms obtained with 0.1 mm x 0.1 mm pixel size provide lower detectability than the conventional screen-film mammograms. Unsharp-masking improved the detectability of microcalcifications in digitized mammograms. However, the detectability of microcalcifications on the processed mammograms was found to be less than that on the conventional films.

The results from a study performed by Karssemeijer et al. (1993) appeared to contradict the results reported by Chan et al. (1987). In this study, a set of 72 screen-film mammograms showing benign or malignant microcalcifications were digitized with a 0.05 mm sampling aperture and a 0.1 mm sampling distance. The digitization only covered an area of 2.5 cm x 2.5 cm on each film where the microcalcifications were located. To view screen-film mammograms, an equally sized black film in which a 2.5 cm x 2.5 cm square hole was cut corresponding to the digitized area was used to force the observers to base their judgments on such small detailed areas. The digitized area (256 x 256 pixel matrix) was magnified to full monitor screen and displayed with 1024 x 1024 pixel matrix. The results from ROC study indicated that differentiation of benign from malignant cases decreased only slightly on the digitized images, and the characterization of different types of malignancies somewhat improves by digitization. The authors therefore concluded that a relatively low spatial resolution of 0.1 mm pixel does not prohibit high-quality diagnostic performance in digital mammography. It is difficult to

compare the results reported by Chan et al. and Karssemeijer et al. because the differences in the selections of cases and criteria in the observe performance studies. There may be some improvements in the latter study as a result of displaying the small digitized area on the monitor. The image contrast was adjusted by the observers for optimal contrast. However, this method of display does not simulate real mammography screening where mammographers always look at the entire breast image first. Furthermore, the authors acknowledged that the observers were not asked to count the individual microcalcifications in the detected clusters. The detectability of the smallest calcifications may have been worse in the digital images. Based on histological findings, the authors also indicated that all structures of interest were not imaged on digitized images.

Chan et al. (1993) investigated the effects of pixel size on computer-aided detection of microcalcifications on digitized screen-film mammograms. Twenty-five mammograms were digitized with a laser film scanner. A computer program was applied to process the digitized images and locate the microcalcifications. It was found that the detection accuracy decreases significantly as the pixel size increases from 0.035 mm x 0.035 mm to 0.07 mm x 0.07 mm (P<0.007) and from 0.07 mm x 0.07 mm to 0.105 mm x 0.105 mm (P<0.002). The detectability of some microcalcifications that were visible on the original mammograms was also found to decrease when a pixel size of greater than 0.035 mm was used. This suggested that very high spatial resolution is required for digital mammograms in CAD applications. By applying wavelet based image processing algorithms to digitized mammograms, Qian and Clark (1995) have also shown that clusters of microcalcifications and their morphologic aspects in the processed mammograms were clearly presented when screen-film images were digitized with 0.035 mm pixel size, but were very difficult to identify in the original mammograms and processed mammograms with a pixel size of 0.1 mm.

In summary, ROC studies have suggested that differentiation of benign from malignant cases always decreased because of the large pixel size used on the digitized film images. This demonstrated that high spatial resolution with pixel size ranging from 0.035 mm to 0.1 mm is required for digital mammography in order to capture subtle microcalcifications detectable on screen-film mammograms.

1.3.4. Dynamic Range in Digital Mammography

The dynamic range requirement of a digital mammography system depends on the x-ray energy spectrum, scattered radiation, breast thickness and composition. For molybdenum (Mo) target spectra, a number of studies (Gambaccini et al., 1993; Nishikawa et al., 1987) have shown that the ratios of the maximum x-ray intensity to the minimum x-ray intensity in the detector plane after uniform x-ray exposure to compressed breasts are generally in the range from 10 to 100, and could be as high as 400 for very thick and dense breasts.

Maidment et al. (1993b) investigated the effect of dynamic range in digital mammography on the discernible image gray levels when tungsten (W) and Mo anode x-ray spectra are used. This study also took into account the effect of detector coupling efficiency and CCD electronic noise on the requirement of dynamic range. It was found that, for an ideal detector (ideal optical coupling, no inherent detector noise) with infinite dynamic range, 3100 image gray levels would be differentiable assuming a 40 KV W anode spectrum with 1 mm Al filtration. For the same spectrum, a detector with total coupling efficiency of 16 electrons per x-ray interaction and a dynamic range of 3000 would decrease the number of gray levels that could be resolved by only 2% compared to the ideal detector. This reduction increased to 26% for a detector with total coupling efficiency of 2 electrons per interacted x-ray and a dynamic range of 240. Hence, it is desirable to have a detector with a dynamic range about 3000 to improve the resolvable

image gray levels (i.e., signal to noise ratio). Furthermore, they found that, on the basis of dynamic range, W spectra are preferable for digital mammography, since Mo spectra yielding the same signal to noise ratio require a detector with dynamic range twice as large.

1.3.5. X-ray Spectra and X-ray Tube Heating Considerations

Optimized x-ray spectra using Mo anode for screen-film mammography have been investigated for many years (Beaman and Lillicrap, 1982; Jennings and Fewell, 1979; Desponds et al., 1991). It was found that Mo anode x-ray spectra in combination with ~30 μm thick added Mo filtration provides the optimized x-ray spectra for most imaging situations. Recent investigations were to optimize x-ray spectra from rhodium (Rh) and W anodes with different filtration materials (Desponds et al., 1991; Jafroudi et al., 1995). The Rh and W x-ray spectra typically have higher x-ray energy thereby providing increased penetration compared to Mo x-ray spectra. This allows the efficient use of x-ray tube output for the examinations of thick and radiographically dense breasts.

In scanning slot digital mammography, in addition to the optimizations usually considered in screen-film mammography, the optimization must take into account of the much longer imaging time and very high x-ray tube heating constraints. Yaffe (1992) compare the influence of detector geometry on imaging time and x-ray tube loading for digital mammography. To imaging an area of 18 cm x 24 cm, a slot x-ray detector with 3.2 mm and 10 mm width would require about 60 times and 20 times the x-ray tube loading of an area detector, respectively. As a result of the relatively long imaging time ~ five seconds, the x-ray tube input power must be reduced to avoid overheating the x-ray tube which again increases the imaging time required. This indicated that either a high power x-ray tube with very large tube heating capacity or higher x-ray energy spectra are needed for scanning slot digital mammography.

Mo anode x-ray spectra are always desirable because they provide high image contrast. Because of their low x-ray energies and lower probability of penetration, the use of Mo anode x-ray spectra requires the development of a high power x-ray tube with large tube heating capacity which exceeds current x-ray tube technology. At present, W anode x-ray spectra are preferred because they provide higher x-ray energies at higher tube potential. Also, the x-ray production efficiency of W is higher than that of Mo. The University of Toronto group (Fahrig et al., 1992; Fahrig and Yaffe, 1994a; Fahrig and Yaffe, 1994b) investigated the optimized x-ray spectra based on image signal to noise ratio (SNR). It was found that a W anode with Rh filtration gives higher SNR at imaging time from 3 to 8 seconds than Mo anode with Mo filtration.

1.4. Purpose of Study

1.4.1. Primary Objectives

In this study, two scintillation screen materials (plastic scintillating fiber screen and a new thallium activated CsI (CsI:Tl) screen) were investigated as alternatives to the rare-earth phosphor (Gd_2O_2S:Tb) screen that has been used as the x-ray to light converter in the scanning slot x-ray detectors for digital mammography. The advantage of the Gd_2O_2S:Tb phosphor is its high efficiency (15%) in converting x-ray energy into light photon energy. Although the intrinsic spatial resolution of Gd_2O_2S:Tb phosphor screen used in mammography is very high (~ 20 lp/mm), when used in a scanning imaging application, the achievable spatial resolution is severely limited by its delayed scintillation light emission which spreads light over a long scanning distance. The x-ray interaction efficiency of the Gd_2O_2S:Tb phosphor screen is also low as a consequence of using thin phosphor to maintain high spatial resolution.

These problems can be overcome by the use of a plastic scintillating fiber screen (SFS) or a CsI:Tl screen. The scintillation decay time is about 1 ns for plastic scintillators and about 1 μs for CsI:Tl crystal. These are compared to about 400 μs for the Gd_2O_2S:Tb phosphor. A SFS can potentially eliminate the compromise between spatial resolution and x-ray interaction efficiency. However, the energy conversion efficiency of plastic scintillators is typically very low and in the range from 3 to 4.5%. The effects of this low conversion efficiency on the achievable image signal performance and methods to enhance the image signal must be investigated. The use of a CsI:Tl screen is a compromise between the use of a Gd_2O_2S:Tb phosphor screen and a SFS. The energy conversion efficiency of the CsI:Tl crystal is 12% which is lower than that of Gd_2O_2S:Tb phosphor but significantly higher than the plastic scintillator. The CsI:Tl screen is composed of columnar CsI:Tl crystals. This fiber-like structure minimizes the scintillation light spread and therefore allows the use of the relatively thicker CsI:Tl screen to improve its x-ray interaction efficiency. The performance of the CsI:Tl screen should be compared to that of the Gd_2O_2S:Tb phosphor screen and SFS.

The first objective of this study was to optimize the slot x-ray detector width based on the presence of scattered radiation and with consideration of the high x-ray tube loading requirement in the scanning slot imaging geometry. In principle, a smaller slot detector width is desired for better elimination of scattered radiation. This will greatly improve image contrast with no penalty in patient dose. However, the smallest slot detector width is limited by the x-ray tube heat loading capacity and the time permitted to acquire one breast image. By studying the amount of scattered radiation present in slot x-ray detectors of varying detector width, an optimized slot detector width can be determined which can provide sufficient scatter rejection and relative efficient use of x-ray tube output.

The second objective of this research was to investigate the imaging performance of using a novel high Z element loaded plastic scintillating fiber screen or a new CsI:Tl

screen to replace the rare-earth phosphor (Gd_2O_2S:Tb) screen that has been used as the x-ray-to-light converter in the initial designs of scanning slot x-ray imaging detectors for digital mammography. One goal was to determine the optimal material compositions to be used in a plastic scintillating fiber screen which will produce the appropriate imaging performance when used in a slot x-ray detector for mammography. The effects of these screen materials on the slot detector imaging performance were studied.

The study was divided into the following three projects to determine the optimal slot detector width based on the effect of scattered radiation, and quantify the slot detector signal and noise performances related to the different screen materials.

1.4.2. Scatter to Primary Ratios

Monte Carlo simulations were performed to quantify the amount of scattered radiation in a scanning slot detector geometry designed for use in digital mammography. Ratios of the scatter to primary (S/P) x-ray photon energy absorbed in the detector were obtained for a lucite phantom and were investigated as a function of photon energy, phantom thickness and slot detector width. For accurate computation, the Monte Carlo simulations implemented the corrections of atomic electron binding effect for Compton scattering, and inter-molecular interference on the coherent scattering cross section data. The relative contributions of Compton and coherent scattering to the total scattered radiation reaching the detector were determined. In addition, the scatter reduction by the use of an air gap was assessed and compared to that of using grids in conventional screen-film mammography. By comparing the difference of S/P ratios in slot x-ray detectors using two different scintillating screen materials, the results obtained were generalized and can readily be applied to enable the design and optimization of current and future development of scanning slot x-ray imaging systems.

1.4.3. Signal

Image signal and spatial resolution performances of a polystyrene based SFS, various high Z element loaded SFSs, the CsI:Tl screen, and all the corresponding slot x-ray detectors were investigated by theoretical analysis and experimental methods. The signal was characterized by the screen x-ray interaction efficiency, number of scintillation light output from the screen per interacted x-ray, and finally the number of CCD electrons produced from each incident x-ray photon. Spatial resolution was depicted by quantifying the modulation transfer functions of the screens and the slot x-ray detectors made of these screens. For SFSs, the effects of loading high Z element into the SFS, the effects of the concentration of a high Z element in a SFS, and the effect of SFS thickness on the signal and spatial resolution performance of the screens and slot x-ray detectors were studied in detail. The signal intensity and spatial resolution of a prototype scanning slot x-ray detector using the CsI:Tl screen were measured and compared to that of the same slot x-ray detector using a $Gd_2O_2S:Tb$ phosphor screen. The spatial resolution performance of a Polystyrene based SFS was also measured using an image intensifier system.

1.4.4. Noise

This project investigates the noise performance in these novel scintillation screens and their corresponding slot x-ray detectors. Scintillation light intensity distributions from monoenergetic x-ray interactions in these scintillation screens were generated and used to analyze the Swank factors and zero spatial frequency detective quantum efficiency (DQE(0)) of the scintillation screens. A modified cascaded noise propagation model was used to describe the noise propagation in the slot x-ray detectors. This analysis allowed the computation of spatial dependent DQE of the slot x-ray detector. The effects of x-ray energy, x-ray exposure, image guide coupling efficiency, CCD quantum efficiency, and CCD electronic noise on detector DQE were studied. The differences in noise

performances among various SFSs and their corresponding slot x-ray detectors were compared. The advantages and problems for SFSs and CsI:Tl screen were identified.

2.1. Introduction

In this study, a scanning slot x-ray detector and a prototype imaging system are developed to investigate the use of two new scintillation screens as alternatives to conventional rare-earth phosphor screens as the x-ray-to-light converter in the scanning slot digital mammography approach. The two scintillation screens are a plastic scintillating fiber screen (**SFS**) and a Thallium activated CsI scintillation screen (**CsI:Tl**).

A SFS is composed of individual plastic scintillating fibers fused together with their axes aligned to the direction of the incident x-ray beam. Because the scintillation light dispersion is limited to the individual fiber diameter, a relatively thick SFS can be used to increase its x-ray interaction efficiency without degrading spatial resolution. The scintillation decay time of a plastic scintillator is only a few nanoseconds which guarantees no loss of modulation transfer function when an SFS is used in the scanning imaging applications.

The CsI:Tl screen has similar advantages over rare-earth phosphor screens when used in a scanning slot x-ray detector for digital mammography. The scintillation decay time for CsI:Tl is only ~1 μs which eliminates the afterglow effect associated with the use of rare-earth phosphor. The CsI:Tl screen is configured of prismatic CsI crystals (needles). This fiber-like structure serves to limit the spread of the scintillation light which permits the use of a relatively thick CsI:Tl screen to improve detector x-ray interaction efficiency without sacrificing resolution performance.

29

In this chapter, characteristics of these new scintillation screens are described. A slot x-ray detector which can use either one of the new scintillation screens is designed. A description of a prototype scanning slot imaging system which was used to measure the imaging performance of the slot x-ray detectors is given.

2.2. Scintillation Screens

2.2.1. Materials and Structures

A schematic of a slot shaped plastic scintillating fiber screen (SFS) designed for mammography is shown in Figure 2-1. Because plastic scintillators have much lower x-ray stopping power than typical phosphor screens used in mammography, it is necessary that the thickness of a plastic SFS should be greater than 1 cm to produce a reasonably high x-ray interaction efficiency. To take account of the parallax effect as a result of this relatively larger thickness, the fiber axes are arranged to be parallel to the direction of the incident x-rays, as shown in Figure 2-1. At the end of the slot detector closest to the chest wall, the fibers are normal to the slot plane.
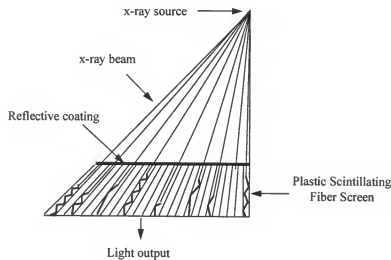
Figure 2-1. A slot shaped plastic scintillating fiber screen (SFS).

A layer of reflective coating painted on the SFS front surface can be used to reflect the light which are transmitted to this surface back to the SFS output. The use of this layer of reflective coating has been measured to increase the SFS light output by a factor of about 1.8 using a polystyrene based SFS based imaging intensifier imaging system (Choi et al., 1994).

Recently, a new CsI:Tl screen became available from Hamamatsu Photonics K.K., Japan (Okumura et al., 1995). This screen is composed of prismatic CsI crystals, which are made by using a special evaporation method to enable the needle-shaped CsI crystals (needles) to grow in the direction perpendicular to a supporting base. The needle size is about 5 μm and very uniform. Figure 2-2 shows the scintillation light dispersion in the CsI:Tl screen to that in a $Gd_2O_2S:Tb$ phosphor screen. When scintillation is generated in each needle, the needle serves as a guide to conduct the light. This fiber-like structure results in a very high resolution.
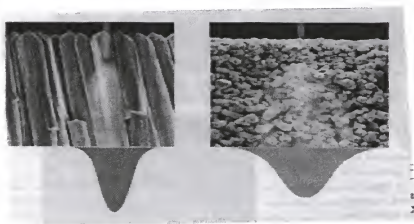
Figure 2-2. Scintillation light dispersion in a prismatic type CsI:Tl screen (left) and a $Gd_2O_2S:Tb$ phosphor screen (Right). Picture is taken from the work of Okumura et al. (1991).

The supporting base of this CsI:Tl screen is uniquely a glass fiber optical plate with numerical aperture equal to 1.0. The fiber diameter is 6 μm. The core glass packing fraction is 75%. This provides an excellent optical interface which preserves the high spatial resolution of the CsI:Tl screen.

2.2.2. X-ray Conversion

At x-ray energies used in mammography, x-ray interactions within a SFS include photoelectric effect, Compton scattering, and coherent scattering. Figure 2-3 shows the x-ray interaction processes of these three interaction mechanisms. Each number represents a case where an incident x-ray interacts in the SFS.

Incident X-ray Photons

(2)   (3)   (1)   (6)   (5)   (4)

Compton Scattered
X-ray Photons

Coherently Scattered
X-ray Photons
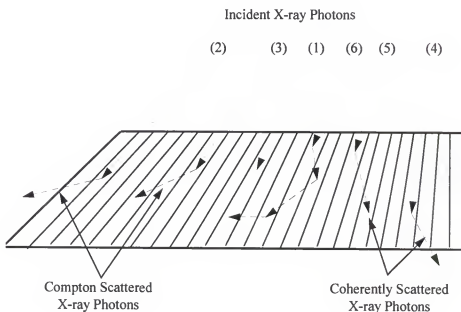
Figure 2-3. X-ray interaction mechanisms in a plastic scintillating fiber screen.

In the photoelectric absorption process as shown for incident x-ray photon (Case 1), the x-ray photon undergoes an interaction with the absorber atom in which the x-ray photon completely disappears. An energetic photoelectron is ejected by the atom from

one of its bound shells. The atomic excitation energy is released through the emission of characteristic x-rays or Auger electrons. For the plastic SFS, the binding energy of the photoelectron in its original shell is so small that the majority of the original x-ray photon energy is carried by the photoelectron.

A large fraction of the x-ray interactions within the SFS are through the Compton scattering process. The scattered x-ray energy, E_S, is a function of the incident x-ray energy, E, and the angle, θ, of the scattered x-ray photon with respect to its original direction, and is given by

$$E_S = \frac{E}{1 + \frac{E}{511}(1 - \cos\theta)} \qquad (2\text{-}1)$$

where E and E_S are in keV. The minimum scattered x-ray photon energy occurs when $\theta = \pi$. For example, the minimum scattered x-ray photon energy is about 18.55 keV and 26.85 keV for 20 keV and 30 keV incident x-ray photons respectively. The majority of the original x-ray photon energy is carried away by the Compton scattered photons. As shown in Figure 3-2, a Compton scattered photon can either escape the SFS without interaction (Case 2), or interact again within the SFS by photoelectric absorption (Case 3). Case 3 leads to a spatial spread of the deposited x-ray energy and produces false image information.

Compared to photoelectric absorption and Compton scattering, the cross section for coherent scattering is relatively small. In a coherent scattering event. All the original x-ray energy is transferred to the scattered x-ray photon energy without any energy deposition in the interaction site. Like the Compton scattered photons, coherently scattered photons can either leave the SFS without interaction (Case 4) or totally be absorbed by the SFS at a remote location from the original interaction site (Case 5). Case

6, as shown in Figure 3-2, is an example of an incident x-ray photon undergoing multiple scattering within the SFS.

It is desirable that x-ray interactions inside a SFS be dominated by the photoelectric effect. However, the interaction cross sections of Compton interaction and the photoelectric effect are comparable in the plastic SFS. The scattered x-ray photons carry most of the incident x-ray energy away from the primary interaction sites. This effect leads to variation in the x-ray energy deposition per incident x-ray. Reabsorption of these scattered x-ray photons within the SFS also leads to a spatial spread of deposited x-ray energy from a single incident x-ray.

It is clear that imaging performance of a plastic SFS could be significantly improved by increasing the probability of photoelectric conversion of the x-ray photons. This can be achieved by incorporating compounds containing high Z elements into the core of plastic scintillating fibers. Loading high Z element into the plastic scintillator has been done for many years. Various weight percentages of Lead (Pb) and Tin (Sn) have been loaded in plastic scintillators for a variety of special applications (Becker et al., 1975; Birks, 1964; Eriksson et al., 1974; Hyman and Ryan, 1958). For example, Nuclear Enterprise (NE) has a plastic scintillator (NE-140) which contains 10% by weight Sn (Nuclear Enterprise Technology Inc., 1993). Bicron (Bicron Corporation, 12345 Kinsman Rd., Newbury, OH 44065) makes a product (BC-452) which contains 5% by weight Pb. Unfortunately, loading high Z elements leads to impurity quenching (decreased light output) in the plastic scintillators (Sandler and Tsou, 1964). An impurity quenching factor, q, is defined as the fraction of light loss due to the addition of high Z elements in the SFS. q is dependent on the choice of the high Z element and its concentration. In this study, two types of plastic scintillating fibers were modeled from the high Z element plastic scintillators. One is a scintillating fiber with 5% by weight tin loaded into the polystyrene based scintillation core material. Another is made of a tin loaded polystyrene

based scintillator. The tin concentration within the fiber was varied from 5% to 10% to investigate its effect on the imaging performance.

For the CsI:Tl screen, x-ray interactions are always dominated by photoelectric effect at mammography x-ray energies. In the typical x-ray energy range of 15 to 30 keV, CsI:Tl screen has the desired properties which convert the x-ray energy into scintillation light at the primary interaction sites. However, it has been proposed that, in scanning slot digital mammography, a higher x-ray tube potential (~40 kV) should be used to reduce the extremely high requirement of x-ray tube output when a lower x-ray energy is used (Maidment et al., 1993a). This involves a fraction of x-rays with energies greater than the iodine and cesium K-edges (33.2 keV for iodine and 36.3 keV for cesium with fluorescence yield ~ 88% for both). Following interactions of these high energy x-rays in the CsI:Tl screen, the number of K-characteristic x-rays emitted almost equals the number of these high energy x-rays. These K-characteristic x-rays are emitted isotropically and can lead to a large spatial spread of x-ray energy deposition in the CsI:Tl screen.

2.2.3. Scintillation Light Emission

The process of fluorescence is the prompt emission of visible radiation from a substance following its excitation by some means. When the excitation is caused by the ionizing radiation, the fluorescence is also referred as scintillation. The energetic photoelectrons from the x-ray interactions cause the excitation of molecules in the SFS. The fluorescence processes arise from transitions in the energy level structures of these excited molecules (Birks, 1964).

To efficiently convert the SFS light output into electronic signals, the wavelength of the SFS scintillation light should be in the range where the quantum efficiency of the CCD is high. Fluorescence spectrum of polystyrene based scintillator peaks at about 310 nm where typical CCD quantum efficiency is very low. Polystyrene based scintillators

also contain one or more wavelength-shifting solutes (dye), which scavenge energy from excited molecules and emit at longer wavelengths. For the plastic scintillator investigated in this study, two solutes were used: a primary solute and 3-Hydroxyflavone (3HF). Energy transfer between polystyrene and the primary solute is through a resonant dipole-dipole process, with fluorescence emission peaking at about 340 nm. Energy transfer between the two solutes is through the radiative process in which emission is followed by absorption of light. Figure 2-4 shows the absorption and fluorescence spectra of 3HF in polystyrene. The quantum efficiency of the Kodak KAF-0360 CCD is also shown in Figure 2-4. The use of 3 HF matches the scintillation light from the SFS well to the quantum efficiency of the CCD.
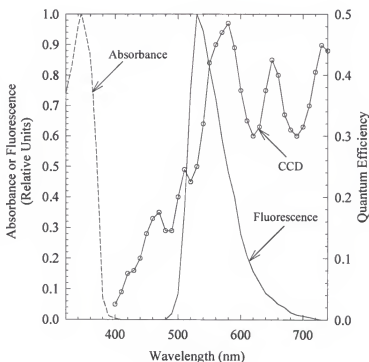
Figure 2-4. Absorption (------) and fluorescence (———)spectra of 3HF in polystyrene. Quantum efficiency of the CCD is also shown.

The energy conversion efficiency, ε, of a scintillation screen is defined as the fraction of all incident x-ray energy which is converted into visible light. One would always prefer this efficiency to be as high as possible. Unfortunately, there are alternate de-excitation processes available to the excited molecules which do not involve the emission of light and in which the excitation is degraded mainly to heat. As a result, ε of all polystyrene based plastic scintillators are low. In this study, a value of 4.5% for ε is used from comparing the measured scintillation pulse height spectra of the polystyrene based scintillator with a standard plastic scintillator with ε value of 3% (Bicron Corporation, Ohio).

Although a polystyrene based plastic scintillator is transparent to the fluorescence of 3HF, there is some overlap between the optical absorption and emission spectra of the primary solute. This leads to the self-absorption of fluorescence. This light loss is independent of the fiber length. In this study, a 15% light loss (L) was used to account for this self-absorption.

For the CsI:Tl screen, the prismatic CsI crystals produce strikingly more efficient light transmission than the powder type material such as Gd_2O_2S:Tb. This could compensate for its lower x-ray energy conversion efficiency (12%) compared to that (15%) of Gd_2O_2S:Tb phosphor screen. Figure 2-5 shows the scintillation light spectrum for CsI:Tl screen. The quantum efficiency of the CCD (Kodak KAF-0360) is also plotted in Figure 2-5 for comparison. The light emission peaks at ~575 nm and the wavelengths of about 2/3 of the light are greater than 550 nm, where the quantum efficiencies of the typical CCD are high.

2.2.4. Scintillation Light Collection

In a SFS, scintillation light produced by the ionizing photoelectron is guided by internal reflections along the scintillating fiber, as shown in Figure 2-6.
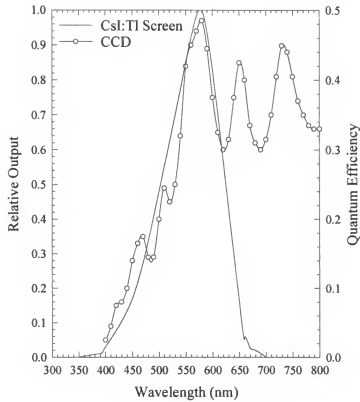
Figure 2-5. Scintillation light spectrum of the CsI:Tl screen and quantum efficiency of the CCD used.
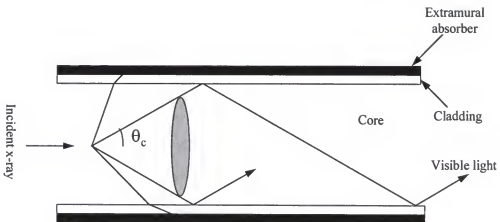
Figure 2-6. Scintillation light collection and transmission in a scintillating fiber screen.

Visible light emitted within the critical angle θ_c will be transmitted along each fiber. θ_c can be calculated from

$$\theta_c = \cos^{-1}\left(\frac{n_{clad}}{n_{core}}\right) \qquad (2\text{-}2)$$

where n_{clad} and n_{core} are the refractive indexes of the optical fiber cladding and core materials. A layer of extramural absorber material is coated to the fiber cladding to absorb those light photons which penetrate the fiber core/cladding interface. The fraction (F) of scintillation light which is transmitted within a fiber in one direction is given by

$$F = \frac{1}{2} \cdot (1 - \frac{n_{clad}}{n_{core}}) \cdot 100\% \qquad (2\text{-}3)$$

The values of F for some combinations of polymers are given in Table 2-1 below.

Table 2-1. Refractive index of selected polymers and scintillation light collection efficiency of the corresponding fibers.

Core Material	Cladding Material	F
Polystyrene (PS) (n=1.59)	PMMA (n=1.49)	0.031
PS	Fluorinated Polymer (FP) (n=1.35)	0.075

It is seen that the fluorinated polymer (FP) cladding produces a factor of greater than 2 scintillation light collection efficiency over the traditional PS/PMMA core/cladding combination. The critical angle, θ_c, is 31.9° for PS/FP fiber and 20.4° for PS/PMMA fiber.

In the CsI:Tl screen, although a relatively large fraction of scintillation light is channeled down the individual CsI crystal, there is also a large amount of scintillation

light which penetrates the interface between CsI crystal and air gap and reaches the screen output at a lateral distance away from the emission site. In addition, there is a substantial transmission loss of scintillation light. Figure 2-7 shows the scintillation light output from the CsI:Tl screen as a function of CsI:Tl screen thickness measured by Okumura et al. (1995) for uniform x-ray exposure to the CsI:Tl screen using a Tungsten (W) anode x-ray tube operating at 28 kVp with 1.8 mm Aluminum filtration. The measurement data was obtained from the manufacturer. It is seen that a thickness of 50 mg/cm^2 (150 µm) thick CsI:Tl screen gives the maximum light output.
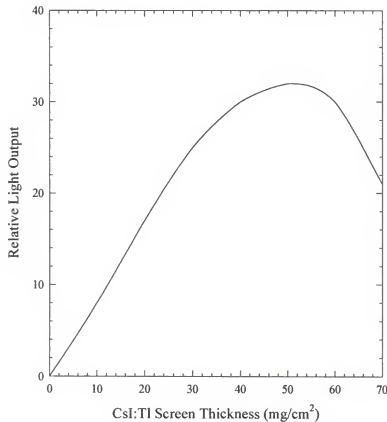
Figure 2-7. Scintillation light output as a function of CsI:Tl screen thickness as given by Okumura et al. (1995).

2.3. Slot X-ray Detectors

2.3.1. Detector Structures

A schematic of the slot x-ray imaging detector is shown in Figure 2-8. The incident x-ray photons are absorbed in the slot shaped scintillation screen. Scintillation light is produced and transmitted by the fiber optic image guides to the Charge Coupled Devices (CCD) operated in the time-delayed integration (TDI) mode. In this configuration, eight SFS-Fiberoptic Image Guide-CCD modules are used to form an x-ray imaging detector with length ≥ 20 cm. The bend in the fiber optical image guides eliminates physical interference between the adjacent CCDs, and ensures that the CCDs are not directly exposed to the x-ray field.
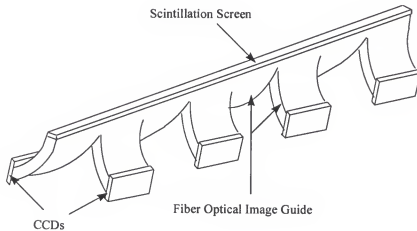
Figure 2-8. Schematic of a slot x-ray detector.

2.3.2. Fiber Optic Image Guide

The fiber optic image guide collects the scintillation light image originated from x-ray absorption within the scintillation screen and transfers the image to the CCDs. There is no reduction in image size in the image guide.

When a plastic scintillating fiber screen is used as the scintillation screen, the image guide can actually be a continuous extension of the SFS. This eliminates additional light transmission loss due to the use of a separate fiber optical image guide. For a CsI:Tl screen based slot x-ray detector, a glass or plastic optical fiber image guide can be used.

2.3.3. CCD Camera and Image Readout

A modular, low noise, fast readout CCD camera was developed. This CCD camera is designed to be operated at ambient temperature. The output from a CCD is amplified and then digitized at 2 MHz with a 14 bit analog-to-digital converter (ADC) located in the camera head. In the prototype detector, CCDs are readout in parallel in order to maintain ~4 cm/second scanning speed. Correlated double sampling (CDS) is implemented to reduce the effect of CCD reset noise. The image data is then captured by a PCI based image grabber developed by Imaging Technology Inc. This grabber is capable of acquiring image data at 35 MByte/s, which can handle the simultaneously output from eight camera modules (2 MHz x 2Byste x 8 = 32 MByte/s). Each of the eight slot images is transferred into the composite image which forms the entire mammogram. The final image is in a 8k x 8k x 14 bits format. The specifications of the CCDs used are shown in Table 2-2.

Table 2-2. Specifications of the CCD from Eastman Kodak Company. Model KAF-0360.

Size	26.4 mm x 7.92 mm
Pixel size	24 μm x 24 μm
Array	1100 x 330
Full Well Capacity	400,000 electrons
Dark Current @25°C	1080 e⁻/pixel/second
Readout Noise @1 MHz @25°C	50 e⁻ rms/pixel see note

note: correlated double sampling is assumed

2.4. Prototype Imaging System

2.4.1. Principle Structure

Figure 2-9 shows the prototype testing system which was developed to evaluate the imaging performance of the scanning slot x-ray detector. Imaging was performed using a Senograph 500T mammography x-ray unit. The x-ray tube had an Molybdenum (Mo) anode with a 30 mm added Mo filter. A 0.3 mm focal spot and a source to detector distance of 60 cm were used. A fan beam of x-rays was formed at the x-ray tube output by the use of a Lead collimator which resulted in an x-ray field size of 20 cm x 1 cm at the slot detector plane.
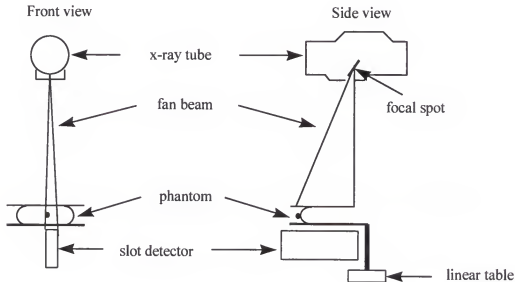
Figure 2-9. A diagram of the prototype testing system.

2.4.2. Time-Delayed Integration Mode of CCD Operation

To allow a smooth mechanical motion during the image acquisition, the CCDs are operated in the time-delayed integration (TDI) mode. Each CCD is capable of bi-

directional TDI mode operation, and is operated in Multi-Pinned-Phasing (MPP) mode of operation to reduce CCD pixel dark current generation. Figure 2-10 shows the principle of TDI operation.
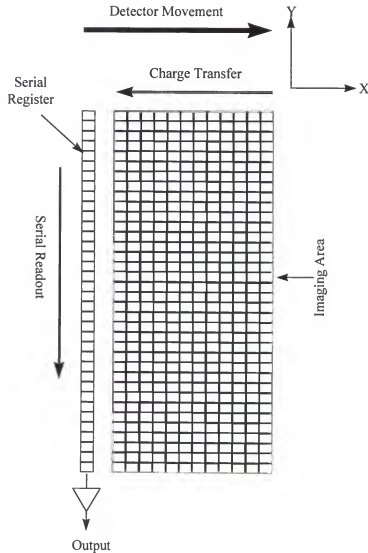
Figure 2-10. Schematic diagram of the TDI-CCD architecture.

TDI is based on the concept of taking multiple exposure of the same object (Holdsworth et al., 1990; Wong et al., 1992). In TDI operation, as the detector is moved across the breast at constant speed in the direction parallel to the X-direction, the charge

collected in each pixel of the CCD is shifted down its column at the same speed as that of the scan but in the opposite direction (-X-direction). This allows the charge generated in one portion of the image to integrate in the CCD pixels along the X-direction during image acquisition. If the total number of CCD pixels in the X-direction is N, the final image signal will be N times larger than that accumulated in any individual pixel.

After integrating N times, one column of the CCD charges are shifted to the serial register where the charges are read out at high speed. A line of the final image is then formed. The CCD readout noise only contributes once to the integrated signal. N = 330 for the Kodak KAF 0360 CCD.

Instead of scanning the detector and the fan x-ray beam, the prototype system had a phantom mounted on a 5 mm thick acrylic plate supported by a linear motion table. Phantom images were acquired by moving the phantom from one side of the slot detector to the other side in the direction parallel to the slot detector short dimension. After the phantom moved one CCD pixel size distance, a synchronization signal was generated to shift the integrating image on the CCD one pixel line in the opposite direction of the moving phantom as depicted in Figure 2-11.

The synchronization between the object motion and CCD pixel charge movement is the critical circuit that permits the imaging operation. An electronic pulse signal which is related to the motion can be obtained through the application of an linear encoder to the linear motion table moving the phantom. This signal can be modified as the application demands and sent to the CCD camera so that the CCD charge shifting is slaved to the motion of the phantom. In this way, any speed variation in the scanning motion is automatically coupled to CCD clocking which shifts the CCD pixel charge. The usually small fluctuation($\sim \pm 2\%$) around the average speed of the linear table will not affect the image spatial resolution. The synchronization signal was obtained from a timing circuit which counted the output of a high resolution (0.2 μm) linear encoder attached to the linear motion table.
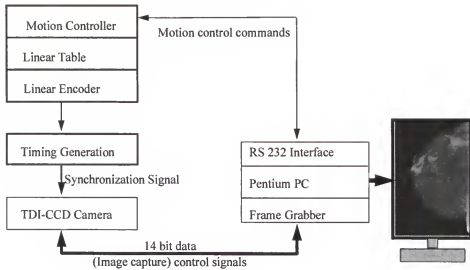
Figure 2-11. Functional diagram of the prototype testing system.

2.4.3. Spatial Resolution in TDI Mode Operation

The TDI mode of image data acquisition introduces several variables which degrade the detector modulation transfer function (MTF(f), where f is spatial frequency) (Wong et al., 1992). Velocity mismatch and discrete charge motion cause MTF degradation in the TDI direction. MTF degradation also occurs if the TDI columns are not aligned perfectly with the mechanical scan direction. The image MTF can be described as the product of the MTF without all these degradation factors and the MTFs due to various degradation.

In this scanning slot imaging system design, CCD charge shifting is slaved to the mechanic motion by the use of a linear encoder, MTF degradation due to velocity mismatch is eliminated. However, even under perfect synchronization, there still is a resolution loss because the charge is transferred in discrete steps in TDI mode of operation. This results in a mode in which the signal charge is always lagging behind the image by a subpixel amount and is never in total synchrony with the optical image. The

MTF$_{discrete}$(f) due to this effect is dependent on the clocking method for the CCD parallel array. Essentially, the greater the number of moves per stage, the smoother of the motion of the signal charge, and thus the less degradation in the MTF because of discrete charge motion. The CCD used is a two phase device, the MTF at Nyquist frequency (f_N) of the CCD, MTF$_{discrete}$(f_N), is estimated to be 0.9.

If the TDI columns subtend an angle θ with respect to the mechanical scan direction, the sampling aperture will move a distance of $NW_{CCD}\,tan\theta$ with respect to the image on the focal plane by the time the charge packet from the top of the TDI column reaches the bottom of the column. The effective sampling aperture for this situation is $NW_{CCD}\,tan\theta$ in the direction perpendicular to the TDI direction. The MTF due to angular misalignment is given by

$$MTF_{alignment}(f) = sinc\left(\pi f NW_{CCD}\,tan\theta\right) \qquad (2\text{-}4)$$

where N is the total number of CCD pixel in the TDI column, $N = 330$, W_{CCD} is the CCD pixel size in mm. For perfect alignment, $\theta = 0$, MTF$_{alignment}$(f) = 1, there is no reduction in image MTF. However, even for a small angle of 0.1^{o} or 0.5^{o} mis-alignment, image MTF will reduce by about 10% or 50% at 10 lp/mm spatial frequency. This misalignment is a potential source of image resolution degradation in a scanning slot digital mammography system.

2.4.4. CCD Camera Noise

The total noise in the image is determined by many independent factors, including x-ray quantum noise, detector intrinsic noise, and additive CCD camera noise. The noise of the TDI-CCD camera arises from the parallel imaging array, the serial shift register, and the output structures (Wong et al., 1992). The major noise sources for the KAF-0360

based CCD camera include thermal noise ($\sigma_{thermal}$), CCD readout noise (σ_r), and quantization noise ($\sigma_{digitization}$). The total camera noise is given by

$$\sigma_{camera} \approx \sqrt{\sigma_{thermal}^2 + \sigma_r^2 + \sigma_{digitization}^2} \tag{2-5}$$

The dark charge collected during the integration time and during transit from the imaging array to the output structure is characterized by a Poisson distribution. Its presence contaminates the signal charge and can contribute significant noise depending on the temperature and integration time. Dark charge is generated both in the bulk of the silicon and at the silicon-silicon dioxide interface just below the parallel gate structure. And the latter is the dominant source. This dark current component can be reduced by a factor of 20 or more in multi-pinned-phase (MPP) mode of CCD operation by biasing all of the parallel register gates to the same negative voltage. With KAF-0360, the total dark current generation is $D = 30$ pA/cm^2 (1080 e$^-$/pixel/sec). The thermal noise in each pixel of the image is given by (Wong et al., 1992)

$$\sigma_{thermal} = \sqrt{D \times \left(t_{integration} + t_{readout} \right)} \tag{2-6}$$

At scan line rate of 1818 Hz (5cm/second scanning speed), the total integration time $t_{integration}$ is about 0.182 second. At readout rate of 2 MHz, $t_{readout}$ is negligible compared to $t_{integration}$. So the thermal noise in each image pixel is 14 e$^-$ rms.

The readout noise of a CCD camera depends on many factors, such as the inherent on CCD preamplifier design, scan rate, the design of the post-amplifier electronics, and the preamplifier (CCD) temperature. The predominance of noise is reset noise due to the uncertainty in the voltage to which the output node is reset after each pixel is read, since the actual data is the voltage difference between the reset level and the valid video level.

Fortunately, reset noise is almost completely removed by correlated double sampling (CDS) technique. CDS takes advantage of the fact that the same noise component is present on valid video as on the reset level. The use of CDS double samples the off-chip amplifiers, thereby doubling the noise power added to the signal. However, careful design in the amplifier usually results in very small amplifier noise, which is much smaller than other noise sources and is not a significant contribution to the total noise.

The CCD charge transfer inefficiency ($\varepsilon = 0.00005$ @ 2 MHz data rate for KAF 0360) introduces shot noise because the charge packet left behind. This noise is a function of the sum of the number of TDI stages and the number of serial register stages (N_{stage}), number of CCD clocking phase (there are two phases for KAF-0360), and the number of signal and thermally generated electrons being transferred (N_{signal})

$$\sigma_{transfer} = \sqrt{2\varepsilon N_{stage} N_{signal}} \qquad (2-7)$$

In the CCD KAF-0360, there are 330 stages in each TDI column, and ≤ 1100 transfers along the serial shift register to reach the output FET, giving $N_{signal} \leq 1430$.

The total readout noise (σ_r), include transfer inefficiency, preamplifier, output FET and amplifier noise, is measured to be 50 e$^-$ rms at 2 MHz data rate at 25°C by the manufacturer.

The analog-to-digital conversion (ADC) quantization noise ($\sigma_{digitization}$) is expressed as

$$\sigma_{digitization} = \frac{1}{\sqrt{b}}\left[\frac{N_{signal}(full)}{2^b}\right] \qquad (2-8)$$

where, b is the ADC bits for quantization, b = 14. $N_{signal}(full)$ is the CCD full well capacity, $N_{signal}(full) = 200,000$ e$^-$. The resulted $\sigma_{digitization}$ is 3.3 e$^-$ rms.

The total camera noise, σ_{camera}, is calculated to be 52 e$^-$ rms using equation 2-5.

2.4.5. Detector Nonuniformity Correction

A flat fielding correction unit was implemented to do uniformity correction during the image scanning process in the camera readout hardware. Because the TDI mode of operation, this unit utilized a simple line correction algorithm. Before image acquisition, two line correction tables (8800 pixels/line) were recorded. First, a dark image is generated by scanning the detector in its normal TDI operation mode for the entire image area without x-ray exposure to the detector. The dark correction table I_d is then computed by averaging the pixel lines (perpendicular to scan direction) of the entire image. The flat field correction table I_f is obtained in the same way with high exposure to the detector so that the x-ray intensity fluctuation is negligible. During image acquisition, each line of the original image $I_{o,j}$ is corrected by the following algorithm (Blouke et al., 1987; Holdsworth et al., 1990)

$$I_{c,j} \propto \frac{I_{o,j} - I_d}{I_f - I_d} \tag{2-9}$$

where $I_{c,j}$ is the jth line of the corrected image. The x-ray quantum noise in the corrected pixel data equals to that in the uncorrected pixel data because of the averaging process and high x-ray exposure involved to obtain the correction tables.

Although this correction can be performed after image acquisition using software, this software correction may take very long time due to the large image data encountered. The use of a real time flat fielding correction unit reduces the digital mammography image acquisition time, and more importantly, enables the technician to check the image qualities while the breast is still compressed.

The major cause of image nonuniformity is due to detector nonuniformity and x-ray field nonuniformity. The scanning slot mammography system is designed so that the slot detector is scanned from one side of the breast to the other side, in a direction parallel to the chest wall. In other words, the long dimension of the slot detector is parallel to the x-ray tube cathode-to-anode axis. The x-ray field nonuniformity mainly stems from the heel effect, which can produce a variation in x-ray exposure by a factor of ~1.5 over a distance of 18 cm away from the chest wall. For a source to detector distance (SDD) of ~ 60 cm and image area of ~ 18 x 24 cm^2, the inverse square law plays a very insignificant role in the x-ray field nonuniformity. For example, this introduce a factor of about 1.05 over a distance of 15 cm at 60 cm SDD. Ignore the effect of inverse square law, a line correction algorithm, which corrects the detector nonuniformity, will be adequate to perform the x-ray field nonuniformity correction over the entire filed.

CHAPTER 3
SCATTERED RADIATION IN SCANNING SLOT MAMMOGRAPHY

3.1. Introduction

3.1.1. Subject Contrast in Mammography

Figure 3-1 illustrates a simplified model of mammographic imaging. A lesion of thickness t is embedded in a uniform background of thickness T. The x-ray attenuation coefficients of the lesion and uniform background are μ' and μ respectively.
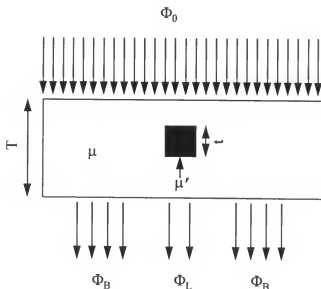
Figure 3-1. Simple model of mammography image formation.

The intensity of primary x-ray photons after penetrating through the uniform background is Φ_B, and given by

$$\Phi_B = \Phi_0 \cdot e^{-\mu T} \tag{3-1}$$

where Φ_0 is the input x-ray photon flux. In the shadow of the lesion, the intensity if penetrating x-ray photons, Φ_L, is given by

$$\Phi_L = \Phi_0 \cdot e^{-\left[\mu(T-t)+\mu' t\right]} \tag{3-2}$$

The subject contrast, C, of the lesion is determined by the difference in x-ray transmission between background and lesion and given by

$$C = \frac{\Phi_B - \Phi_L}{\Phi_B + \Phi_L} \tag{3-3}$$

Using Equations 3-1 and 3-2, the subject contrast will be determined only by the thickness of the lesion and the difference between the lesion attenuation coefficient (and background attenuation coefficient as

$$C = \frac{1 - e^{\left(\mu - \mu'\right)}}{1 + e^{\left(\mu - \mu'\right)}} \tag{3-4}$$

Figure 3-2 shows the linear x-ray attenuation coefficients of various breast tissues as a function of x-ray energy. The data is taken from the measurement data of Jones and Yaffe (1987). The small difference in x-ray attenuation coefficients between breast carcinoma and normal breast tissues shows that the image contrast of a breast lesion at its earlier stages (i.e., when the lesion is small in size) is very low, which makes the detection of breast cancers the most challenging imaging task in diagnostic radiology.

Figure 3-2 also shows that the difference in x-ray attenuation coefficients between the breast carcinoma and normal breast tissues decreases with increasing x-ray energy. Mammography is therefore performed at low x-ray energies to maximize the lesion subject contrast.
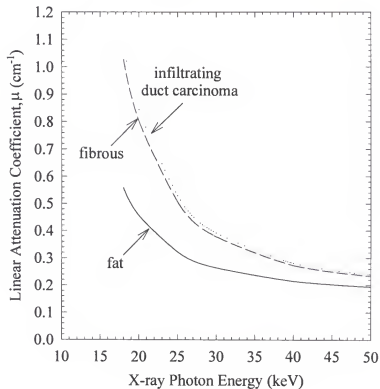
Figure 3-2. Measured x-ray attenuation coefficients of different breast tissues as a function of x-ray energy. Based on results from Jones and Yaffe (1987).

3.1.2. The Effect of Scattered Radiation on Image Contrast

The absorption of photons scattered from breast by the image detector degrades image contrast in the breast images. This makes the perception of microcalcification and small differences in tissue density more difficult. Scattered photons contribute an added x-ray intensity Φ_s to the transmitted x-ray intensity Φ_t. The x-ray image contrast at the breast output is reduced to C_r as given by

$$C_r = C \cdot \frac{I_p}{I_p + I_s} = \frac{C}{1 + \frac{I_s}{I_p}} \qquad (3\text{-}5)$$

where C is the subject contrast. I_s and I_p are the scattered radiation intensity and primary radiation intensity, respectively. $(1 + I_s/I_t)^{-1}$ is the contrast reduction factor. In an x-ray imaging detector where the output is the integration of absorbed x-ray energy, the final image contrast, C_I, is given by

$$C_I = \frac{C}{1 + S/P} \qquad (3\text{-}6)$$

where S/P is the scatter to primary ratio.

S/P is defined as the ratio of the scattered to primary photon energies absorbed by a small area of the image detector. In mammography, S/P is a function of the x-ray energy, x-ray field size, breast composition, as well as breast thickness (Barnes and Brezovich, 1979; Dance and Day, 1984; Yester et al., 1981). In screen-film mammography, grids with either 4:1 or 5:1 ratios and strip line densities of between 30 and 50 per centimeter are typically used to minimize the amount of scatter present on the mammography screen-film combination. These mammographic grids absorb 75% to 85% of the scattered radiation. As a result, the S/P ratio in screen-film mammography may be reduced to between ~0.10 and ~0.30 (Junck et al., 1996). At the same time, however, mammographic grids only transmit 60% to 75% of the primary x-rays. To achieve the optimal film density for display, it is necessary to increase the amount of x-ray tube output to compensate the loss of x-ray photons absorbed by the grid (primarily scattered radiation) in screen-film mammography. This results in increased breast mean glandular doses by a factor of about two (Barnes, 1992; Rothenberg, 1994; Skubic and Fatouros, 1989).

3.1.3. Purpose of This Study

Imaging systems using a scanning slot detector geometry have been evaluated for use in digital mammography. These designs use a collimated fan beam of x-rays with the slot detector moved to cover the whole breast region in about 4 to 6 seconds. The choice of the slot detector width has typically ranged from ~4 mm to ~10 mm (Jing et al., 1994; Toker and Piccaro, 1993; Yaffe, 1993). Use of a smaller slot detector width will be expected to reduce the amount of scattered radiation reaching the detector but will increase the x-ray tube loading. Increasing the slot detector width permits the x-ray tube output to be more efficiently utilized and will enable the use of a shorter imaging time thereby reducing patient discomfort. The size of the slot detector width directly affects the expected value of the S/P ratios. A S/P value of ~0.1 has been reported by Fahrig et al. (1994) who used a 5 cm thick, 30 x 33 cm block of BR12 material with a field size restricted to 16 x 0.93 cm for the slot measurement. A similar S/P value of < 0.15 has also been reported by Feig et al. (1996). Specially designed grids used in conjunction with a scanning slot x-ray detector have been shown to result in large reductions in the S/P ratio, but at the price of an increase in radiation dose (Fahrig et al., 1994). Systematic data on the amount of scattered radiation present in the scanning slot mammography systems, however, are not available in the scientific literature and scatter rejection by the use of air gaps also merits additional examination (Krol et al., 1996; Court and Speller, 1995).

In this chapter, Monte Carlo simulations were performed to calculate the S/P ratios for a slot x-ray detector geometry using x-ray photon energies currently used in screen-film mammography. The relative contributions of Compton and coherent scattering to the total scattered radiation reaching the detector were determined. The dependence of the S/P ratio on the slot detector material was examined. In addition, the scatter reduction by the use of an air gap was assessed and compared to that of using grids in conventional screen-film mammography.

3.2. Monte Carlo Method

3.2.1 Monte Carlo Simulation

In the scanning slot detector geometry, the solid angle of acceptance for a scattered x-ray is much smaller than that encountered in conventional screen-film mammography. In order to perform an accurate Monte Carlo simulation, it is not only important to accurately sample the x-ray interaction processes by their cross sections, but also important to correctly sample the angles of both Compton and coherent scattered x-rays (Jones and Yaffe, 1983).

The EGS4 Monte Carlo code (Nelson et al., 1985) was employed to simulate the x-ray interaction processes in a Lucite phantom and the slot x-ray detector. The atomic electron binding effect on Compton scattering was taken into account by incorporating the changes in the EGS4 code reported by Namito et al. (1995). The effect of molecular structure on coherent scattering in the Lucite breast phantom was included using methods described by Leliveld et al. (1995).

The differential Compton cross section of a bound electron for an unpolarized photon is used:

$$\frac{d\sigma}{d\Omega} = \left(\frac{d\sigma}{d\Omega}\right)_{KN} S(x, Z) \qquad (3-7)$$

where $(d\sigma/d\Omega)_{KN}$ is the well known Klein-Nishina function which assumes the electron struck by the incoming photons in an Compton scattering is initially unbound and stationary. $(d\sigma/d\Omega)_{KN}$ is defined as

$$\left(\frac{d\sigma}{d\Omega}\right)_{KN} = \frac{r_0^2}{2} \left(\frac{h\nu'}{h\nu}\right)^2 \left(\frac{h\nu}{h\nu'} + \frac{h\nu'}{h\nu} - \sin^2\theta\right) \qquad (3-8)$$

where r_0 is the classical electron radius. $h\nu$ and $h\nu'$ are the incident and scattered photon

energies. θ is the scattering polar angle. $S(x, Z)$ is the total molecular incoherent scatter

function which was used to treat the electron-binding effect on the angular distribution of

a Compton scattered x-ray. $S(x, Z)$ was calculated as the weighted sum of the individual

atomic incoherent scatter function, $s(x, Z_i)$, Z_i is the atomic number of the ith atom. x is

the momentum transfer and is related to the incident x-ray energy, E, and scattering polar

angle, θ as

$$x = \frac{E}{hc}\sin\left(\frac{\theta}{2}\right) \tag{3-9}$$

In sampling the coherent scattering angle, the differential coherent scattering cross

section was given by

$$\frac{d\sigma}{d\Omega} = \left(\frac{d\sigma}{d\Omega}\right)_{Th} F(x,Z)^2 \tag{3-10}$$

where $(d\sigma/d\Omega)_{Th}$ is the Thomson differential cross section which describes coherent

scattering of a photon with a free electron. $(d\sigma/d\Omega)_{Th}$ is given by

$$\left(\frac{d\sigma}{d\Omega}\right)_{Th} = \frac{r_0^2}{2}\left(1 + \cos^2\theta\right) \tag{3-11}$$

where θ is the coherent scatter polar angle. $F(x, Z)$ is the total molecular form factor of

the attenuation material. $F(x, Z)$ takes into account the effective charge that scatters the

photon. In the past, $F(x, Z)$ was calculated from the weighting sum of the atomic form

factors of the individual atoms, assuming that all the atoms act independently. However,

it has been shown that the coherent scattering cross section, and most importantly, the coherent scattering angle depend strongly on the molecular structure. Since coherent scattered photons are peaked in the forward direction, the Monte Carlo simulation results for a slot x-ray imaging detector would be in significant error without correcting the molecular structure effect on the coherent scattering differential cross section. Total molecular form factors were available for Lucite (Kosanetzky et al., 1987), and were used in the Monte-Carlo simulations performed.

3.2.2. Simulation Model

Figure 3-3 shows the geometry used in the Monte Carlo simulations.
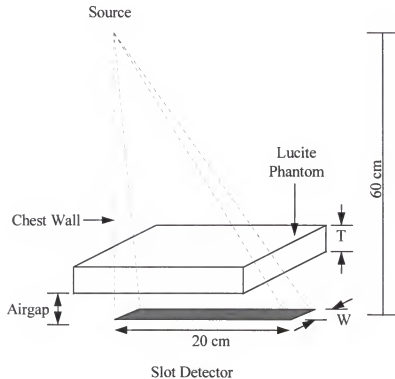
Figure 3-3. Imaging geometry used in Monte Carlo simulations.

The fan beam originates at a point focus and is collimated to the cross-sectional area of the slot detector. The breast was modeled by a homogeneous block of Lucite (20 cm x 20 cm cross sectional area) of thickness T which ranged from 2 to 6 cm. The x-ray source, one edge of the Lucite phantom, and one edge in the short dimension of the slot detector area were aligned at the chest wall as shown in Figure 3-3. The slot detector was aligned with the center of the Lucite phantom with an x-ray source to detector distance of 60 cm. The length of the slot x-ray detector was 20 cm and the slot detector width, W, ranged from 4 mm to 20 mm. Unless otherwise specified, the Monte Carlo simulations had no air gap.

Two slot x-ray detectors were studied. The first detector (Detector 1) was assumed to have a 100% efficiency for absorbing x-ray photons, regardless of their energies and angles of incidence. The second detector (Detector 2) consisted of a 31.7 mg/cm^2 thick Gd$_2$O$_2$S:Tb phosphor as the x-ray detection material. Unless otherwise specified, the Monte Carlo simulations used Detector 1.

3.2.3. X-ray Energy and Breast Phantoms

Monte Carlo simulations were performed using monoenergetic x-ray photons with energies ranging from 15 to 50 keV and for three representative mammographic x-ray energy spectra taken from the measured data of Fewell and Shuping (1978). The x-ray spectra were generated using a Mo target with 30 μm Mo added filtration at x-ray tube potentials of 25, 30, and 35 kVp. The average photon energies of the 25, 30, and 35 kVp x-ray spectra were 17.7, 18.4, and 19.4 keV respectively. As an example, the 30 kVp x-ray spectrum is shown in Figure 3-4. These measured x-ray spectra were generated with an x-ray tube with a glass window, therefore, are different from those x-ray spectra that are generated from the modern mammography x-ray tubes which utilize a beryllium

window to allow the output of lower energy x-rays. However, this difference in x-ray spectra is not expected to have a significant effect on the computed S/P ratios.
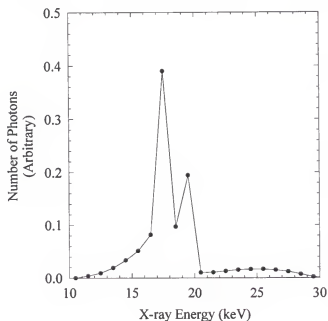
Figure 3-4. A typical mammography 30 kVp x-ray energy spectrum. Based on results from Fewell and Shuping (1978).

The breast phantom is modeled as a homogeneous block of Lucite. Lucite has an effective atomic number, Z_{eff}, of 6.5 which is between those of glandular tissue (7.4) and adipose tissue (5.9). Lucite is used in many mammographic phantoms including the RMI 156 phantom (GAMMEX RMI, Middleton, WI) used for accreditation purposes by the American College of Radiology. Breast tissue is primarily composed of a mixture of adipose, glandular and fibrous tissue. Barnes and Brezovich (1979) have shown that Lucite has the same Z_{eff} as breast tissue composed of 65% fat and 35% tissue. The density of such breast tissue is 0.95 g/cm^3. Since the density of Lucite is 1.19 g/cm^3, a 1 cm thickness of Lucite is equivalent to a 1.25 cm thickness of the above breast tissue.

The major reason Lucite was used is that its molecular form factors are available for Monte Carlo calculations. Fahrig et al. (1994) measured the angular distribution of

scattered photon energy using a breast equivalent material (BR12) and a 30 kVp Tungsten anode x-ray source. This scattered radiation distribution peaked at ~5° which is similar to the distribution of scattered radiation measured from Lucite (Kosanetzky et al., 1997; Muntz et al., 1983). It is therefore reasonable to take the S/P ratios obtained with a Lucite phantom to be generally applicable to the values expected to occur in clinical mammography.

3.2.4. Calculation of Scatter to Primary Ratios

Scatter to primary ratio, S/P, was defined as the ratio of the total scattered x-ray photon energy absorbed by the detector to the sum of the primary x-ray photon energies absorbed, as given by

$$\frac{S}{P} = \frac{\sum_i ES_i}{\sum_j EP_j} \tag{3-12}$$

where ES_i and EP_j are the energies absorbed by the detector from the ith scattered x-ray photon and jth primary x-ray photon reaching the detector, respectively.

In the case of Detector 1, all primary and scattered photons incident on the surface cross-sectional detector area were assumed to be completely absorbed by the detector. In the case of Detector 2, the actual energy absorbed by the detector from each incident x-ray photon was computed. Secondary electrons were assumed to deposit their energies at the interaction sites. Energy deposited in the detector from characteristic x-rays emitted following photoelectric interactions was also included. Statistical errors in the resultant S/P ratios were about 1%.

The effect of an air gap on the reduction of the scatter to primary ratio was quantified by a scatter reduction factor, f, defined as the S/P ratio with no air gap divided

by the S/P ratio with an air gap. Since the S/P ratio is reduced as the air gap is increased, the value of f will be greater than 1.

3.2.5. Validation of Monte Carlo Calculations

Barnes and Brezovich (1979) have reported some measurements of S/P ratios as a function of circular x-ray field diameter using a 32 kVp x-ray energy spectrum. In this study, simulations were performed to repeat their measurements using the average energy of that experimental 32 kVp x-ray spectrum, 24.5 keV. S/P values were computed as the ratio of scattered to primary x-ray photon energy absorbed by an area of 2 mm diameter in the center of the detector. Table 3-1 gives a summary of their measured S/P values at 32 kVp and the corresponding predictions of our Monte Carlo computations. The differences between the predicted and measured S/P values are less than 10% and 5% for the 3 cm and 6 cm Lucite phantoms, respectively. The agreement between measurement and calculation is good and this provides a useful check on the validity of the calculations.

Table 3-1. S/P values vs. circular x-ray field diameter (d) for two Lucite phantom thicknesses (T). The experimental results were taken from the measurements of Barnes and Brezovich (1979).

d	Experimental Results		Present Calculation	
(cm)	T = 3 cm	T = 6 cm	T = 3 cm	T = 6 cm
4	0.32	0.54	0.33	0.54
6	0.37	0.65	0.39	0.68
10	0.39	0.80	0.42	0.84
14	0.40	0.86	0.44	0.89

3.3. Scatter to Primary Ratios

3.3.1. Dependence of S/P Ratio on Slot Detector Width

Table 3-2 shows the dependence of the S/P ratio on the slot detector width (W) for a 4 cm thick Lucite phantom. The S/P ratio decreased by a factor of ~2.5 when W was reduced from 20 mm to 4 mm at all photon energies. Differences in S/P ratios between 20 keV photons and 30 kVp spectra were less than 6%. Average differences in S/P ratios were less than 5% between 25 kVp and 30 kVp spectra, and less than 10% between 25 kVp and 35 kVp spectra.

Table 3-2. S/P values as a function of slot detector width (W) for a 4 cm thick Lucite phantom.

W (mm)	20 keV	25 keV	30 keV	25 kVp	30 kVp	35 kVp
4	0.150	0.132	0.123	0.156	0.152	0.143
6	0.192	0.184	0.176	0.204	0.189	0.185
8	0.238	0.215	0.208	0.242	0.231	0.226
10	0.268	0.239	0.234	0.280	0.266	0.252
15	0.345	0.302	0.288	0.335	0.331	0.311
20	0.371	0.352	0.343	0.391	0.372	0.336

3.3.2. Dependence of S/P Ratio on Lucite Phantom Thickness

Figure 3-5 (a), (b) and (c) show the S/P ratios as a function of Lucite phantom thickness (T) for the 4 mm, 10 mm, and 20 mm wide slot detectors, respectively. At 20 keV, the S/P ratio ranges from 0.12 to 0.17 for the 4 mm wide slot detector, between 0.18 to 0.33 for the 10 mm wide slot detector, and between 0.22 to 0.52 for the 20 mm wide

slot detector. The S/P ratio decreased by ~10% as the x-ray energy increased from 20 to 25 keV. Average differences in the S/P ratio between 25 and 30 keV were ~3%.

(a)   (b)

(c)
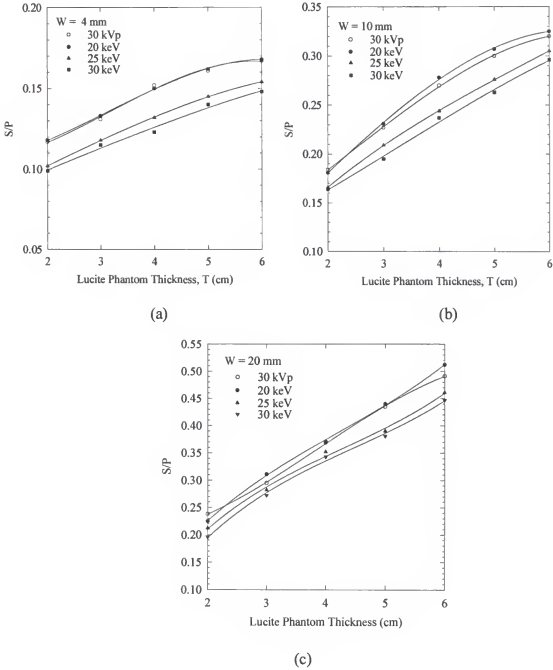
Figure 3-5. S/P ratios as a function of Lucite phantom thickness (T) for the (a) 4 mm wide, (b) 10 mm wide, and (c) 20 mm wide slot x-ray detectors.

The S/P ratios for a 4 mm wide slot detector were between 0.10 to 0.17, which are similar to those encountered in conventional screen-film mammography when a 5:1 ratio grid is used. Increasing the slot detector width to 10 mm resulted in an increase in the S/P ratio by a factor of ~1.8. The x-ray tube heat loading for a 10 mm wide slot detector is only 40% of that of a 4 mm wide slot detector. Efficient use of the x-rays generated in the x-ray tube would reduce the scan time and thereby minimize patient motion artifacts as well as patient discomfort. In addition, more efficient use of the x-ray beam would enable filters to be used to optimize the shape of the x-ray spectrum to better match the imaging needs in clinical situations.

3.3.3. Dependence of S/P Ratio on Incident X-ray Photon Energy

Figure 3-6 shows the S/P ratio as a function of x-ray energy for a 10 mm wide slot detector at 2, 4, and 6 cm Lucite phantom thicknesses. For a 4 cm thick Lucite phantom, the S/P ratios decreased as x-ray energy increased with a reduction of about 33% between 15 and 50 keV.

For the slot detector geometry considered in this study, the S/P ratios decreased as the photon energy increased. This differs from the case of mammography performed with large area detectors where the S/P ratios generally shown little dependence on the x-ray energy. The reason for this behavior is that in a slot detector geometry, it is only the forward scattered photons which contribute to the S/P ratio. Whereas in area detectors, photons scattered through large angles can also reach the detector and therefore contribute to the S/P ratio. The relatively constant energy dependence of the S/P ratio for area detectors is a result of the increasing contribution of Compton scattered photons which increase with photon energy (see Figure 3-10) and decreasing contribution of Coherent scattered photons which are primarily forward scattered and their contribution to the S/P ratio generally decreases with increasing photon energy. In a slot detector geometry, the

initial dominance of Coherent scattering at low x-ray energies diminishes at higher x-ray energies thereby leads to a reduction of S/P ratios with increasing x-ray energy.
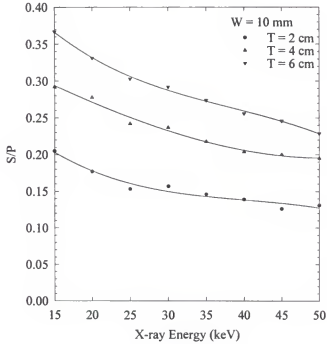
Figure 3-6. S/P as a function of x-ray energy for a 10 mm wide slot detector at 2, 4, and 6 cm Lucite phantom thicknesses.

3.3.4. S/P Ratio Profile in the Slot Detector Plane

Figure 3-7 shows the positional variation of S/P ratio for a 4 cm Lucite phantom at 20 keV in a 10 mm wide slot detector. In this calculation, the 20 cm slot detector length was equally divided into 200 sections. S/P ratios were calculated for each 10 mm x 1 mm area along the slot detector length.

As can be expected from the size of the phantom volume from which scattered radiation can reach a given point in the slot detector, the S/P ratios at the edges of the slot detector are about 50% of that at the center of the slot detector. In the majority (center 16

cm long) of the slot detector area, S/P ratios remains constant. In some analysis of scatter effect on image contrast and signal-to-noise ratio, it was generally assumed that S/P ratios are independent of the position on the detector. It is a reasonable assumption as long as the object to be detected is located on the center portion of the detector.
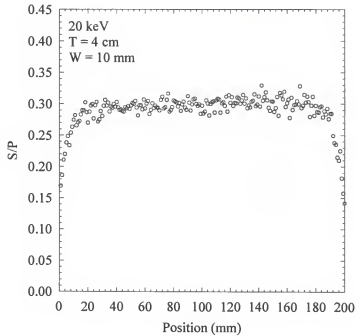
Figure 3-7. S/P ratio as a function of position in the slot detector plane for a 10 mm wide slot detector at 20 keV. The Lucite phantom thickness is 4 cm.

3.4. Practical Considerations of Scatter in Scanning Slot Mammography

3.4.1. Scatter rejection by Air Gap Method

Figure 3-8 shows the dependence of the S/P ratio on the air gap introduced between the Lucite phantom and a 10 mm wide detector. S/P ratio was reduced by a factor of about two and three using 1.5 cm and 3 cm air gaps, respectively. The S/P ratio

was in the range of 0.05 to 0.13 with a 3 cm air gap. Differences in the S/P ratio between 20 keV photons and the 30 kVp spectrum were ~3%.
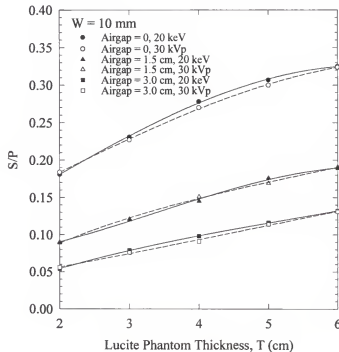
Figure 3-8. S/P as a function of Lucite phantom thickness (T) for a 10 mm wide slot detector at Airgap = 0, 1.5, and 3.0 cm. The results are shown in solid and dashed curves for 20 keV and 30 kVp x-ray sources, respectively.

Table 3-3 gives the resultant values of the scatter reduction factor, f, as a function of Lucite phantom thickness for the two air gaps at 20 keV. The values of f were found to decrease with increased Lucite phantom thickness. This result is expected for the same reason that the observed increase in S/P ratio with phantom thickness is sublinear. The increase in the phantom thickness for a constant (or no) air gap results in an additional layer of material which will contribute proportionally less to the scattered radiation in the detector. The reason is that there is an effective air gap (equal to the original phantom thickness) for scattered photons produced in this additional layer of material. Clearly the relative importance of the additional layer will decrease with increasing air gap which is

responsible for the decrease of scatter reduction factor with increased phantom thickness as depicted in Table 3-3.

Table 3-3. Scatter reduction factor, f, vs. Lucite phantom thickness (T) for two air gaps at 20 keV x-ray energy.

T	Airgap (cm)	
(cm)	1.5	3.0
2	2.01	3.35
3	1.93	2.92
4	1.92	2.84
5	1.74	2.65
6	1.72	2.46

Figure 3-9 shows how the S/P ratios vary as a function of air gap size for slot detector widths ranging from 2.5 mm to 20 mm as computed for a 30 kVp x-ray spectrum and a 4 cm thick Lucite phantom. When no air gap introduced, S/P ratios reduce by nearly a factor of two when the slot detector width changes from 5.0 mm to 2.5 mm. This is the reason that a very small slot detector width is desired for scanning slot mammography for the purpose of improving image contrast. The fraction of scatter present in a slot detector geometry with 2.5 mm slot width and no air gap would be equivalent to that in a slot detector geometry with 10 mm slot width and a 3 cm air gap. Scatter rejection by the air gap method is also more efficient at smaller slot detector width. With the use of a 3 cm air gap, S/P ratios decreased by a factor of 4.25, 3.37, 2.83, and 2.07 for slot detector widths of 2.5, 5.0, 10, and 20 mm, respectively.

Despite of all the advantage of scatter rejection at smaller slot detector width, the minimum slot width is practically limited by the available x-ray tube power and heating capacity. The optimization of slot detector width is therefore to achieve the maximum scatter rejection at reasonable x-ray tube loading requirement. For current mammography

x-ray tube technology, the use of a 10 mm wide slot detector with a 3 cm air gap geometry would provide an optimized balance between scatter rejection and x-ray tube loading requirement.
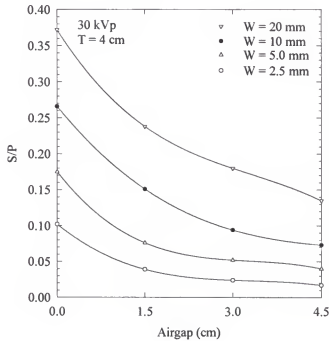
Figure 3-9. S/P as a function of Airgap for the slot detector widths of 2.5, 5, 10, and 20 mm using a 4 cm thick Lucite phantom and a 30 kVp x-ray spectrum.

3.4.2. Relative Contributions from Compton and Coherent Scatter

Figure 3-10 shows the S/P ratio as a function of x-ray energy for a 4 cm thick Lucite phantom and the effect on the S/P ratio from the introduction of a 3 cm air gap. Also shown in Figure 3-10 are the contributions of coherent scatter ($(S/P)_{Coh}$) and Compton scatter ($(S/P)_{Comp}$) to the total scatter. With no air gap, the $(S/P)_{Coh}$ ratio was greater than the $(S/P)_{Comp}$ ratio below about 25 keV. With a 3 cm air gap, however, the
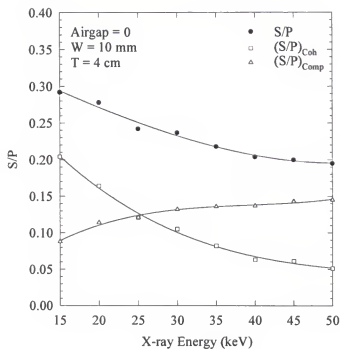
(a)
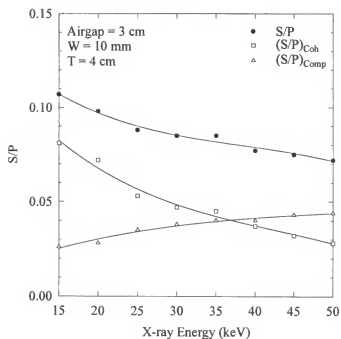
(b)

Figure 3-10. S/P as a function of x-ray energy for the 4 cm thick Lucite phantom and a 10 mm wide slot detector at (a) Airgap = 0; and (b) Airgap = 3.0 cm.

contributions from these two scatter processes were equal at an x-ray energy of ~36 keV. The scatter reduction factor, f, averaged about 2.8 and showed little dependence on the x-ray energy over the range of 15 to 50 keV.

At 20 keV, there are about four times more photons which undergo Compton scattering than coherent scattering in the Lucite phantom. Despite this fact, the contribution of coherent scatter to the S/P ratios is larger than that of Compton scatter at energies below 25 keV as shown in Figure 3-10(a). This occurs because most coherently scattered photons have a small angular divergence whereas the angular distribution of Compton scattered photons is approximately isotropic. This also explains why an air gap is more efficient in rejecting the Compton scattered photons and why the two processes make equal contributions at a higher photon energy (~36 keV) with the 3 cm air gap shown in Figure 3-10(b).

3.4.3. Dependence of S/P Ratio on X-ray Detection Materials

Figure 3-11 (a) to (d) shows the effect of the x-ray detector material on the S/P ratios for a 10 mm wide slot detector at 20, 25, and 30 keV x-ray energies and for a 30 kVp x-ray spectrum. The S/P ratio obtained using Detector 2 (i.e., 31.7 mg/cm^2 thick Gd_2O_2S:Tb phosphor) was ~7% higher than that of Detector 1. The introduction of a 3 cm air gap reduced the difference between the S/P ratios obtained with these two detectors to ~ 4%.

X-ray detection materials currently under investigation for scanning slot digital mammography include Gd_2O_2S:Tb phosphor, CsI:Tl crystal, plastic scintillating fiber screens, and hybrid photodiode array. The data in Figure 3-11 show that choice of x-ray detection material in a slot detector had very little effect on the resultant S/P ratio. In the case of area detectors, however, the S/P ratios of an ideal screen and a Min-R screen
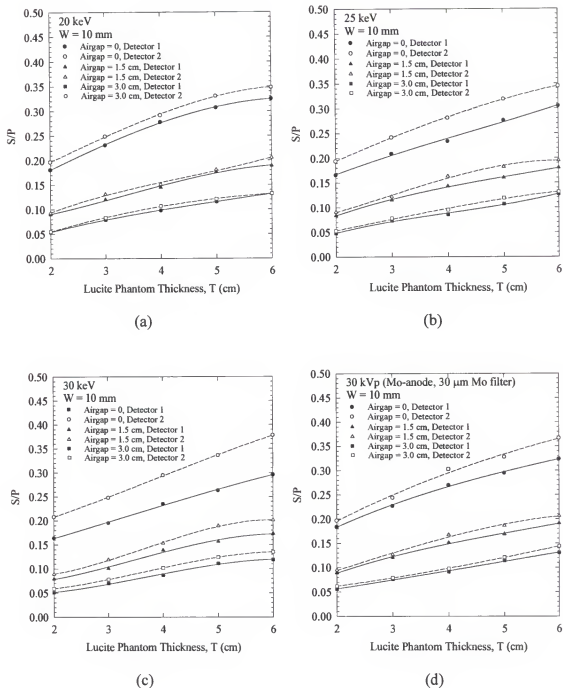
Figure 3-11. S/P as a function of Lucite phantom thickness for an ideal detector with 100% absorption efficiency (plotted in solid lines) and a Min-R screen (plotted in dashed lines) using a 10 mm slot width at (a) 20, (b) 25, (c) 30 keV x-ray energies and (d) a 30 kVp x-ray spectrum.

show markedly different responses. The reason why a slot detector geometry shows little dependence on the detector material is that most scattered photons reaching the slot detector have directions and energies which are similar to those of the primary photons. This finding suggests that the results obtained in this study will be applicable to any type of detection material providing the geometry is similar to those investigated in this work.

3.4.4. The Effect on Patient Dose by the Use of an Air Gap

In conventional screen-film radiography, scattered radiation is rejected by the use of grids. The radiation exposure to the screen, however, needs to be maintained at a constant level to ensure that the resultant film density is satisfactory. This requires an increase in the x-ray tube output to compensate for any removed scattered and primary x-ray photons, and normally leads to an approximate doubling of the mean glandular dose. Use of a scatter reduction grid with a digital slot detector increased the mean glandular dose by between 30 and 40% as a result of the increased attenuation of the primary x-ray beam. Air gaps can achieve scatter reduction without necessarily increasing the radiation dose and are an attractive option for use in a slot detector geometry particularly since the air gaps which are likely to be employed are much smaller than those normally considered in conventional screen-film mammography.

The effect on the patient dose by the use of an air gap with a slot detector geometry will depend on both the characteristics of the detector, and on the manner in which the air gap is introduced. If the detector is quantum noise limited, there will be no need to increase the primary exposure to maintain the same SNR providing the source to detector distance is kept constant. However, if there is a significant electronic noise component from the detector, then an increase in the x-ray tube output would be needed to maintain the same SNR. For a 3 cm air gap introduced by moving the detector away

from the patient, the patient dose would increase by about 10% because of the inverse square law fall off in x-ray beam intensity for a source to detector distance of ~60 cm.

CHAPTER 4
SIGNAL TRANSFER IN THE SLOT X-RAY DETECTORS

4.1. Scanning Slot X-ray Detectors

4.1.1. Introduction

Scanning slot digital x-ray imaging systems are being developed for full-field mammography. There are many factors which affect the imaging performance of these systems. The most challenging work is in the development of the slot x-ray imaging detector which determines, to a large extent, the final image quality achievable with a particular system.

Almost all the slot x-ray detectors have utilized a slot shaped scintillation screen optically coupled to charge coupled devices (CCD) through the use of fiber optical image guide. These slot x-ray detectors can be treated as consisting of serially cascaded components in which the image signals (x-rays, scintillation light, and electrons) propagate. The final image signal of the slot x-ray detector is determined by the amount of x-rays interacted in the scintillation screen, the amount of x-ray energy absorbed per x-ray interaction within the scintillation screen, the energy conversion efficiency of the scintillation screen, the efficiency with which the scintillation light photons are transmitted by the scintillation screen, the coupling efficiency of the fiber optical image guide, and the quantum efficiency with which the light quanta are converted to electrons in the CCD.

In this study, signal propagation and signal distribution as a function of spatial frequency f, modulation transfer function (MTF(f)), in the scanning slot x-ray detectors

are investigated. The signal performances of two novel scintillation screen materials are investigated and compared to the Gd_2O_2S:Tb phosphor screen, which has been used in the previous slot x-ray detector designs.

4.1.2. Scintillating Fiber Screen Based Slot X-ray Detector

Figure 4-1 shows a scanning slot x-ray detector using a plastic scintillating fiber screen (**SFS**). Scintillation light produced from x-ray absorption is channeled to the CCDs through the extension of plastic scintillating fibers. The initial ~2 cm length of the plastic scintillating fibers are aligned to the direction of incident x-ray. The continuous use of plastic scintillating fibers as the image guide could provide efficient optical coupling between the scintillating fiber screen and CCD.
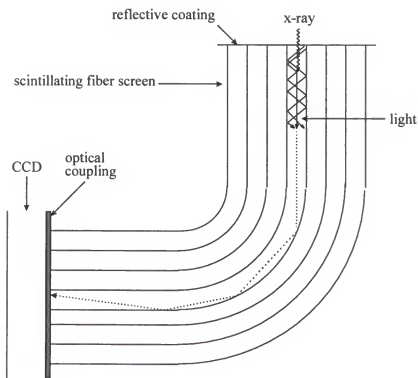
Figure 4-1. A plastic scintillating fiber screen based slot x-ray detector

Two types of high Z element loaded SFSs were compared to that of a pure polystyrene (PS) based plastic SFS, **SFS:PS**. One SFS contains 10% by weight of tin element in its scintillating fiber core material, **SFS:Sn:10%**. The other is loaded with 5% by weight of lead, **SFS:Pb:5%**. To investigate the effect of high Z element concentration on signal propagation within the SFS, two more SFSs loaded with 7.5% by weight of tin (**SFS:Sn:7.5%**) and 5% by weight of tin (**SFS:Sn:5%**) were considered.

Table 4-1 summarizes the energy conversion efficiency (ε), the light loss (L) due to the reabsorption of the scintillating dye in each SFS, the fraction (q) of the scintillation light lost due to quenching.

Table 4-1. Energy conversion efficiency (ε), light loss (L) due to reabsorption of the scintillating dye, and fraction (q) of the scintillation light lost due to quenching for the five plastic scintillating fiber screens investigated in this study.

	SFS:PS	SFS:Pb:5%	SFS:Sn:10%	SFS:Sn:7.5%	SFS:Sn:5%
ε (%)	4.5	4.5	4.5	4.5	4.5
L (%)	15	15	15	15	15
q (%)	0	20	20	15	10

All the slot shaped SFSs investigated were 2 cm in thickness, 0.8 cm wide and 20 cm long. The diameter, d, of the plastic scintillating fibers was 20 μm.

Furthermore, the effect of the thickness of 7.5% by weight tin loaded SFSs, and the effect of the diameter, d, of the individual scintillating fibers on the image signal generation and MTF(f) were also investigated as a function of x-ray energy.

As described in Chapter 2, the fraction, F, of scintillation light collected and transmitted in one direction along each fiber is 7.5%. A reflection layer at the SFS input side reflects 80% of the light transmitted to this direction back to the SFS output. The light loss during the transmission of scintillation light in the continuous fiber image guide is estimated to be 10%.

The average energy of the scintillation light is 2.34 ev (530 nm), where the quantum efficiency (QE) of the CCD is 40%. This value is used for the analysis of light to CCD electrons conversion in the SFS based slot x-ray detectors.

4.1.3. A CsI:Tl Screen Based Slot X-ray Detector

Figure 4-2 shows a CsI:Tl screen based slot x-ray detector. The 150 μm thick CsI:Tl screen is optically coupled to the CCD by a fiber optical image guide with 1:1 input output ratio.
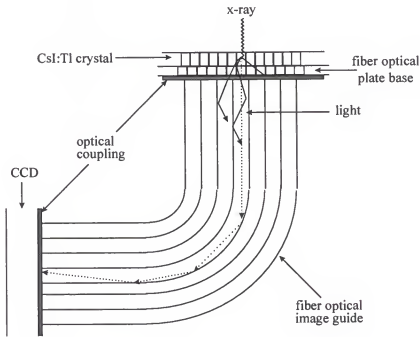
Figure 4-2. A CsI:Tl screen based slot x-ray detector.

The CsI:Tl screen is composed of columnar CsI crystals with air gap between them. As scintillation light reaching the CsI crystal surface, a large fraction of scintillation light with angles less than the critical angle of 56.3°, as determined by the refractive indexes of CsI crystal (n_{CsI} = 1.80) and air (n_{air} = 1), will be reflected back to

the CsI crystal. This fiber-like structure minimizes the lateral spread of scintillation within the CsI:Tl screen.

As mentioned in Chapter 2, the CsI crystals were grown on a glass fiber optical plate supporting base. This supporting base is 3 mm thick and incorporates extra-mural absorber (EMA) material to absorb light that penetrates the fiber core/cladding interface. The numerical aperture (NA) of the fibers in the base is 1.0. NA is determined by the refractive indexes of the core (n_{core} = 1.82) and the cladding (n_{clad} = 1.495) as

$$NA = \sqrt{n_{core}^2 - n_{clad}^2} \tag{4-1}$$

As shown in Figure 4-3, NA also determines the angle (θ) at which the scintillation light enters the fiber from the CsI crystal.
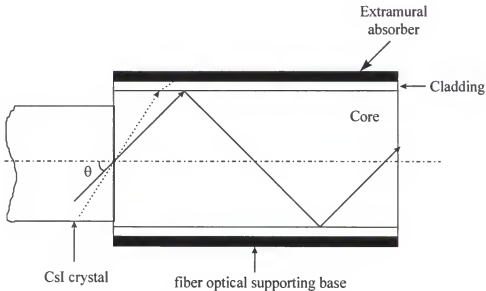
Figure 4-3. A simplified diagram of scintillation light collection and transmission by the glass fiber optical plate supporting base.

The relationship between NA and θ is given by

$$NA = n_{CsI} \cdot \sin\theta \qquad (4\text{-}2)$$

θ is calculated to be 33.7°. Due to this restricted angle of acceptance for scintillation light originating in the CsI crystals, the light emission from the CsI:Tl screen (CsI crystals plus supporting base) is peaked in the forward direction.

The x-ray energy conversion efficiency, ε, of the CsI:Tl crystal is 12%. The average number of light photons (average energy is 2.3 eV) exiting the CsI:Tl screen per keV energy deposition, K, has been measured to be 4 photons/keV by Okumura et al.(1995). In the measurement, Am-241 radioisotope (γ-ray energy 59.6 keV) was used. The scintillation pulse height spectrum was measured by reading the CsI:Tl screen light out using a photomultiplier tube. The scintillation pulse height spectrum was also measured for a standard NaI:Tl crystal with known number of light photons emitted per unit of x-ray energy deposition. By comparing the photopeaks in the two spectra, the number of light photons exiting the CsI:Tl screen per 59.6 keV energy deposition can be calculated.

The image guide is made of 6 μm glass optical fiber with (NA) equal to 1.0. In the interfaces between CsI:Tl screen and image guide and between image guide and CCD, optical coupling gel with refractive index value of 1.48 was applied to provide stable connection, optical alignment, and matching of refractive indexes between two optical components. The coupling efficiency of this image guide is determined by the angular distribution of the scintillation light emitted from the CsI:Tl screen, the packing fraction (i.e., fraction fiber core area in the total image guide cross sectional area) of the image guide, NA of image guide, refractive indexes of the coupling gel, and the transmission efficiency of the optical fiber. Because scintillation light emitted from the CsI:Tl screen is peaked in the forward direction and is within the accepted angle of the image guide, the coupling efficiency is given by the product of the image guide packing fraction (80%) and

transmission efficiency (85%) of the optical fiber. A coupling efficiency value of 68% was used for the image guide in CsI:Tl screen based slot x-ray detector.

The scintillation spectrum of the CsI:Tl screen is very close to that from the plastic scintillating fiber screen. A CCD quantum efficiency of 40% is also applied to analysis the signal propagation in the CsI:Tl screen based slot x-ray detector.

4.2. Methods

4.2.1. Quantum Accounting Diagram

In x-ray imaging, an imaging system is often described as a series of cascaded stages according to the physical processes involved in the signal (**quanta**) transfer (Cunningham et al., 1994; Maidment and Yaffe, 1995; Maidment and Yaffe, 1996). In this model, the quanta leaving a previous stage constitutes an effective input to the subsequent stage. Primary input quanta (i.e., x-rays) are converted to secondary quanta through one or more stages before contributing to the final image. Each stage has a gain or efficiency associated with it. The average number of quanta in each stage, given by the product of the average gains and efficiencies of all proceeding stages, can be represented in a diagram where the average number of quanta at each stage is plotted as a function of the stage number. This diagram is called a quantum accounting diagram (QAD) and is a powerful analytic tool which can identify the "quantum sink" in a imaging system and allow for the optimization of an imaging system..

In the slot x-ray detectors discussed in section 4.1.2 and 4.1.3, a total of four cascaded stages can be used to represent the quanta propagation:

Stage 1: X-ray interaction within the screen. For each x-ray incident on the slot x-ray detector, x-ray interaction efficiency, η, gives the average probability in percentage that this x-ray will interact within the scintillation screen.

Stage 2: X-ray to light conversion and light transmission within the screen. For each interacted x-ray, the average number of light photons emitted from the scintillation screen, N_{exit}, is given by

$$N_{exit} = \frac{E_d}{E_L} \cdot \varepsilon \cdot \xi \qquad (4\text{-}3)$$

where E_d is the average x-ray energy deposited per incident x-ray interaction,. E_L, is the average energy of scintillation light photons, ε is the x-ray to light conversion efficiency of the scintillation screen. ξ is the scintillation light transmission efficiency of the scintillation screen.

Stage 3: The transmission of light to the CCD. The average number of light photons reaching the CCD, N_{CCD}, is given by

$$N_{CCD} = N_{exit} \cdot \kappa \qquad (4\text{-}4)$$

where κ is coupling efficiency of the fiber optical image guide.

Stage 4: The conversion of light to electrons in the CCD pixel. The average number of electrons generated in the CCD, N_e, is given by

$$N_e = N_{CCD} \cdot Q \qquad (4\text{-}5)$$

where Q is the average quantum efficiency of the CCD to the light emitted from the scintillation screen.

The QAD analysis of an imaging system is informative and permits the optimization of the imaging system, for example, by optimizing the efficiency or gain of a particular stage. QAD also allows the estimation of the fundamental noise limitations of

particular system designs. For example, the stage with the fewest quanta is usually called the "quantum sink". QAD analysis of an imaging system, however, does not provide any information on the location of quanta that are generated in each stage. Some stages usually involve a scattering and spreading process that results in a finite spatial distribution of secondary quanta, such as the light dispersion in the scintillation screen. QAD analysis integrates the number of quanta over all space at each stage, and, is called the zero spatial frequency analysis of quanta propagation in an x-ray imaging system.

4.2.2. Modulation Transfer Function

In the spatial domain (as opposed to the spatial frequency domain), the spatial spread of the secondary quanta in each stage can be described by its point spread function (PSF(x,y), where x and y are the orthogonal spatial coordinates) or line spread function (LSF(x) or LSF(y)). PSF(x,y) is the secondary quanta image obtained from an infinitesimal point input of the primary quanta. LSF(x) is obtained with an infinitesimal slit input of the primary quanta. LSF(x) is therefore a one dimensional representation of the two dimensional PSF(x,y). LSF(x) is related to PSF(x,y) as:

$$LSF(x) = \int_{-\infty}^{+\infty} PSF(x,y)dy \qquad (4-6)$$

In the past, modulation transfer function has been used successfully to characterize the resolution properties of x-ray imaging systems (Dainty and Shaw, 1974; Giger and Doi, 1984, Metz and Doi, 1979). Modulation transfer function, MTF(f), where f is the spatial frequency, can be obtained from the Fourier transform of LSF(x) as given by:

$$MTF(f) = \left| \int_{-\infty}^{+\infty} LSF(x) \cdot e^{-2\pi \cdot i \cdot f \cdot x} dx \right| \qquad (4\text{-}7)$$

For a linear, shift invariant imaging system, the total system MTF(f) is given by the product of the $MTF_i(f)$ of each individual stage in the image formation as

$$MTF = MTF_1(f) \cdot MTF_2(f) \cdot MTF_3(f) \cdots \qquad (4\text{-}8)$$

where $MTF_1(f)$, $MTF_2(f)$, $MTF_3(f)$ are the MTF(f) of the first, second, and third stages in the imaging system. In this study, equation 4-8 is applied to analysis the MTF(f) of the slot x-ray detector. The slot x-ray detector MTF, $MTF_{Detector}(f)$, is given by

$$MTF_{Detector}(f) = MTF_{screen}(f) \cdot MTF_G(f) \cdot MTF_{CCD}(f) \qquad (4\text{-}9)$$

where $MTF_{screen}(f)$, $MTF_G(f)$, and $MTF_{CCD}(f)$ are the MTF(f) of the scintillation screen, fiber optical image guide, and the CCD, respectively.

4.2.3. Monte Carlo Calculation

The EGS4 Monte Carlo code was used to calculate the x-ray absorption in the scintillation screens. In all simulations, x-rays from a point source were normally incident on the scintillation screen. Three x-ray interaction processes with the scintillation screen were included: Compton scattering, coherent scattering, and photoelectric effect. Scattered x-rays can either interact again in a remote location within the scintillation screen, or escape without being absorbed. The emission of characteristic x-rays following photoelectric interactions were included. The Compton recoil electrons, photoelectrons and Auger electrons have very low energies and were assumed to deposit their energies in the x-ray interaction sites.

X-ray interaction efficiency, η, was computed as the fraction of incident x-rays which interacted within the SFS as given by

$$\eta = \frac{N_{interact}}{N_{History}} \cdot 100\% \tag{4-10}$$

where $N_{interact}$ is the total number of incident interacted within the scintillation screen, $N_{History}$ is the history (i.e., total number of incident x-rays) from each simulation.

For the plastic scintillating fiber screen (SFS), the average number, N_{exit}, of visible photons exiting the SFS per interacted x-ray was calculated using the equation

$$N_{exit} = E_d \cdot \varepsilon \cdot (1 - L) \cdot (1 - q) \cdot F \cdot 1.8 / 2.34 \tag{4-11}$$

where E_d (in eV) is the average energy deposition per incident x-ray photon, F is scintillation light collection efficiency. E_d is obtained from the Monte Carlo simulation. As described in Chapter 2, a F value of 7.5% is used in this analysis. A numerical constant, 1.8, accounts for the 80% light reflection from the reflective layer painted in the input surface of a SFS. The average energy of the scintillation light is 2.34 eV.

For the CsI:Tl screen, N_{exit} is calculated as

$$N_{exit} = E_d \cdot K \tag{4-12}$$

In a scintillation screen, two stages in the image formation determine its spatial resolution. First, x-ray interactions within the scintillation screen include Compton scattering, coherent scattering, and photoelectric effect. An incident x-ray undergoes single or multiple interactions before being totally absorbed or scattered out of the scintillation screen. Following the photoelectric absorption, there are also characteristic x-

rays which could be emitted isotropically and reabsorbed again within the screen (Arnold and Bjarngard, 1979). These lead to a spread of incident x-ray energy deposition from the primary interaction site. Second, the emitted light is propagated to the screen output which causes a lateral dispersion of scintillation light with the scintillation screen.

The total MTF(f) of a scintillation screen, MTF$_{screen}$(f), is therefore given by

$$MTF_{screen}(f) = MTF_E(f) \cdot MTF_o(f) \qquad (4-13)$$

where, MTF$_E$(f) is the spatial resolution of the incident x-ray energy spread. MTF$_O$(f) is the spatial resolution of the scintillation light spread.

To compute MTF$_E$(f), the point spread functions, PSF$_E$, of the spread of x-ray energy deposition were generated. The SFS was divided into a two dimensional array composed of squares of 5 μm^2 size. Total energy deposition, E$_{i,j}$, inside a square centered at (x_i, y_j) from the normally incident pencil beam of x-rays was calculated. By definition, we have PSF$_E$ = E$_{i,j}$. The line spread function, LSF$_E$, of this deposited energy spread was calculated by integrating the point spread function in one dimension. LSF$_E$ is therefore given by

$$LSF_E = \sum_{j=-\infty}^{+\infty} E_{i,j} \qquad (4-14)$$

MTF$_E$ was obtained from the modulus of the Fourier transform of the LSF$_E$.

4.2.4. Scintillation Screen Optical MTF

For a SFS made of uniformly packed scintillating fibers of same diameter, d. The scintillation light is channel down each individual fiber by the total reflection principle. MTF$_O$(f) of an SFS is therefore given by

$$\text{MTF}_\text{o}\left(f\right) = \frac{\sin\!\left(\pi \cdot f \cdot d\right)}{\pi \cdot f \cdot d} \tag{4-15}$$

Okumura et al. (1995) has measured the contrast transfer function, CTF(f), of the 150 μm thick CsI:Tl screen by taking the x-ray images of the square wave resolution charts. In their experiment, the resolution charts were placed in direct contact with the CsI:Tl screen input side. A tungsten (W) anode x-ray tube was used and images were taken at x-ray tube potential of 40 KV with no additional filtration. Figure 4-4 shows the measured CTF(f) from this measurement.
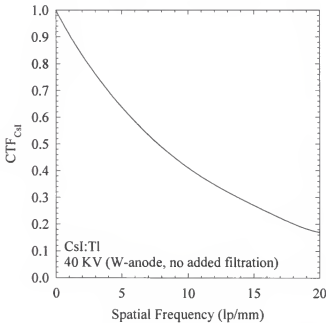
Figure 4-4. Measured contrast transfer function, CTF(f), for the 150 μm thick CsI:Tl screen. Based on results from Okumura et al., 1996.

Although MTF(f) and CTF(f) are similar in many respects, the difference is that CTF(f) describes a system's ability to image line pairs (as seen on the square wave resolution objects), whereas MTF(f) describes its ability to image sine-wave shapes, or

spatial frequencies. A major advantage of MTF(f) that is not possessed by CTF(f) is the MTF(f)'s ability to be cascaded.

In this study, the Coltman relational equation is used to convert the measured CsI:Tl screen CTF(f) to a MTF(f), as given by

$$MTF(f) = \frac{\pi}{4}\left[CTF(f) + \frac{1}{3}CTF(3f) - \frac{1}{5}CTF(5f) + \frac{1}{7}CTF(7f) - \frac{1}{9}CTF(9f) + \cdots\right] \quad (4\text{-}16)$$

The optical MTF for the 150 μm thick CsI:Tl screen was then determined using equation 4-13. The energy deposition MTF, MTF$_E$(f), was computed from Monte Carlo simulation using a 40 KV x-ray spectrum as shown in Figure 4-5. The spectrum was obtained from the measurement data for a Tungsten anode with no added filtration.
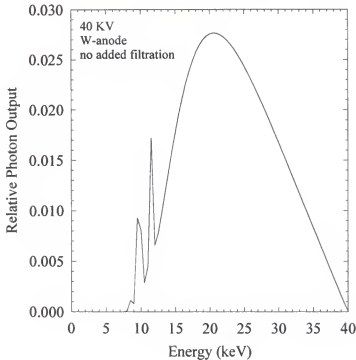
Figure 4-5. A 40 KV x-ray spectrum used in the measurement of CsI:Tl screen CTF(f).

4.3. Signal Propagation in the Slot X-ray Detectors

4.3.1. X-ray Interaction Efficiency

The x-ray interaction efficiency is shown in Figure 4-6 as a function of incident x-ray energy for three types of SFSs of 2 cm thickness and a Kodak Min-R screen. The data for the Min-R screen were obtained from the Technical data (1989) provided by the manufacturer. Loading high Z elements into a plastic SFS significantly improved its x-ray interaction efficiency. X-ray interaction efficiency of SFS:Sn:10% or SFS:Pb:5% was significantly higher than the x-ray interaction efficiency of the Kodak Min-R screen.
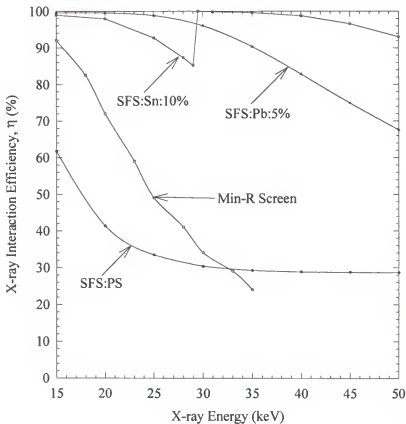
Figure 4-6. X-ray interaction efficiency for three 20 mm thick SFSs and for a Kodak Min-R phosphor screen.

Figure 4-7 (a) shows the dependence of x-ray interaction efficiency on the concentration of tin element in the SFS. Figure 4-7 (b) shows the dependence of x-ray interaction efficiency on the thickness of the SFS:Sn:7.5%. As expected, x-ray interaction efficiency improves with increased tin concentration in the SFS. However, this increase in x-ray interaction efficiency is relatively small at mammographic x-ray energies. For example, at 20 keV, there is about 5% and 2% increase in x-ray interaction efficiency when the concentration of tin increases from 5% to 7.5% and from 7.5% to 10%, respectively. The x-ray interaction efficiency increases with increasing SFS:Sn:7.5% thickness. It is seen that the use of a 2 cm thick SFS:Sn:7.5% provides sufficient x-ray interactions with the SFS:Sn:7.5%. The x-ray interaction efficiency is greater than 80% at x-ray energies below tin K-edge (29.2 keV) for the 2 cm thick SFS:Sn:7.5%. Further increase in SFS thickness resulted in modest improvement in x-ray interaction efficiency.
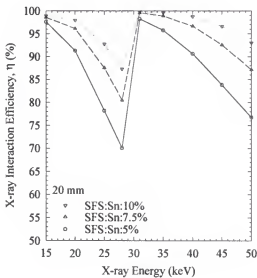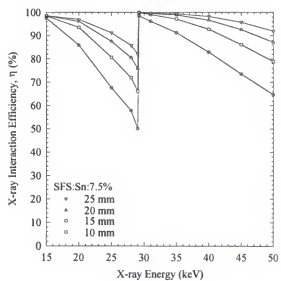
(a)   (b)

Figure 4-7. X-ray interaction efficiency for (a) tin loaded SFSs of 20 mm thickness; and (b) 7.5% by weight tin loaded SFSs of 10, 15, 20, and 25 mm thicknesses.

Figure 4-8 shows the x-ray interaction efficiency as a function of x-ray energy for the 150 μm thick CsI:Tl screen from Monte Carlo simulation (shown in dots). Figure 4-8 also shows (in line) the calculated x-ray interaction efficiency as given by the probability in percentile of an incident x-ray that interacts over the thickness, t, of the CsI:Tl screen

$$\eta = \left(1 - e^{-\frac{\mu}{\rho} \cdot \rho \cdot t}\right) \cdot 100\% \qquad (4\text{--}17)$$

The total mass attenuation coefficient (μ/ρ) data were obtained using the XCOM program developed by Berger and Hubbell (1987).
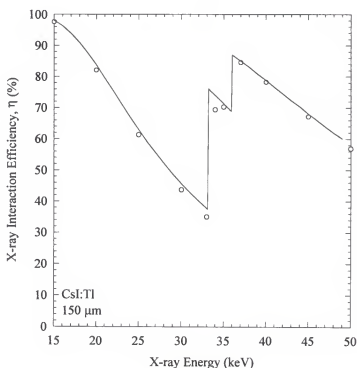
Figure 4-8. X-ray interaction efficiency of the 150 μm thick CsI:Tl screen. Results from Monte Carlo simulation were shown in dots. Results from calculation were shown in line.

For the CsI:Tl screen, the x-ray interaction efficiency was ~84% at 20 keV, and averaged ~ 20% greater than that of Min-R screen over the energy range of 15 to 30 keV. The good agreement between the results from Monte Carlo simulation and calculation using equation 4-17 demonstrates the accuracy of these Monte Carlo simulations.

4.3.2. X-ray to Light Conversion in the Scintillating Fiber Screens

Figure 4-9 shows N_{exit}, the number of light photons output from the three types of SFS per interacted x-ray photon, as a function of x-ray energy. N_{exit} is generally in the range between 30 and 50 for x-ray energies normally encountered in mammography. At x-ray energies below about 23 keV, the SFS:PS output more light photons than both high Z element loaded SFSs. This is primary due to that x-ray interactions at these energies are dominated by the photoelectric effect which gives approximately equal amount of x-ray energy deposition per interacted x-ray in all three SFSs. The scintillation light loss due to the addition of high Z element is more significant at low x-ray energies. At higher x-ray energies, the energy deposition in the high Z element loaded SFSs is higher than SFS:PS in which Compton scattering becomes important. It is also seen that, below tin K-edge (29.2 keV), there is little difference in N_{exit} for SFS:Pb:5% and SFS:Sn:10% because of their similar properties in x-ray absorption and scintillation light transmission. Due to the escape of some tin K-characteristic x-rays which do not contribute to energy deposition in the SFS:Sn:10%, N_{exit} for SFS:Sn:10% is smaller than that for SFS:Pb:5% at energies above tin K-edge. As a result of the photoelectric effect domination, Figure 4-9 also shows that N_{exit} is proportional to the incident x-ray energy for both high Z element loaded SFSs despite of the discontinuity at the tin K-edge.
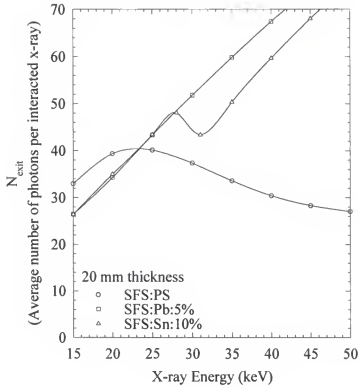
Figure 4-9. N_{exit} as a function of x-ray energy for three types of SFSs at 20 mm thickness.

Figure 4-10 shows the dependence of N_{exit} as a function of x-ray energy on the tin concentration in the SFS (Figure 4-10 (a)) and on the thickness of 7.5% by weight tin loaded SFS (Figure 4-10 (b)). N_{exit} decreases slightly with increasing tin concentration at x-ray energies used in mammography. Again, this is the result of light loss due to high Z element quenching. This effect manifests at lower x-ray energies where all SFSs have similar x-ray absorption properties. At higher x-ray energies, N_{exit} is almost independent of the concentration of tin in the SFS. N_{exit} is independent of the SFS:Sn:7.5% thickness below the tin K-edge, where x-ray interactions within the SFS are dominated by photoelectric effect. This is the result by the use of the same material in all four SFSs. At x-ray energies above the tin K-edge, a large fraction of characteristic x-rays are emitted following photoelectric absorption of primary x-rays. The probability of these energetic

(~25 to 28 keV) characteristic x-rays escaping the SFS without being absorbed is the highest for the smallest SFS volume. Therefore, N_{exit} diverges, and exhibits a higher value for the thicker SFS.
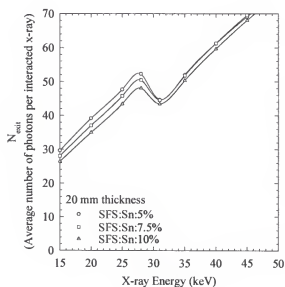
(a)
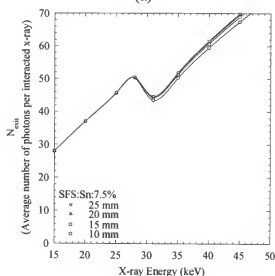
(b)

Figure 4-10. N_{exit} as a function of x-ray energy for (a) tin loaded SFSs at 20 mm thickness; and (b) 7.5% by weight tin loaded SFSs at 10, 15, 20, and 25 mm thickness.

Figure 4-11 shows N_{exit} as a function of x-ray energy for the 150 μm thick CsI:Tl screen. The number of light photons exiting the CsI:Tl screen are in the range of about 80 to 120 for x-ray energies from 20 to 30 keV. This is to be compared to that of about 30 to 50 light photons output from the plastic scintillating fiber screens. The fact that N_{exit} for CsI:Tl screen is also proportional to the incident x-ray energy indicates the photoelectric effect domination within the CsI:Tl screen. At x-ray energies above the Iodine K-edge (33.2 keV), N_{exit} drops initially due to the escape of a large fraction of Iodine characteristic x-rays, but increases with increasing x-ray energy again as the relative importance of emission of Iodine/Cesium characteristic x-rays diminishes.
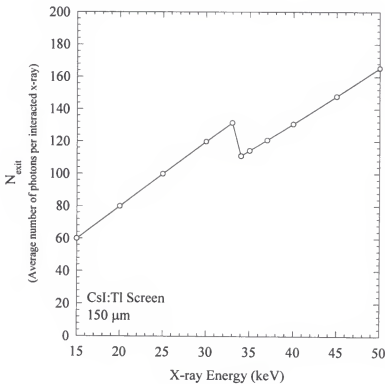
Figure 4-11. N_{exit} as a function of x-ray energy for the 150 μm thick CsI:Tl screen.

4.3.3. Quantum Accounting Diagram of the Slot X-ray Detectors

Figure 4-12(a) to (c) Shows the quantum accounting diagrams (QAD) for the three types of SFSs based slot x-ray detectors at 20, 35, and 50 keV incident x-ray energies. All the SFSs are 20 mm in thickness. At 20 keV, the number of electrons generated per incident x-ray is ~ 6 for SFS:PS, and ~ 12 for SFS:Pb:5% and SFS:Sn:10%. As shown in Figure 4-12(a), for SFS:PS, the reduction in the probability of the incident x-ray being absorbed (stage 1) leads to the reduced number of electrons generated at the CCD pixels at higher x-ray energies. For SFS:Pb:5%, as shown in Figure 4-12(b), the number of CCD electrons generated per incident x-ray increases from 20 to 35 keV due to the increased x-ray energy deposition in the SFS with increasing incident x-ray energy. Between 35 and 50 keV, however, there is little difference in the electron generation. As shown on the QAD, the less x-ray interaction efficiency (at stage 1) at 50 keV is compensated by the larger N_{exit} (at stage 2). For SFS:Sn:10%, at the three x-ray energies considered, the number of CCD electrons generated increases with increasing x-ray energy. Since there is negligible difference at stage 1 for the three x-ray energy, the difference in the amount of x-ray energy deposited in the SFS at the three x-ray energies determines the difference in electron generation. Table 4-2 summarizes the number of quanta in each stage for the slot x-ray detectors using the three types of SFSs of 20 mm thickness at 20 keV x-ray energy.

Table 4-2. Number of quanta in each stage of the slot x-ray detectors using the three types of SFSs of 20 mm thickness at 20 keV x-ray energy.

Stage	SFS:PS	SFS:Pb:5%	SFS:Sn:10%
0	1	1	1
1	0.41	1.00	0.98
2	16.27	34.14	34.29
3	14.64	30.72	30.86
4	5.86	12.29	12.34

(a)

(b)

(c)
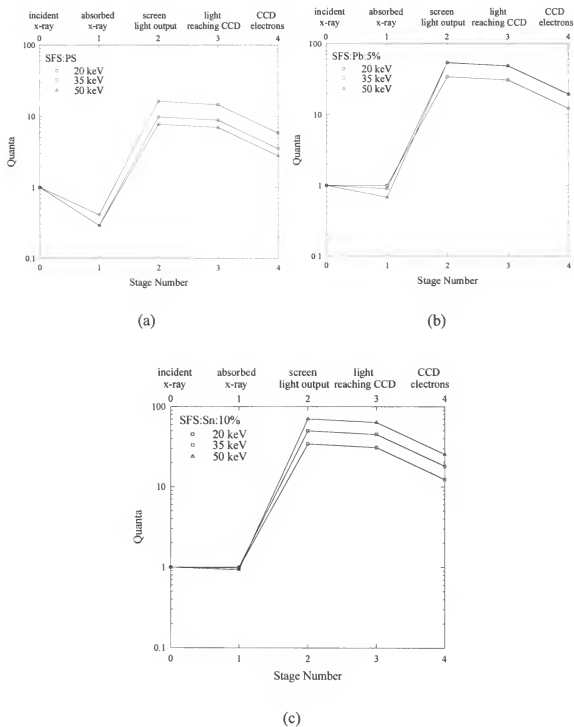
Figure 4-12. QADs for three type SFSs based slot x-ray detectors at 20, 35, and 50 keV incident x-ray energies. All the SFSs are 20 mm in thickness.

Figure 4-13 shows the QAD for the slot x-ray detector using (a) tin loaded SFSs of 20 mm thickness and (b) 7.5% by weight tin loaded SFSs of 10, 15, 20, and 25 mm thicknesses at 20 keV x-ray energy. There is a negligible difference in the number of electrons generated per incident x-ray for 20 mm thickness SFSs of varying tin concentration. The thickness of the 7.5% by weight tin loaded SFS also has a very small effect on the number of electrons produced in the CCD per incident x-ray.

(a)   (b)
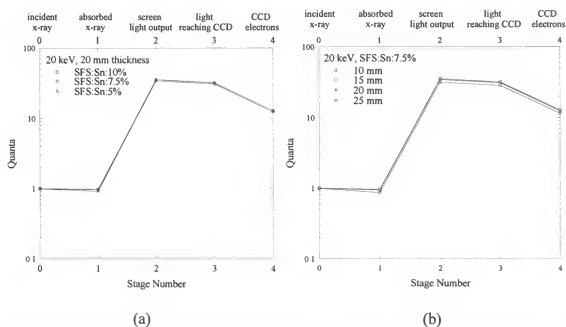
Figure 4-13. QADs for (a) 5%, 7.5%, and 10% by weight tin loaded SFSs; and (b) 7.5% by weight tin loaded SFSs of 10, 15, 20, and 25 mm thicknesses at 20 keV x-ray energy.

Figure 4-14 shows the QADs for the CsI:Tl screen based slot x-ray detector at x-ray energies from 20 to 50 keV. The number of electrons generated in the CCD per 20 keV incident x-ray is ~18, a factor of 1.5 increase compared to the slot x-ray detector using a high Z element loaded plastic scintillating screen. Although the x-ray interactions within the CsI:Tl screen are primarily photoelectric effect below Iodine K edge, the rapidly reduced x-ray interaction efficiency with increasing x-ray energy resulted in lower

number of electrons generated per incident x-ray at higher x-ray energies. At x-ray energies above Iodine K edge, the number of electrons generated is affected by the emission and absorption of Iodine or Iodine/Cesium characteristic x-rays within the CsI:Tl screen. Table 4-3 summarizes the number of quanta in each stage for the CsI:Tl screen based slot x-ray detector.
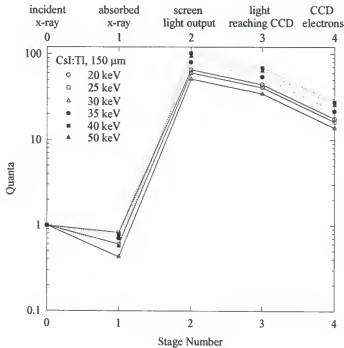
Figure 4-14. QADs for the CsI:Tl screen at 20, 25, 30, 35, 40, and 50 keV.

Table 4-3. Number of Quanta in each stage of the CsI:Tl screen based slot x-ray detector.

Stage	X-ray Energy					
	20	25	30	35	40	50
0	1	1	1	1	1	1
1	0.82	0.60	0.43	0.70	0.78	0.57
2	65.53	60.25	51.09	80.29	102.25	94.12
3	44.24	40.67	34.49	54.20	69.02	63.53
4	17.69	16.27	13.79	21.68	27.61	25.41

4.3.4. Measurement of Signal Intensity in the Slot X-ray Detectors

Signal intensity was measured for a CsI:Tl screen based scanning slot x-ray detector, and was compared to the same slot x-ray detector using a 31.7 mg/cm^2 Gd$_2$O$_2$S:Tb phosphor (Kodak Min-R screen phosphor).

For CsI:Tl screen, the fraction of the incident x-ray energy which converted to light energy depends on the x-ray interaction efficiency and the x-ray energy conversion efficiency (12%). Measured signal intensity as recorded by the CCD will also need to take into account light transmission efficiency of the scintillation screen, the coupling efficiency of the image guide and the quantum efficiency of the CCD. The CCDs used have similar efficiency in converting the scintillation light from both the CsI:Tl screen and Gd$_2$O$_2$S:Tb phosphor. The conversion efficiency of Gd$_2$O$_2$S:Tb is 15%. Assuming a similar light absorption for the two screen materials, the slot x-ray detector using the CsI:Tl screen would result in a signal intensity (CCD pixel value) approximately equal to that of the same slot x-ray detector using the Min-R screen phosphor.

Measured signal intensities were obtained for slot x-ray detectors exposed to a uniform x-ray source generated at tube potentials ranging from 24 to 34 kV using the GE Senograph 500 T mammography x-ray unit. Measured signal intensities (S_{CsI}) were obtained from the slot x-ray detectors using the CsI:Tl screen. Using the same exposure technique, signal intensities (S_{Min-R}) were also measured for the slot x-ray detectors by replacing the CsI:Tl screen with a Min-R screen phosphor. The ratio of these two intensities (i.e. S_{CsI}/S_{Min-R}) were then determined. A constant phantom scanning speed of 1 cm/second was used for all signal intensity measurements.

Figure 4-15 shows the measured S_{CsI}/S_{Min-R} ratios as a function of x-ray tube potential. This ratio is ~0.9 and is independent of x-ray tube potential. This value is close to the theoretical value of 1.0 and indicates that the two phosphors appear to have similar light transmission and absorption properties in the detector arrangement depicted in

Figure 4-2. These results show that the use of a CsI:Tl screen in a slot x-ray detector produces comparable signals to the Gd_2O_2S:Tb phosphor based slot x-ray detector.
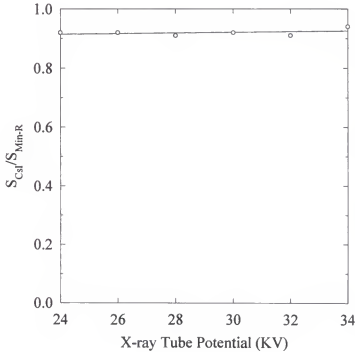
Figure 4-15. Measured S_{CsI}/S_{Min-R} ratios as a function of x-ray tube potential using a Mo anode x-ray tube.

4.4. Modulation Transfer Function of the Slot X-ray Detectors

4.4.1. Energy Deposition Line Spread Function

Figure 4-16 (a), (b), and (c) show the calculated LSF_E curves for the three type of plastic scintillating fiber screens of 20 mm thickness at 20, 35, and 50 keV incident x-ray energies. The major difference in the LSF_E curves of the three type SFSs is shown in the tails of these curves.
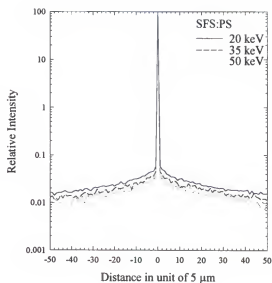
(a)
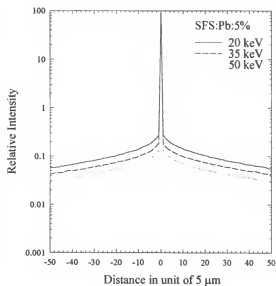
(b)
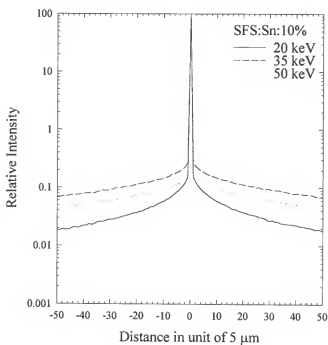
(c)

Figure 4-16. Energy deposition LSF, LSF$_E$, of the three types of SFSs of 20 mm thickness at 20, 35, and 50 keV incident x-ray energies.

LSF_E of the SFS:PS shows little dependence on the incident x-ray energy, and has the smallest spread among the three SFSs. The reason is that scattered x-rays carry most of the incident x-ray energy and has the highest probability to escape in the SFS:PS. For SFS:Pb:5%, the tail in its LSF_E curve becomes smaller as the x-ray energy increases. This is mainly due to the increased energy transfer to the photoelectrons which deposit their energies at the primary interaction site. LSF_E of SFS:Sn at 20 keV is better than the LSF_E of SFS:Pb:5% at all incident x-ray energies. However, the reabsorption of tin K x-rays causes large degradation in the resultant LSF_E at 35 keV x-ray energy. Similar to the SFS:Pb:5%, the tail in the LSF_E of the SFS:Sn at 50 keV is smaller than at 35 keV.

Figure 4-17 shows the LSF_E curves for (a) 5%, %, 7.5%, and 10% by weight tin loaded SFSs of 20 mm thickness and (b) 7.5% by weight tin loaded SFSs of 10, 15, 20, and 25 mm thicknesses at 20 keV x-ray energy. In both cases, LSF_E curves show a negligible change by varying the tin concentration or the thickness of the SFSs.

(a)   (b)
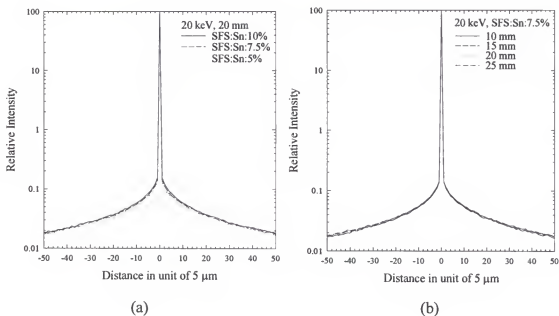
Figure 4-17. LSF_E curves plotted for (a) 5%, 7.5%, and 10% by weight tin loaded SFSs of 20 mm thickness; and (b) 7.5% by weight tin loaded SFSs of 10, 15, 20, and 25 mm thicknesses at 20 keV x-ray energy.

Figure 4-18 shows the LSF$_E$ curves for the 150 μm thick CsI:Tl screen at 20, 35, and 50 keV incident x-ray energies. At 20 keV, there is very little spatial spread of incident x-ray energy as the majority of incident x-rays are absorbed locally through photoelectric absorption. At 35 keV, Iodine K-characteristic x-rays are emitted following a photoelectric absorption of incident x-ray. The fluorescence yield for Iodine K-characteristic x-rays emission is ~ 88% with energies of 28.6, 28.3, and 32.3 keV for K$_{\alpha1}$, K$_{\alpha2}$, and K$_{\beta1}$. These large fraction of energetic secondary x-rays are emitted isotropically, and can interact again within the CsI:Tl at a remote location from the primary x-ray interaction site. This leads to a large spatial spread of the deposited x-ray energy from the primary interaction site. At 50 keV, this spatial spread of x-ray energy deposition is reduced as a result of increased amount of x-ray energy deposited at the primary interaction sites by energetic photoelectrons.
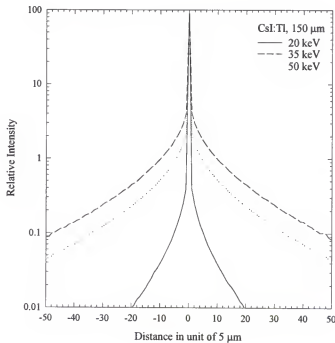
Figure 4-18. LSF$_E$ curves for the 150 μm thick CsI:Tl screen at 20, 35, and 50 keV incident x-ray energies.

4.4.2. Scintillation Screen MTF

Figure 4-19 shows the $MTF_O(f)$ curves for plastic scintillating fiber screens made of scintillating fibers of 20, 30, and 40 μm diameters. For d = 20 μm, $MTF_O(f)$ values are 0.98, 0.93, 0.85 and 0.75 at 5, 10, 15 and 20 lp/mm, respectively.
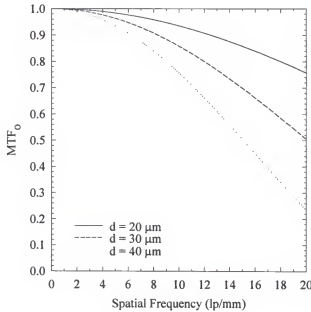
Figure 4-19. $MTF_O(f)$ curves for SFS with individual fiber diameters of 20, 30, and 40μm.

Figure 4-20 shows the calculated CsI:Tl screen MTF, $MTF_{CsI}(f)$, and the calculated $MTF_E(f)$ from Monte Carlo Simulation using a 40 kV x-ray spectrum. The $MTF_{CsI}(f)$ is obtained from the measured contrast transfer function ($CTF(f)$) using equation 4-16. Figure 4-20 also shows the calculated CsI:Tl screen optical MTF using Equation 4-13. For the 40 kV x-ray spectrum, the energy of only about 7% of the total incident x-rays is greater than the Iodine K edge. The effect of K-characteristic x-ray emission is therefore small for the 40 KV x-ray source. The CsI:Tl screen MTF is dominated by the scintillation light diffusion within the screen.
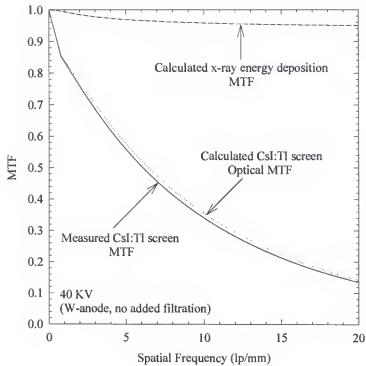
Figure 4-20. MTF$_E$(f), MTF$_O$(f), and MTF$_{CsI}$(f) of the 150 μm thick CsI:Tl screen using a 40 kV x-ray spectrum.

Figure 4-21 (a), (b), and (c) show the MTF of the plastic scintillating fiber screen, MTF$_{SFS}$(f), curves at 20, 35 and 50 keV incident x-ray energies for the three types of SFSs of 20 mm thickness and made of 20 μm diameter plastic scintillating fibers. For each SFS, MTF$_{SFS}$(f) drops quickly in the range from 0 to 2 lp/mm due to the spread of x-ray energy deposition from the primary interaction site. MTF$_{SFS}$(f) for SFS:Pb:5% improves with increasing x-ray energy. For SFS:Sn:10%, the emission and absorption of tin K-characteristic x-rays significantly reduce the screen MTF. Nevertheless, the MTF$_{SFS}$(f) values of all SFSs remain high (> 50%) beyond 25 lp/mm and are dominated by the 20 μm scintillating fiber diameter used. Table 4-4 summarizes the MTF$_{SFS}$(f) values of the three SFSs at 5, 10, 15 and 20 lp/mm spatial frequencies at 20 keV x-ray energy.
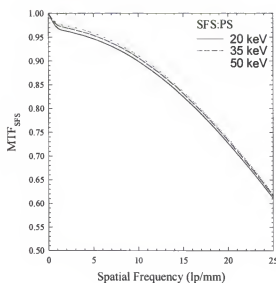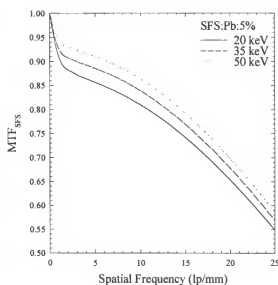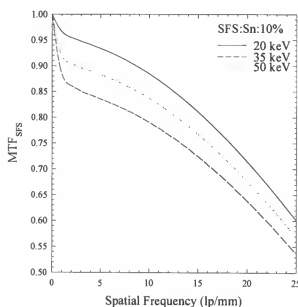
Figure 4-21. MTF$_{SFS}$(f) curves of the three types of SFSs of 20 mm thickness and made of individual scintillating fibers of 20 μm diameter at 20, 35, and 50 keV incident x-ray energies.

Table 4-4. MTF$_{SFS}$(f) values for three types of SFSs at 20 keV incident x-ray energy

f (lp/mm)	MTF$_{SFS}$(f)		
	SFS:PS	SFS:Pb:5%	SFS:Sn:10%
5	0.94	0.85	0.93
10	0.90	0.81	0.89
15	0.82	0.74	0.81
20	0.73	0.65	0.72

It was also found that MTF$_{SFS}$(f) curves show negligible dependence on the concentration of tin from 5% to 10% by weight in the SFSs. The effect of the SFS thickness on MTF$_{SFS}$(f) is also very small.

Figure 4-22 shows the dependence of MTF$_{SFS}$(f) curves on the scintillating fiber diameter for a 20 mm thick, 7.5% by weight tin loaded SFS at 20 and 35 keV incident x-ray energies. At 20 keV, MTF$_{SFS}$(f) is dominated by the effect of the plastic scintillating fiber diameter. At 35 keV, MTF$_{SFS}$(f) drops significantly as tin K-characteristic x-rays are emitted and absorbed within the SFS.

Figure 4-23 shows the 150 μm thick CsI:Tl screen MTF, MTF$_{CsI}$(f), at incident x-ray energies from 20 to 50 keV. Below Iodine K-edge, x-ray interactions within the CsI:Tl screen are dominated by photoelectric effect. MTF$_{CsI}$(f), the total CsI:Tl screen MTF, is determined by the scintillation light spread (MTF$_O$(f)) within the CsI:Tl screen. There is little difference in MTF$_{CsI}$(f) values between 20 and 30 keV. At 35 keV, the reabsorption of Iodine K-characteristic x-rays within the CsI:Tl screen lead to a large spread of deposited x-ray energy. Compared to 20 keV, MTF values at 35 keV decreased about 15%, 30%, and 35% at spatial frequency of 2, 5, and 10 lp/mm, respectively. Above 35 keV, MTF$_{CsI}$(f) improves with increasing x-ray energy.
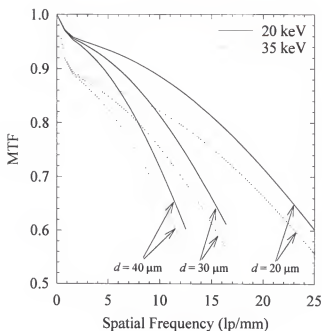
Figure 4-22. MTF$_{SFS}$(f) curves at 20 and 35 keV for the 20 mm thick, 7.5% by weight tin loaded SFSs made of 20, 30, and 40 μm diameter plastic scintillating fibers.
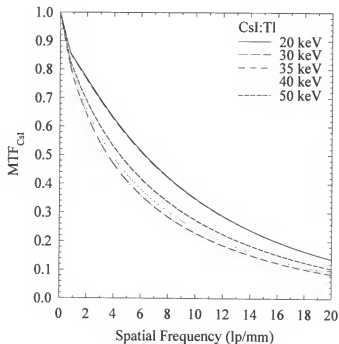
Figure 4-23. MTF(f)of the 150 μm thick CsI:Tl screen at incident x-ray energies from 20 to 50 keV.

4.4.3. MTF of the Slot X-ray Detectors

Figure 4-24 shows the MTF of the slot x-ray detector using the 20 mm thick SFS:PS, SFS:Pb:5%, and SFS:Sn:7.5% at 20 and 35 keV x-ray energies. All SFSs are made of 20 μm diameter plastic scintillating fibers. Also shown in Figure 4-24 is the MTF(f) curve of the CCD with pixel size of 24 μm.

(a)   (b)
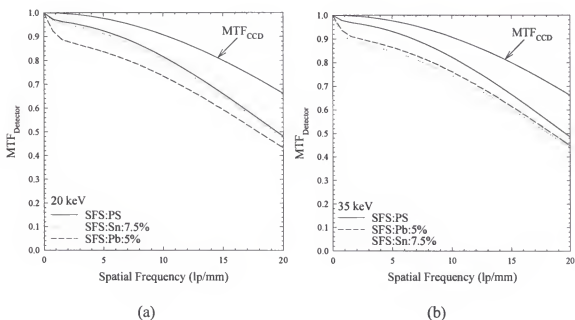
Figure 4-24. MTF curves of the slot x-ray detector using 20 mm thick SFS:PS, SFS:Pb:5%, and SFS:Sn:7.5% at (a) 20, and (b) 35 keV x-ray energies. All SFSs are made of 20 μm diameter plastic scintillating fibers.

For SFS:PS based slot x-ray detector, MTF$_{Detector}$(f) is dominated by the SFS:PS screen MTF at spatial frequency less than 4 lp/mm. Beyond 5 lp/mm, MTF$_{Detector}$(f) is governed by both the SFS:PS screen MTF and CCD MTF. MTF$_{Detector}$(f) values for SFS:Pb:5% and SFS:Sn:7.5% based slot x-ray detectors exhibit the similar properties as mentioned for SFS:PS. MTF$_{Detector}$(f) for SFS:PS based slot x-ray detector is superior to slot x-ray detectors using a high Z element loaded SFS. At 20 keV, MTF$_{Detector}$(f) for SFS:Sn:7.5% based slot x-ray detector approaches that of SFS:PS based slot x-ray

detector, and is significantly higher than that of SFS:Pb:5% based slot x-ray detector. At 35 keV, $MTF_{Detector}(f)$ for SFS:Sn:7.5% based slot x-ray detector is below that of SFS:Pb:5% based slot x-ray detector.

Figure 4-25 shows the MTF curves of the slot x-ray detector using the 150 μm thick CsI:Tl screen at 20, 35, and 50 keV x-ray energies. At all x-ray energies, $MTF_{Detector}(f)$ is dominated by the CsI:Tl screen MTF. At 20 keV, $MTF_{Detector}(f)$ values are 0.76, 0.56, 0.32, and 0.17 at 2, 5, 10, and 15 lp/mm.
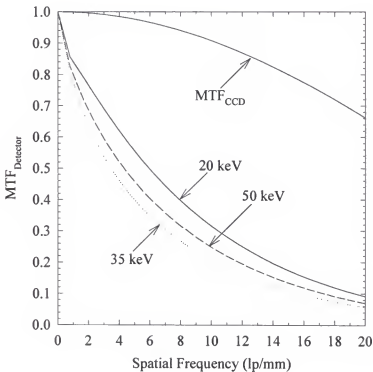
Figure 4-25. MTF(f) of the slot x-ray detector using the 150 μm thick CsI:Tl screen at 20, 35, and 50 keV x-ray energies

Figure 4-26 shows the MTF(f) curves of all the stages for the CsI:Tl screen based slot x-ray detector using a 30 kV mammographic x-ray spectrum. The differences in the

values between MTF$_{Detector}$(f) for the 30 kV spectrum and for 20 keV monoenergetic x-ray source are less than 1% at all spatial frequencies.
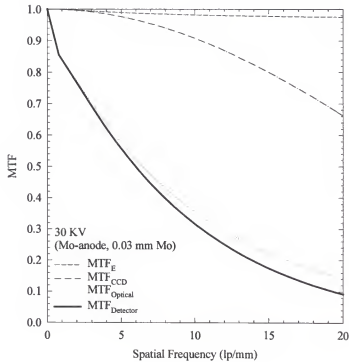
Figure 4-26. MTF(f) curves of all the conversion stages for the CsI:Tl screen based slot x-ray detector using a 30 kV mammographic x-ray spectrum.

In a plastic scintillating fiber screen based slot x-ray detector investigated in this study, the plastic scintillating fiber diameter (20 μm) is comparable to the CCD pixel size (24 μm). Depending on the relative alignment between each plastic scintillating fiber and the CCD pixel(s), shifting an object parallel to the image plane will not produce the same image. The relative position between each individual plastic scintillating fiber and CCD pixel(s) has a very large effect on the final slot x-ray detector MTF. A range of MTF$_{Detector}$(f)s exists for a plastic scintillating fiber screen based slot x-ray detector.

Figure 4-27 shows the effect of pixel alignment on the $MTF_{Detector}(f)$ values at 20 keV for a slot x-ray detector using a 7.5% by weight tin loaded SFS made of 20 μm plastic scintillating fibers. Compared to the perfect alignment in which one plastic scintillating fiber is covered by a single CCD pixel, $MTF_{Detector}(f)$ when one plastic scintillating fiber is distributed over four CCD pixels (worst alignment) decreased about 2%, 10%, 35%, and 70% at spatial frequencies of 2, 5, 10, and 15 lp/mm, respectively.
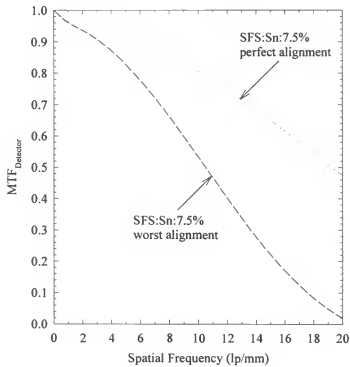
Figure 4-27. Effect of pixel alignment on $MTF_{Detector}(f)$ curves at 20 keV incident x-ray energy for a slot x-ray detector using a 20 mm thick, 7.5% by weight tin loaded SFS made of 20 μm diameter plastic scintillating fibers.

4.4.4. Measurement of Spatial Resolution in the Slot X-ray Detectors

Spatial resolution performance of the CsI:Tl screen based slot x-ray detector was investigated by taking the images of a $1°$ star resolution test pattern (Nuclear Associates,

Model No. 07-542). Phantom movement speed was varied from 1 to 4 cm/second to study its effect on image spatial resolution. Figure 4-28 shows an x-ray image of the center of the 1° star resolution test pattern which was obtained using a 4 cm/second scanning speed and a tube potential of 32 kV with exposure to detector level of ~10 mR.
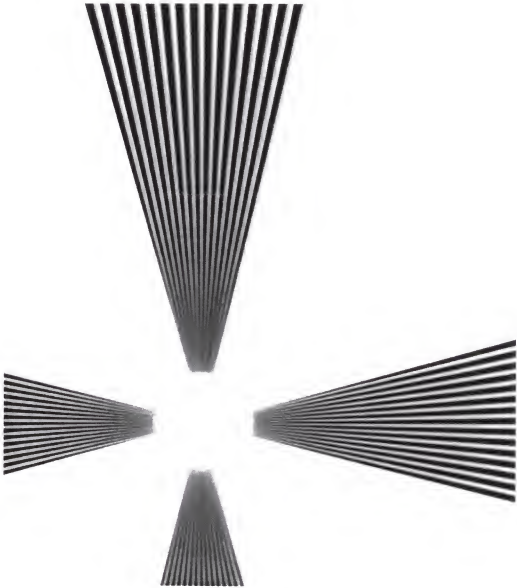
Figure 4-28. An x-ray image of a 1° star resolution test pattern acquired from a prototype CsI:Tl screen based slot x-ray detector using a 32 kV x-ray spectrum.

The limiting spatial resolution, f_{max}, of the CsI:Tl screen based slot x-ray detector can be determined by measuring the blur diameter, D (mm), in the star image. f_{max} is related to D by

$$f_{max} = 1.273 \frac{45}{D} \tag{4-18}$$

D is measured to be 3.96 mm (165 pixels) for the image shown in Figure 4-28. The resulted f_{max} is 14.47 lp/mm. Table 4-5 summarizes the measured f_{max} at scanning speeds from 1 to 4 cm/second. f_{max} was also found to be independent of the phantom movement speed for the CsI:Tl screen based slot x-ray detector.

Table 4-5. Limiting spatial resolution, f_{max}, as a function of scanning speed for the CsI:Tl screen based slot x-ray detector.

Scanning speed (cm/second)	Blur Diameter (pixels)	Blur Diameter (mm)	f_{max} (lp/mm)
1	153	3.672	15.60
2	160	3.84	14.92
3	163	3.912	14.65
4	165	3.96	14.47

From a MTF curve, f_{max} is generally given by the spatial frequency where the MTF value is between 5 to 10%. A 5 to 10% MTF value (contrast) is a threshold for a signal to be detected by a reader with additive noise level. MTF analysis, however, does not count the noise in the x-ray detector. The predicted f_{max} is therefore about 19 lp/mm for a 10% MTF threshold the $MTF_{Detector}(f)$ curve of the CsI:Tl screen based slot x-ray detector shown in Figure 4-26.

The measured limiting spatial resolution of the CsI:Tl screen based slot x-ray detector is about 15 lp/mm which appears to be lower than that of about 19 lp/mm

predicted. The reason for this is that, measurement of spatial resolution is affected by several factors which were not taken into account in the theoretical analysis. Theses factors include (1) noise in the images which affect the observer's ability to identify the signals in the noisy background; (2) the alignment between CCD pixel column and phantom scanning direction which is practically impossible to be aligned perfectly. A single point in the phantom can therefore be spread into several CCD pixel column during the scanning process; (3) the charge transfer efficiency of the CCD pixel is not 100%. This will always leave a small amount of CCD pixel charge behind the actual image pixel, and cause a spatial spread of image signal. The measured 15 lp/mm limiting spatial resolution is therefore consistent with the theoretical analysis in this study.

To compare the spatial resolution performance of the slot x-ray detectors using the CsI:Tl screen and the Gd_2O_2S:Tb phosphor screen, the above measurement of limiting spatial resolution was performed on the same slot x-ray detector by replacing the CsI:Tl screen with a 31.7 mg/cm^2 Gd_2O_2S:Tb Phosphor (Kodak Min-R screen phosphor). Table 4-6 summarizes the measured f_{max} at scanning speeds from 1 to 4 cm/second for this Gd_2O_2S:Tb phosphor screen based slot x-ray detector. At scanning speed above 2 cm/second, f_{max} is largely affected by the afterglow effect of Gd_2O_2S:Tb Phosphor.

Table 4-6. Limiting spatial resolution, f_{max}, as a function of scanning speed for the Gd_2O_2S:Tb phosphor screen based slot x-ray detector.

Scanning speed (cm/second)	Blur Diameter (pixels)	Blur Diameter (mm)	f_{max} (lp/mm)
1	170	4.08	14.04
2	175	4.2	13.64
3	249	5.976	9.59
4	371	8.904	6.43

4.4.5. Measurement of a Prototype Scintillating Fiber Screen Spatial Resolution

Figure 4-29 shows a prototype imaging system which was constructed to investigated the spatial resolution performance of a SFS made of Polystyrene/PMMA core/cladding scintillating fibers. The SFS was 1 cm x 1cm x 1 cm thick, and was made of fibers of 30 μm in diameter. There was no EMA added in the scintillating fiber. The SFS was coupled to a tapered glass microfiber image guide which was connected to an image intensifier. The intensified image was then read out by a room temperature operated CCD TV camera for subsequent analysis. Tapered glass image guide has a demagnification ratio of 1.5:1. CCD pixel size was 20 μm which converted to 43.6 μm at the scintillating fiber screen plane. The limiting spatial resolution of the image intensifier was 75 lp/mm.
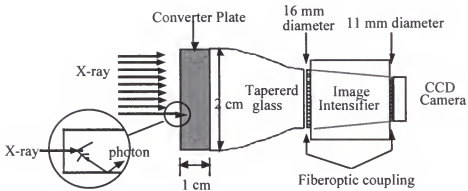
Figure 4-29. A prototype digital x-ray imaging detector using a plastic scintillating fiber screen.

Figure 4-30 shows an x-ray image of a 2° star resolution test phantom which was imaged with this prototype system. The test image was obtained by setting the phantom in direct contact with the SFS. The x-ray tube has a Tungsten (W) anode and the tube potential used was 70 kVp (2 mm Al filtration). A limiting spatial resolution of about 11.3 lp/mm was confirmed by counting the number of line pairs per mm in the image.

This showed that the prototype x-ray imaging detector limiting spatial resolution was mainly determined by the pixel size of the CCD whose resolution was reduced to 11.5 lp/mm when transforming back to the scintillating fiber screen plane. It implied that the limiting spatial resolution of the SFS alone is significantly higher than 11 lp/mm. This is in agreement with a 16.7 lp/mm limiting spatial resolution as can be expected from the 30 μm scintillating fiber diameter. However, the contrast of the lead bar pattern in the image is low. One of the reason is that scintillation light can transmitted through many fibers to the SFS output as a result of no EMA addition in the SFS. This resulted in a loss of image signal.
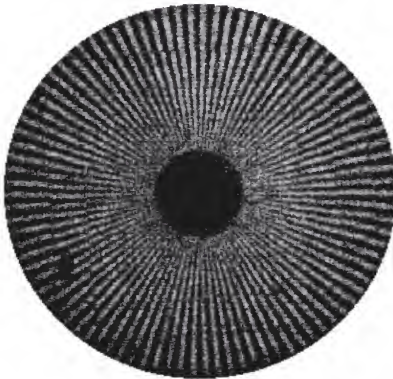
Figure 4-30. An x-ray image of a $2°$ star resolution test phantom obtained using the prototype SFS based digital x-ray imaging detector.

More importantly, this study demonstrated the limitation of low energy conversion efficiency and scintillation light collection efficiency of a SFS. It was observed that the star image appears to be very noisy. There are several factors contributing to this noisy appearance. First, the input photocathode of the image intensifier converts scintillation light into electrons. However, the scintillation light spectrum of the scintillating fibers peaked at ~530 nm, where the image intensifier photocathode has very low quantum efficiency. Second, and most importantly, the plastic scintillating fibers had an energy conversion efficiency of ~3% and a scintillation light collection efficiency of ~3%. These fibers are standard products of current scintillating fiber technology. These low energy conversion efficiency and light collection efficiency lead to the low image signal level. Also, the CCD camera used was a commercial TV camera. The thermal noise and readout noise of the CCD camera were high. As a result, the image signal to noise ratio is low, which explains why the star image appears to be very noisy.

CHAPTER 5
NOISE PROPAGATION IN THE SLOT X-RAY DETECTORS

5.1. Detective Quantum Efficiency and Noise Propagation Theory

5.1.1. Detective Quantum Efficiency (DQE)

Noise propagation in the x-ray imaging detectors, especially radiographic and fluoroscopic phosphor screens, has been investigated for many years. It is recognized that detective quantum efficiency, DQE(f) (where f is spatial frequency), can be used to characterize the overall noise performance of an x-ray imaging detector (Cunningham et al., 1994; Dainty and Shaw, 1974; Swank, 1973; Tapiovaara and Wagner, 1984). DQE(f) describes the efficiency in transferring the signal-to-noise ratio (squared) contained in the incident x-ray pattern to the detector output, as given by

$$DQE(f) = \frac{SNR_o^2(f)}{SNR_i^2(f)} \tag{5-1}$$

where, $SNR_i(f)$ and $SNR_o(f)$ are the input and output signal-to-noise ratio (SNR) of the image in the spatial frequency domain. For an ideal detector, DQE(f) is unity at all spatial frequencies. Additional noise sources in a real detector reduces the DQE(f) and often cause the DQE(f) to decrease with increasing spatial frequency. For monoenergetic incident x-ray energy, Swank (1973) has shown that the zero spatial frequency detective quantum efficiency, DQE(0), of a scintillation screen is given by

$$DQE(0) = \eta \cdot A_S \tag{5-2}$$

122

where A_S is the Swank factor (also called Swank statistical or noise factor).

X-ray conversion in the scintillation screen is a process of primary importance for an x-ray imaging detector. X-ray absorption and the following emission of scintillation light from the scintillation screen directly determine both the signal intensity and the magnitude of signal fluctuations referred to as noise. In the scanning slot x-ray detectors investigated, the output signals are the integration of generated visible photons. The signal intensity in general is distributed according to some probability distributions. These variations cause variations in the magnitude of light burst from each x-ray interaction in the scintillation screen, and leads to an uncertainty (noise) in recording the total number of x-rays incident on the detector.

There are three major factors affecting this scintillation light intensity distribution: (1) the incident x-ray energy distribution. (2) the absorbed energy distribution which results from different absorption process (Metz and Vyborny, 1983, Swank, 1973), and (3) the optical pulse distribution which results from unequal light propagation depending on the position of x-ray-to-light conversion (Drangova and Rowlands, 1986; Nishikawa and Yaffe, 1989, 1990a, 1990b). The last two distributions are unique properties of the scintillation screen, and their effects on the image noise is characterized by A_S. A_S values range from 0.6 to 0.8 for most phosphor screens used in screen-film mammography.

Calculations and measurements of A_S can be performed from the scintillation light output intensity distribution when x-rays of monoenergetic energy incident on the scintillation screen (Chan and Doi, 1984; Dick and Motz, 1981; Fahrig et al., 1995; Ginzburg and Motz, 1993; Swank 1974). A_S is defined in terms of the moments, m_0, m_1, m_2, of the scintillation light output intensity distribution, $P(N_{exit})$, and is given by

$$A_S = \frac{m_1^2}{m_0 m_2} \tag{5-3}$$

where the *i*th moment of $P(N_{exit})$ is defined as

$$m_i = \sum_0^{N_{max}} P(N_{exit}) N_{exit}^i \qquad (5\text{-}4)$$

For a plastic scintillating fiber screen (SFS), emitted scintillation light is collected and transmitted to the SFS output due to the total reflection principle. The number of light photons exiting the SFS, N_{exit}, is proportional to the total number, N, of light photons emitted per absorbed x-ray, and is independent on the depth of x-ray interaction within the SFS. In this study, the emitted light intensity distribution, $P(N)$, was therefore used to obtain the Swank factor for the SFS.

Scintillation light intensity distributions are computed for the scintillation screens (plastic scintillating fiber screens and the CsI:Tl screen) using Monte Carlo simulation. In all simulations, monoenergetic x-rays from a point source were normally incident on the scintillation screen. Three x-ray interaction processes with the scintillation screens were included: Compton scattering, coherent scattering, and photoelectric effect. The Compton recoil electrons, photoelectrons and Auger electrons were assumed to deposit their energies in the x-ray interaction sites.

For a plastic scintillating fiber screen, total x-ray energy deposited, E_d, from each interacted incident x-ray was generated. E_d varies due to the variation in the x-ray absorption processes. For each E_d, the average number of light photons emitted, $\overline{N}$, is given by

$$\overline{N} = \varepsilon \cdot (1 - L) \cdot (1 - q) \cdot \frac{E_d}{2.34} \qquad (5\text{-}5)$$

The conversion from E_d to the number of light photons emitted is also a random process which is described by a Poison distribution with mean equal to $\overline{N}$. In the simulation, for each $\overline{N}$ computed using equation 5-5, a value for N was generated using the rejection sampling method described by Williamson (1988).

For the CsI:Tl screen, a similar method was used to generate the output scintillation light intensity distribution, $P(N_{exit})$. The average of N_{exit} is obtained from

$$\overline{N}_{exit} = E_d \cdot \overline{K} \tag{5-6}$$

where $\overline{K} = 4$, described in Chapter 4, is the average number of light photons output from the 150 μm thick CsI:Tl screen per keV of x-ray energy deposition.

5.1.2. Noise Propagation in The Multi-Stage Imaging System

To analyze noise performance of the slot x-ray detectors, the theory of noise propagation in a cascaded imaging system is applied. In this approach, an imaging system is divided into cascaded stages in which noise propagates from one to another (Cunningham et al., 1994; Dillon et al., 1985; Rabbani et al., 1987; Rabbani and Van Metter, 1989; Zwieg, 1965).

Figure 5-1 shows the relationship between the input and output signal and noise in each stage of a M stage imaging system. For each stage (i), signal, $\Phi_i(x)$, is described by the distribution of image quanta. $\Phi_i(x)$ is a one dimension representation of the two orthogonal dimension distribution. Noise, $W_i(f)$, is described by the noise power spectrum (NPS). The SNR in each stage of the system is then given by

$$SNR_i^2(f) = \frac{\overline{\Phi}_i^2}{W_i(f)} \tag{5-7}$$
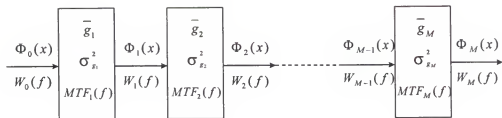
Figure 5-1. Signal and noise propagation in a M stage imaging system.

For a stage with gain only, the process is characterized by an average gain, $\bar{g}_i$, and the variance in the gain, $\sigma^2_{g_i}$. The modulation transfer function, $MTF_i(f)$, of a gain only stage is unity. The output and input signal and noise are related as

$$\overline{\Phi}_i = \bar{g}_i \overline{\Phi}_{i-1} \qquad W_i(f) = \bar{g}_i^2 W_{i-1}(f) + \sigma^2_{g_i} \overline{\Phi}_{i-1} \qquad (5\text{-}8)$$

where $\overline{\Phi}_i$ is the mean number of quanta per unit area. For an ideal stage ($\sigma^2_{g_i} = 0$), the signal and noise are equally amplified and the SNR will not be affected by an ideal stage.

For a stage with spatial spreading only, the process is characterized by its modulation transfer function, $MTF_i(f)$. Consequently, we have $\bar{g}_i = 1$ and $\sigma^2_{g_i} = 0$. The output and input signal and noise are related as

$$\overline{\Phi}_i = \overline{\Phi}_{i-1} \qquad W_i(f) = [W_{i-1}(f) - \overline{\Phi}_{i-1}] MTF_i^2(f) + \overline{\Phi}_{i-1} \qquad (5\text{-}9)$$

In an x-ray imaging system, many physical processes always involve both a gain and a spatial spreading. For example, the conversion of x-ray to light photons in a scintillation screen includes a gain process in which one x-ray is converted into many light photons, and a spatial spreading process in which the light photons diffused to the screen output. To apply the noise propagation theory, this physical stage is divided into two cascaded stages: a gain only stage which accounts for both the conversion (from x-ray to light photons) gain and attenuation loss of light photons during the diffusion to the

screen output; a spatial spreading only stage which only accounts for the spatial spreading. For example, if one x-ray is converted into 2000 light photons in the screen. These 2000 light photons are partially absorbed in the screen on their way to the screen output, and only 1500 light photons exit the screen. The gain for the gain only stage will be assigned a value of 1500.

Equation 5-9 indicates that for a spatial spreading stage, the correlated component of noise is modulated by the square of the MTF of the stage, whereas the uncorrelated noise component is not changed. In a stage where independent noise sources (such as screen structure noise, electronic noise, etc.) exist, equation 5-8 and 5-9 are modified by adding the NPS of the additive noise, $W_{a_i}(f)$, to the output NPS.

The spatial frequency dependent DQE, DQE(f), of a M stage system is generally given by

$$DQE(f) = \frac{SNR_M^2(f)}{SNR_0^2(f)} = \frac{\overline{\Phi}_M^2 \Big/ W_M(f)}{\overline{\Phi}_0^2 \Big/ W_0(f)} = \frac{\prod_{i=1}^{M} \overline{g}_i^2 MTF_i^2(f)\overline{\Phi}_0^2 \Big/ W_M(f)}{\overline{\Phi}_0^2 \Big/ W_0(f)} \qquad (5\text{-}10)$$

When the input of a M cascaded stage system has a Poisson distribution (as is always true for an x-ray imaging system), we have $W_0(f) = \Phi_0$. Combining this and equations 5-8 or 5-9, it can be found that DQE(f) of a M stage system is given by

$$DQE(f) = \frac{1}{1 + \sum_{i=1}^{M} \left(\dfrac{1 + \varepsilon_{g_i} MTF_i^2(f) + W_{a_i}(f)\Big/\overline{\Phi}_i}{\prod_{j=1}^{i} \overline{g}_j MTF_j^2(f)} \right)} \qquad (5\text{-}11)$$

where the Poisson excess term, ε_{g_i} is used to describe the relative amount of variance in the distribution of g_i that exceeds that of a Poisson distribution. ε_{g_i} is given by

$$\varepsilon_{g_i} = \frac{\sigma_{g_i}^2}{g_i} - 1 \qquad (5\text{-}12)$$

5.2. Noise in Cascaded Slot X-ray Detectors

5.2.1. Incident X-ray Fluence

Diagrams of the slot x-ray detectors are shown in Figure 4-1 and 4-2. In this study, the slot x-ray detectors are described as cascaded conversion stages according to the noise propagation theory. A total of six conversion stages were identified: (1) Interactions of x-rays within the screen; (2) Spatial spreading of x-ray energy within the screen; (3) Conversion of x-ray to light; (4) Spatial spreading of light to screen output; (5) Coupling of screen light to CCD; (6) Conversion of light to CCD electrons. In this section, the parameters (g, ε_g, and MTF(f)) governing the signal and noise propagation properties of the slot x-ray detector are discussed for each stage. A generalized equation is then derived for the DQE(f) of the slot x-ray detector.

Monoenergetic x-rays from 15 to 50 keV are considered. For a given incident x-ray energy E (in units of keV), the mean fluence, $\overline{\Phi}_0$, per unit x-ray exposure, X (in units of mR), is calculated as

$$\frac{\overline{\Phi}_0}{X} = \frac{5.45 \cdot 10^5}{E \cdot [\mu_{ab}(E)/\rho]_{air}} \quad \text{(units: x-rays/mm}^2\text{/mR)} \qquad (5\text{-}13)$$

where $[\mu_{ab}(E)/\rho]_{air}$ is the energy absorption coefficient (cm^2/g) for air. Because the incident x-ray fluence Φ_0 is Poisson distributed, we have $W_0(f) = \overline{\Phi}_0$.

<u>5.2.2. Screen Model</u>

A cascaded scintillation screen model is composed of three distinctive processes. These are x-ray interaction, x-ray to light photon conversion, and light photon propagation to the screen output.

X-ray interaction in the scintillation screen is again a process which has both a gain and a spatial spreading. To apply equation 5-11, this process is divided into two cascaded stages. The probability of a incident x-ray interacted in the scintillation screen is determined by the screen x-ray interaction efficiency η. This is a binary selection process, and can be considered as a gain stage with gain $\overline{g}_1 = \eta$, and variance $\sigma_{g_1}^2 = \eta(1-\eta)$. Hence

$$\varepsilon_{g_1} = \frac{\sigma_{g_1}^2}{\overline{g}_1} - 1 = -\eta$$

Values of x-ray interaction efficiency η are given in Chapter 4.

As a result of incident x-ray scattering and possibly characteristic x-ray emission in the screen, part of the deposited x-ray energy is re-assigned a new location away from the primary interaction site. This stage is governed by the x-ray energy deposition MTF, MTF$_E$(f), as defined and given in Chapter 4. We have, MTF$_2$(f) = MTF$_E$(f), gain $\overline{g}_2 = 1$, and variance $\sigma_{g_2}^2 = 0$. Hence

$$\varepsilon_{g_2} = \frac{\sigma_{g_2}^2}{\overline{g}_2} - 1 = -1$$

As discussed in section 5.1.2, conversion of deposited x-ray energy into light quanta is a gain only stage with gain $\overline{g}_3 = \overline{N}_{exit}$, the average number of light photons exiting the scintillation screen per interacted x-ray, and a variance $\sigma_{N_{exit}}^2$. $\overline{N}_{exit}$ can be calculated from the generated scintillation light intensity distributions $P(N_{exit})$ of the scintillation screens as following

$$\overline{N}_{exit} = \frac{\sum_{N_{exit}} N_{exit} P(N_{exit})}{\sum_{N_{exit}} P(N_{exit})} = \frac{m_1}{m_0} \tag{5-14}$$

Since

$$< N_{exit}^2 >= \frac{\sum_{N_{exit}} N_{exit}^2 P(N_{exit})}{\sum_{N_{exit}} P(N_{exit})} = \frac{m_2}{m_0} \tag{5-15}$$

then, we have

$$\sigma_{N_{exit}}^2 =< N_{exit}^2 > - \overline{g^2} = \frac{m_2}{m_0} - \left(\frac{m_1}{m_0}\right)^2 \tag{5-16}$$

Finally, the Poisson excess term ε_{g_3} and ε_{Φ_3} can be found by inserting equations 5-14 and 5-16 into equation 5-12

$$\varepsilon_{g_3} = \frac{\sigma_{N_{exit}}^2}{\overline{N}_{exit}} - 1 = \frac{\frac{m_2}{m_0} - \left(\frac{m_1}{m_0}\right)^2}{\frac{m_1}{m_0}} - 1 = \left(\frac{1}{\frac{m_1^2}{m_2 m_0}} - 1\right)\frac{m_1}{m_0} - 1 = \left(\frac{1}{A_S} - 1\right)\overline{N}_{exit} - 1$$

Scintillation light propagation to the screen output is a stage with spatial spreading governed by the scintillation screen optical MTF, $\text{MTF}_O(f)$. We have, $\text{MTF}_4(f) = \text{MTF}_O(f)$, gain $\overline{g}_4 = 1$, and variance $\sigma_{g_4}^2 = 0$. Hence

$$\varepsilon_{g_4} = \frac{\sigma_{g_4}^2}{\overline{g}_4} - 1 = -1$$

$\text{MTF}_O(f)$s for the scintillation screens investigated are given in Chapter 4.

5.2.3. Image Guide to CCD Coupling

Coupling of light photon to the CCD by the image guide is a stage with only a gain. The coupling efficiency K represents a binary selection that a light photon may be transported to the CCD pixels by the image guide. Therefore, gain $\overline{g}_5 = K$, variance $\sigma_{g_5}^2 = K(1-K)$, and Poisson excess term $\varepsilon_{g_5} = -K$. Coupling efficiency K has been described in Chapter 4. K is 0.9 for the plastic scintillating fiber screen based slot x-ray detector, and 0.675 for the CsI:Tl screen based slot x-ray detector.

Conversion of light photons into electrons in the CCD pixels is also a binary selection process governed by the quantum efficiency Q of the CCD. Again, gain $\overline{g}_6 = Q$, variance $\sigma_{g_6}^2 = Q(1-Q)$, and Poisson excess term $\varepsilon_{g_6} = -Q$. An average quantum efficiency Q of 0.40 is used for both the plastic scintillating fiber screen based and the CsI:Tl screen based slot x-ray detectors.

Additive CCD camera electronic noise $S_{a_6}(f)$ is added after the generation of CCD electrons from x-ray interaction. The detailed description of CCD camera noise is given in Chapter 2. This additive electronic noise generally has a Poisson distribution with mean equal to the average number of noise electrons, $\overline{N}_{e\,add}$ per CCD pixel. Therefore $S_{a_6}(f) = \overline{N}_{e\,add}$ in units of electrons/pixel area. $\overline{N}_{e\,add}$ has been estimated to be 2704 (52 e⁻ rms) in Chapter 2.

Integration of electrons in the CCD pixels is a deterministic spreading stage representing the integration of quanta by the CCD and characterized by the CCD pixel MTF, $MTF_{CCD}(f)$. Since both the spatial frequency dependent signal (squared) and NPS are modulated identically by $MTF_{CCD}(f)$, this stage will have no effect on the detector $DQE(f)$.

5.2.4. Detector DQE(f)

Insert all the required parameters as defined above into equation 5-11, the $DQE(f)$ of the slot x-ray detector is given by

$$DQE(f) = \frac{\eta}{\dfrac{1}{A_S \cdot MTF_E^2(f)} + \dfrac{1}{\overline{N}_{enit} \cdot K \cdot Q \cdot MTF_E^2(f) \cdot MTF_O^2(f)} + \dfrac{\overline{N}_{e_{exit}} / \overline{\Phi}_0}{\eta \left(\overline{N}_{enit} \cdot K \cdot Q \cdot MTF_E(f) \cdot MTF_O(f)\right)^2}} \tag{5-17}$$

At zero spatial frequency $f = 0$ lp/mm, if the product of $\overline{N}_{enit} \cdot K \cdot Q$ is $\gg 1$, then equation 5-17 reduces to $DQE(0) = \eta A_S$ (equation 5-2).

In all previous works, the stage accounting for the spatial spreading of deposited x-ray energy was not included in the noise propagation analysis. Equation 5-17 was therefore simplified as

$$DQE(f) = \frac{\eta}{\dfrac{1}{A_S} + \dfrac{1}{\overline{N}_{enit} \cdot K \cdot Q \cdot MTF_{screen}^2(f)} + \dfrac{\overline{N}_{e_{exit}} / \overline{\Phi}_0}{\eta \left(\overline{N}_{enit} \cdot K \cdot Q \cdot MTF_{screen}(f)\right)^2}} \tag{5-18}$$

where $MTF_{screen}(f)$ is the total screen MTF and is actually given by the product $MTF_E(f) \cdot MTF_O(f)$. In a scintillation screen at a given incident x-ray energy where $MTF_E(f)$ is significant less than 1, ignoring the contribution of $MTF_E(f)$ will result in overestimated DQE(f) values at spatial frequencies > 0 lp/mm.

This is the first study in which a stage describing the spatial spreading of deposited x-ray energy is identified as a separate stage in the analysis of noise propagation of an x-ray imaging system. Previous studies assumed x-ray interactions in the x-ray detectors are dominated by photoelectric effect, and therefore $MTF_E(f) \cong 1$. This may be valid for some phosphor screens in diagnostic x-ray energies if the x-ray energy is locally deposited. However, when the energies of a large fraction of incident x-rays are above the K-edge(s) of the phosphor screen high Z elements (such as Gadolinium in Gd_2O_2S:Tb phosphor), the spatial spread of the x-ray energy deposition becomes important. In other x-ray detection materials such as the plastic scintillating fiber screen investigated in this study or in other x-ray imaging applications such as portal imaging where high energy x-rays are used, there are appreciable amount of incident x-rays undergo scattering processes which also cause a spatial spread of deposited x-ray energy. Equation 5-17 can therefore be applied to these imaging situations providing the spatial spreading of x-ray energy deposition can be accurately modeled by theoretical analysis or Monte Carlo simulation.

In this study, DQE(f) values computed using equations 5-17 and 5-18 are compared for slot x-ray detectors using SFS:PS, SFS:Sn:10%, and CsI:Tl screen. SFS:PS represents a scintillation screen in which x-ray interactions are dominated by Compton Scattering. SFS:Sn:10% and CsI:Tl screen represent scintillation screens in which x-ray interactions are dominated by photoelectric effect. The difference between SFS:Sn:10% and CsI:Tl screen is that N_{exit} of CsI:Tl screen is significantly higher (greater than a factor of 2) than that of SFS:Sn:10%. This allows a comparison to be made between the low and high energy conversion efficiency scintillation screens.

Figure 5-2 shows the calculated DQE(f) of (a) SFS:PS, (b) SFS:Sn:10%, and (c) CsI:Tl screen based slot x-ray detectors calculated using equations 5-17 and 5-18. For SFS:PS, there are about 10% and 5% difference in the calculated DQE(0) at 20 and 35 keV x-ray energies, respectively, at spatial frequencies greater than 2 lp/mm. For

SFS:Sn:10%, theses differences are about 10% at 20 keV, and about 35% at 35 keV. The average difference for CsI:Tl screen is about 3% at 20 keV, but increases to about 60% at 35 keV.
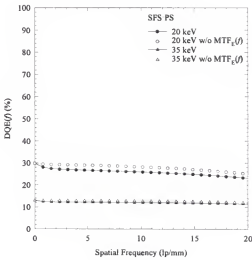
(a)
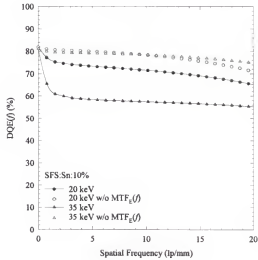
(b)
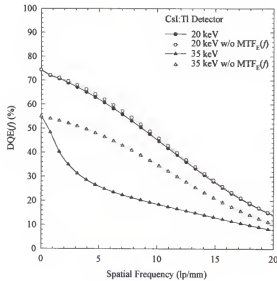
(c)

Figure 5-2. DQE(*f*) of (a) SFS:PS, (b) SFS:Sn:10%, and (c) CsI:Tl screen based slot x-ray detectors calculated using equation 5-17 with and without the consideration of a separate stage for spatial spreading of x-ray energy deposition.

5.3. Zero Spatial Frequency Detective Quantum Efficiency

5.3.1. Scintillation Light Intensity Distribution

Figures 5-3 (a) to (c) show the emitted light intensity distributions, $P(N)$, for the three types of plastic scintillating fiber screens of 20 mm thickness at 20, 35, and 50 keV x-ray energies. $P(N)$s of SFS:PS are always composed of a photopeak and a Compton continuum. $P(N)$'s of both high Z element loaded SFSs are dominated by the photopeak. The photopeaks of the high Z element loaded SFSs shift to a smaller N value than that of the SFS:PS photopeak. This is due to the quenching of scintillation light by the addition of high Z elements in the SFS.

Figure 5-4 shows the scintillation light output intensity distributions for the 150 μm thick CsI:Tl screen 20, 35, and 50 keV x-ray energies. At 20 keV (and x-ray energies below Iodine K-edge), $P(N_{exit})$ is composed of a single photopeak as a result of photoelectric effect domination of x-ray interactions in the CsI:Tl screen. At 35 and 50 keV (x-ray energies above Iodine or Iodine/Cesium K-edges), the escape of Iodine or Iodine/Cesium K-characteristic x-rays leads a wide distribution of N_{exit}, as shown by the appearance of the Iodine or Iodine/Cesium K-escape peaks.

The computed scintillation pulse height spectrum at 50 keV is in agreement with two measured scintillation pulse height spectra of similar CsI:Tl phosphors (Groot, 1991; Swank, 1974). In both measurements, two peaks were observed in each spectrum: the photopeak and a lower peak corresponds to absorption of an x-ray followed by the escape of the K x-rays of I or Cs. The energy difference between the K x-rays of Cs and I was not resolved, either.
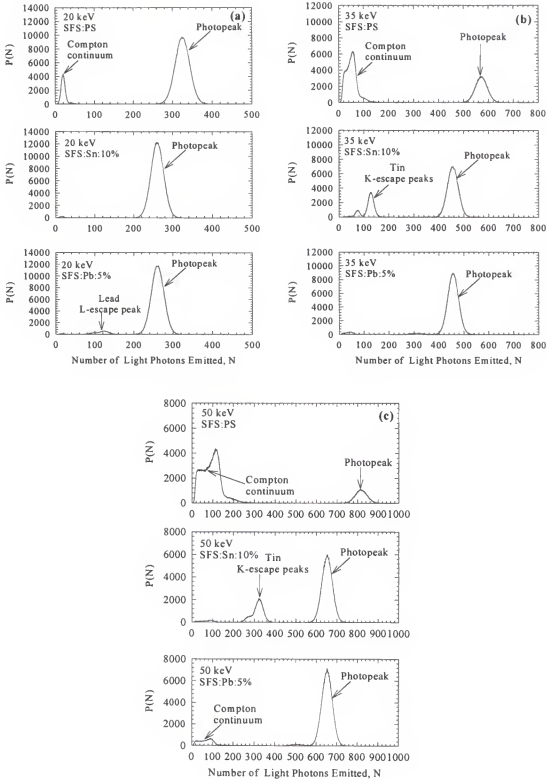
Figure 5-3. P(N) of three types of SFSs of 20 mm thickness at (a) 20, (b) 35, and (c) 50 keV x-ray energies.
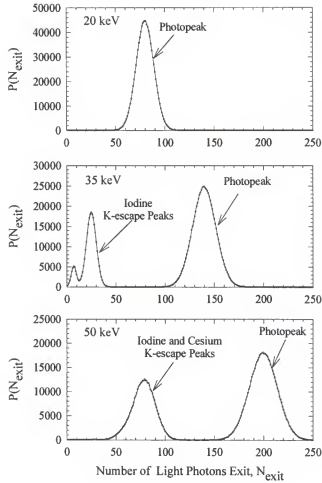
Figure 5-4. $P(N_{exit})$ of the 150 µm thick CsI:Tl screen at 20, 35, and 50 keV x-ray energies.

Figure 5-5 shows the calculated swank factors, A_S, as a function of x-ray energy for (a) three types of SFSs of 20 mm thickness, (b) 5%, 7.5%, and 10% by weight tin loaded SFSs of 20 mm thickness, and (c) 7.5% by weight tin loaded SFSs with thickness varying from 10 to 25 mm. The measured A_S of a Min-R screen is obtained from work done by Trauernicht and Van Metter (1990) and shown in Figure 5-5 (a).

(a)

(b)

(c)

Figure 5-5. Swank factor, A_S, as a function of incident x-ray energy for (a) three types of SFSs of 20 mm thickness, (b) 5%, 7.5%, and 10% by weight tin loaded SFSs of 20 mm thickness, and (c) 7.5% by weight tin loaded SFSs with thickness varying from 10 to 25 mm. Measured Min-R screen A_S values by Trauernicht and Van Metter (1990) is also shown in (a).

A_S of SFS:PS decreases quickly as x-ray energy increases which is due to the reduced photoelectric interaction cross section with increasing incident x-ray energy. Because P(N)'s of SFS:Pb:5% are dominated by the photopeak, A_S of SFS:Pb:5% is close to unity from 15 to 50 keV. At x-ray energies below tin K-edge (29.2 keV), A_S of the SFS:Sn:10% is also close to unity. Although it drops abruptly just above tin K-edge, A_S of SFS:Sn:10% increases as x-ray energy increases further. The results show that Swank factors of both high Z element loaded SFSs are significantly higher than that of a Min-R screen. Figure 5-5 (b) and (c) show that A_S improves with increasing tin concentration from 5 to 10%, but shows little dependence on the SFS thicknesses.

Figure 5-6 shows the calculated swank factors, A_S, as a function of x-ray energy for the 150 μm thick CsI:Tl screen.
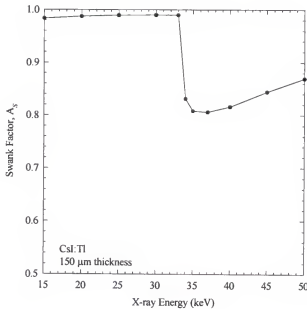
Figure 5-6. Swank factor, A_S, as a function of incident x-ray energy for the 150 μm thick CsI:Tl screen. Measured Min-R screen A_S values by Trauernicht and Van Metter is also shown in (a).

As can be expected from the scintillation light output intensity distribution, A_S of the 150 mm thick CsI:Tl screen is close to unity at x-ray energies below Iodine K-edge. At higher x-ray energies, however, A_S is largely affected by the escape of Iodine or Iodine/Cesium K-characteristic x-rays. This could be a potential problem since high energy x-ray spectra with x-ray energy up to 45 keV have been proposed for scanning slot digital mammography. This effect will depend on the fraction of x-rays with energies greater than the Iodine K-edge in the x-ray spectrum.

5.3.2. Screen and Detector DQE(0)

Figure 5-7 shows calculated (using equation 2) scintillation screen DQE(0) as a function of incident x-ray energy for (a) three types of SFSs of 20 mm thickness, (b) 5%, 7.5%, and 10% by weight tin loaded SFSs of 20 mm thickness, and (c) 7.5% by weight tin loaded SFSs with thickness varying from 10 to 25 mm. The DQE(0) of a Min-R screen is also shown in Figure 5-7 (a). Loading high Z elements significantly improves DQE(0) of the plastic scintillating fiber screen. DQE(0) of SFS:Pb:5% ranges from about 99% to 62% from 15 to 50 keV, and is primarily determined by its x-ray interaction efficiency. DQE(0) of t SFS:Sn:10% is greater than 80%. In the 20 to 30 keV x-ray energy range, DQE(0) of both high Z element loaded SFSs is a factor of three higher than the DQE(0) of the Min-R screen. The combination effect of improved x-ray interaction efficiency (η) and swank factor (A_S) with increasing tin concentration leads to a significant dependence of DQE(0) on the tin concentration. For 7.5% by weight tin loaded SFSs, difference in DQE(0) for different SFS thickness is mainly determined by the difference in x-ray interaction efficiency.

(a)

(b)

(c)
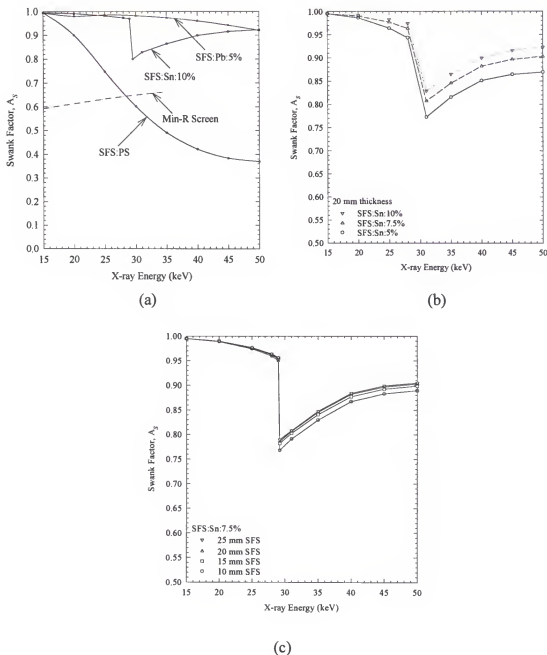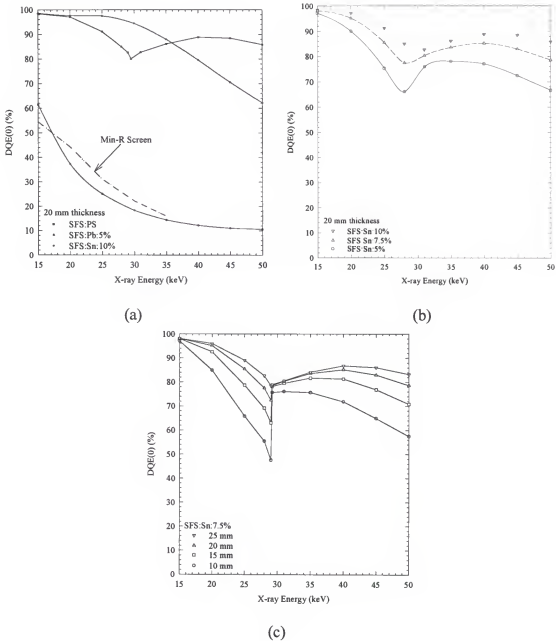
Figure 5-7. DQE(0) plotted as a function of incident x-ray energy for (a) three types of SFSs of 20 mm thickness, (b) 5%, 7.5%, and 10% by weight tin loaded SFSs of 20 mm thickness, and (c) 7.5% by weight tin loaded SFSs with thickness varying from 10 to 25 mm.

Figure 5-8 shows calculated (using equation 2) scintillation screen DQE(0) as a function of incident x-ray energy for the 150 µm thick CsI:Tl screen. At x-ray energies below Iodine K-edge, DQE(0) is primarily determined by the x-ray interaction efficiency

in the 150 μm thick CsI:Tl screen. The major screen noise at zero spatial frequency therefore arises from the fluctuation in the number of x-rays interacted in the CsI:Tl screen at mammography x-ray energies. Further increase in the CsI:Tl screen thickness would improve the screen noise performance but, as mentioned earlier would affect the spatial resolution and scintillation light output of the CsI:Tl screen.
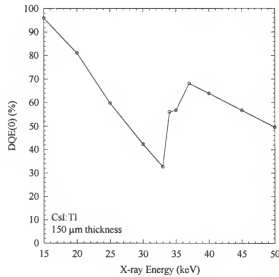
Figure 5-8. DQE(0) plotted as a function of incident x-ray energy for the 150 μm thick CsI:Tl screen.

Figure 5-9 shows in dashed lines the calculated (using equation 16) detector DQE(0) as a function of incident x-ray energy for slot x-ray detectors using the three types of SFSs of 20 mm thickness, and the 150 μm thick CsI:Tl screen. Also shown in Figure 5-9 are the corresponding DQE(0) of the scintillation screen for each slot x-ray detector. For SFS:PS based slot x-ray detector, DQE(0) is dominated by its x-ray interaction efficiency and decreases with increasing x-ray energy. For both high Z element loaded SFSs, DQE(0) increases as x-ray energies increases from 15 keV. This is a result of increased N_{exit} at higher x-ray energies. DQE(0) reaches the maximum at 25

keV for SFS:Pb:5% and 20 keV for SFS:Sn:10% based slot x-ray detector, and is largely affected by the decreasing x-ray interaction efficiency at higher x-ray energies.

(a)

(b)

(c)

(d)
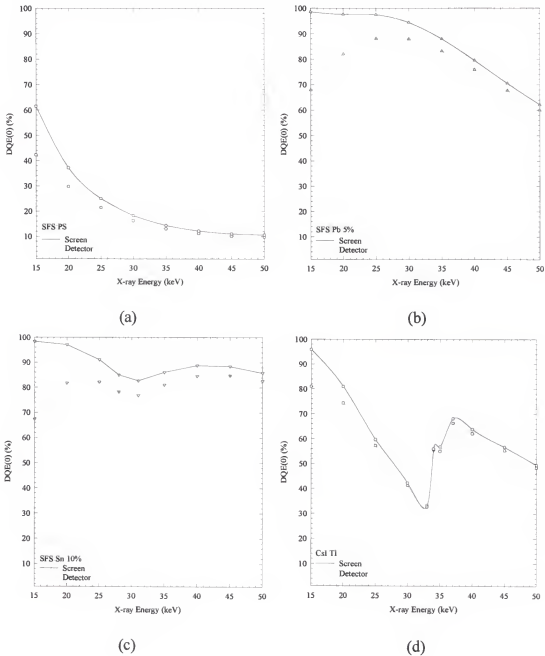
Figure 5-9. DQE(0) as a function of incident x-ray energy for slot x-ray detectors using (a) three types of SFSs of 20 mm thickness, and (b) the 150 μm thick CsI:Tl screen.

For CsI:Tl screen based slot x-ray detector, DQE(0) is always dominated by its x-ray interaction efficiency. Except at very low x-ray energies, DQE(0) of the CsI:Tl screen based slot x-ray detector is close to that of the CsI:Tl screen. This is due to that N_{exit} of CsI:Tl screen at x-ray energies above 20 keV is high and the noise contributions from other stages are reduced. The effect of other noise sources manifest due to the small N_{exit} for both high Z element loaded screens from 15 to 30 keV. DQE(0) values of both high Z element loaded SFSs are significantly lower than that of the corresponding screens.

5.3.3. DQE(0) and X-ray Exposure and CCD Electronic Noise

Figure 5-10 shows the dependence of DQE(0) on x-ray exposure to the slot x-ray detector at (a) 20 and (b) 35 keV x-ray energies. At 20 keV, DQE(0) values of all the slot x-ray detectors improves with increased x-ray exposure up to about 5 mR. Whereas at 35 keV, DQE(0) values saturate at about 1 mR. This is due to the large difference in the fluence (Φ_0) of the incident x-rays at the two x-ray energies. Φ_0 is about 32 per CCD pixel per mR at 25 keV and about 101 at 35 keV. The x-ray quantum noise at 35 keV is therefore lower than that at 20 keV for the same detector exposure level. The fact that, at 20 keV, DQE(0) improves from 0.1 to 5 mR indicates the additive electronic noise level of about 50 electrons rms in the slot x-ray detector is still significant.

Figure 5-11 shows the dependence of DQE(0) on the additive CCD electronic noise level at (a) 20 and (b) 35 keV x-ray energies and x-ray exposure level of 1 mR. Similarly, due to a factor of greater than two in the number of incident x-rays, the additive CCD electronic noise has a smaller effect on DQE(0) at 35 keV. At 20 keV, It is seen the reducing the additive electronic noise level from the estimated 2704 electrons to about 1000 electrons can provide about 40%, 30%, and 10% improvement in DQE(0) values for SFS:PS, two high Z element loaded SFSs, and the CsI:Tl screen based slot x-ray detectors, respectively.
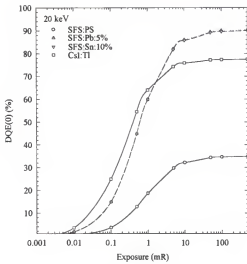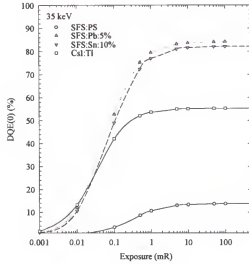
(a)   (b)

Figure 5-10. Dependence of DQE(0) on x-ray exposure to the slot x-ray detector at (a) 20 and (b) 35 keV x-ray energies.
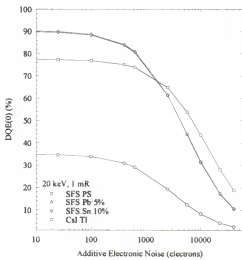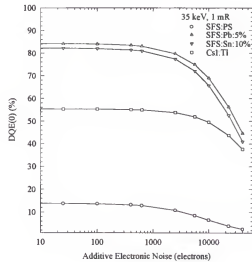
(a)   (b)

Figure 5-11. Dependence of DQE(0) on the additive CCD electronic noise level at (a) 20 and (b) 35 keV x-ray energies.

5.3.4. Comparison with Published Works

Swank factor of some other type of CsI:Tl screens used in x-ray image intensifiers has been calculated or measured or by a number of investigators. Swank (1973) calculated the A_S values of a 111 µm thick and a 222 µm thick CsI crystals only taking account of the energy deposition variation for incident x-rays. Table 5-1 compares the calculated values by Swank and the results of present study. At 20 and 30 keV, there is little difference in A_S values between the two studies, although the present study takes into account the effect of scintillation light propagation within the CsI crystal. These results showed that A_S of CsI crystal is mainly determined by the x-ray absorption processes. At 40 and 50 keV, the present results for the 150 µm thick CsI crystal are within the range of A_S values calculated for the 111 and 222 µm thick CsI crystals by Swank. This good agreement demonstrates the reasonable accuracy of this study.

Table 5-1. Comparison of Swank factors, A_S, calculated from this study with the work done by Swank (1973).

Energy (keV)	Present Study (150 µm CsI)	Swank Work	
		(111 µm CsI)	(222 µm CsI)
20	0.99	1.00	1.00
30	0.99	1.00	1.00
40	0.82	0.76	0.82
50	0.87	0.85	0.89

Groot (1991) measured Swank factor of some prismatic CsI crystals. In that measurement, A_S was measured from the scintillation pulse height spectra of the CsI crystal layers using an Am-241 monoenergetic x-ray source (59.6 keV). A_S was ~0.9 and varied only slightly with the CsI crystal layer thicknesses from 250 to 500 µm. In an earlier study, Swank (1974) measured the A_S of an approximately 100 µm thick CsI:Tl phosphor using the Am-241 x-ray source. A_S was found to be 0.86. The results from the

present calculations are consistent with these measured values. Exact matches, however, are not expected due to different CsI crystal geometry.

5.4. Spatial Frequency Dependent Detective Quantum Efficiency

5.4.1. X-ray Exposure

Figure 5-12 shows the dependence of DQE(f) on the x-ray exposure at 20 keV x-ray energy for slot x-ray detectors using (a) SFS:PS, (b) SFS:Pb:5%, (c)SFS:Sn:10%, and (d) 150 μm thick CsI:Tl screen. All SFSs are 20 mm thick SFSs and made of 20 μm diameter scintillating fibers.

At all non zero spatial frequencies, increasing the detector exposure generally improves DQE(f) values for all slot x-ray detectors. This effect is more significant at lower x-ray exposures (less than 5 mR) where electronic noise contribution is relatively high. For all SFS based slot x-ray detectors, improvement in DQE(f) with increased x-ray exposure only shows a slight increase at high spatial frequencies. When x-ray exposure increases from 1 to 5 mR, the DQE(f) improves by a factor of ~ 1.6, 1.4, and 1.4 for the SFS:PS. SFS:Pb:5%, and SFS:Sn:10% based slot x-ray detector, respectively.

DQE(f) values of CsI:Tl screen based slot x-ray detector, however, show a very strong dependence on the x-ray exposure. For example, from 1 to 5 mR, DQE(f) increases by a factor of about 1.1, 1.4, 1.8, 2.3 at spatial frequencies of 0, 5, 10, and 15 lp/mm, respectively. This difference in dependence of DQE(f) on the x-ray exposure between the SFS and CsI:Tl based slot x-ray detectors is due to the lower values of MTF$_O$(f) for CsI:Tl screen compared to a SFS.
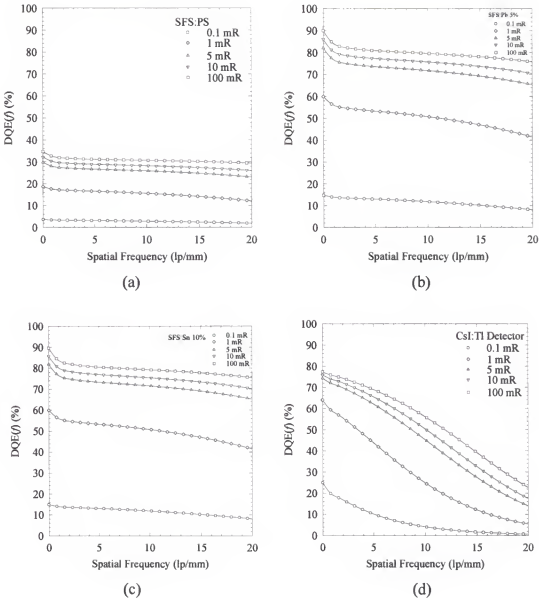
Figure 5-12. Dependence of DQE(*f*) on the x-ray exposure at 20 keV x-ray energy for slot x-ray detectors using (a) SFS:PS, (b) SFS:Pb:5%, (c)SFS:Sn:10%, and (d) 150 μm thick CsI:Tl screen.

5.4.2. CCD Electronic Noise

Figure 5-13 shows the dependence of DQE(*f*) on the additive CCD electronic noise level at 20 keV x-ray energy for slot x-ray detectors using (a) SFS:PS, (b)
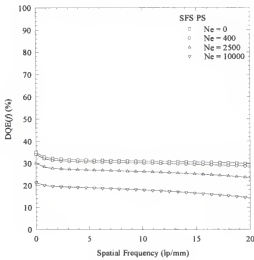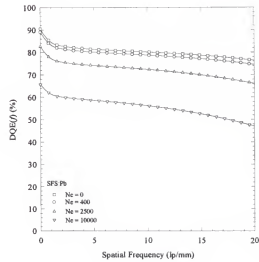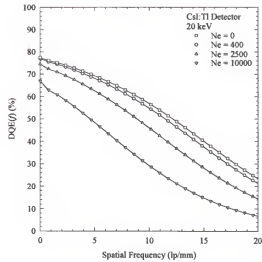
Figure 5-13. Dependence of DQE(*f*) on the additive CCD electronic noise level at 20 keV x-ray energy for slot x-ray detectors using (a) SFS:PS, (b) SFS:Pb:5%, (c)SFS:Sn:10%, and (d) 150 μm thick CsI:Tl screen.

SFS:Pb:5%, (c)SFS:Sn:10%, and (d) 150 µm thick CsI:Tl screen. All SFSs are 20 mm thick SFSs and made of 20 µm diameter scintillating fibers.

Dependence of DQE(f) on the additive CCD electronic noise is similar to that on the x-ray exposure. This can be expected from analyzing equation 5-16. For all slot x-ray detectors, DQE(f)s almost approach their maximum values (ideal situation where there is no CCD electronic noise, $N_e = 0$) by reducing CCD electronic noise level from 2500 electrons to 400 electrons.

In CCD based digital x-ray imaging, a lot of effort has been devoted to reduce the CCD electronic noise to near zero levels. Unfortunately, this usually increase the complexity and cost of the imaging system. The results from this study indicates that for a particular imaging system, it may not be necessary to reduce the additive noise component in the detector to about zero level. An analysis similar to that performed in this study may eliminate many technical limitations imposed by a poor understanding of the actual technical requirement.

5.4.3. Image Guide Coupling Efficiency

Figure 5-14 shows the dependence of DQE(f) on the image guide coupling efficiency K at 20 keV x-ray energy for slot x-ray detectors using (a) SFS:PS, (b) SFS:Pb:5%, (c)SFS:Sn:10%, and (d) 150 µm thick CsI:Tl screen. All SFSs are 20 mm thick SFSs and made of 20 µm diameter scintillating fibers. In all cases, image guide coupling efficiency significantly affects the DQE(f)s. An idea coupling ($K = 1$) is always desired to improve the DQE(f) of the slot x-ray detectors.

In CCD based x-ray imaging system, couplings of scintillation screen and CCD have been achieved through the use of optical fiber image guide and optical lens. The lens typically has coupling efficiency at least one order of magnitude lower than that of fiber
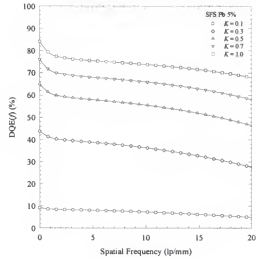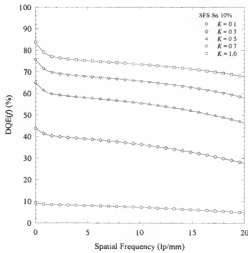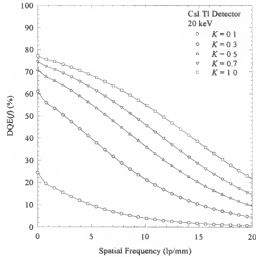
Figure 5-14. Dependence of DQE(*f*) on the image guide coupling efficiency at 20 keV x-ray energy for slot x-ray detectors using (a) SFS:PS, (b) SFS:Pb:5%, (c)SFS:Sn:10%, and (d) 150 μm thick CsI:Tl screen.

image guide. In some applications, tapered fiber image guides were also used as the coupling medium. For example, with a 2:1 ratio tapered image guide, the coupling efficiency is less than 25%. These low coupling efficiency designs limited the maximum achievable detector DQE(f). Based on the results of this study, a better design of a CCD based imaging system should use an 1:1 ratio image guide to maximize the coupling efficiency. A necessary image reduction can then be achieved by CCD binning, i.e., combining adjacent CCD pixel charges in the CCD readout.

5.4.4. CCD Quantum Efficiency

Figure 5-15 shows the dependence of DQE(f) on the quantum efficiency Q of the CCD at 20 keV x-ray energy for slot x-ray detectors using (a) SFS:PS, (b) SFS:Pb: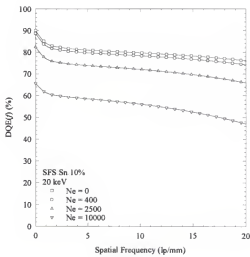5%, (c)SFS:Sn:10%, and (d) 150 μm thick CsI:Tl screen. All SFSs are 20 mm thick SFSs and made of 20 μm diameter scintillating fibers. Dependence of DQE(f) on the CCD quantum efficiency is similar to that on the image guide coupling efficiency. However, it is shown that for a practically achievable CCD quantum efficiency of 0.7, DQE(f)s of all the SFS based slot x-ray detectors approach to their maximum values when $Q = 1.0$. The reason is that the image guide coupling efficiency is high (0.9) for all SFS based slot x-ray detectors. For the CsI:Tl screen based slot x-ray detector with a 0.68 coupling efficiency, however, a CCD quantum efficiency close to unity is needed to improve its DQE(f) at high spatial frequencies. This is a very useful conclusion that will help the design and optimization of CCD based x-ray imaging detectors. In order to achieve high DQE(f), it is desired to efficiently couple the scintillation screen to the CCD. This will allow the use of more economic CCDs which may have lower quantum efficiency than other expensive and specialized CCDs.
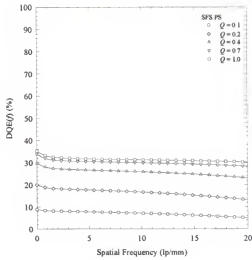
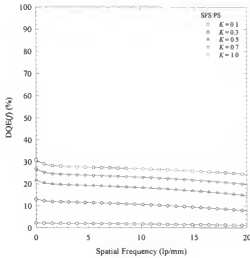(a)
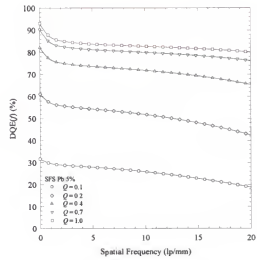
(b)
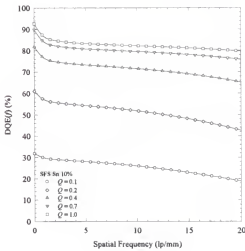
(c)
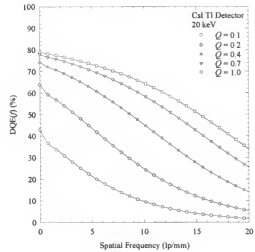
(d)

Figure 5-15. Dependence of DQE(f) on the quantum efficiency of CCD at 20 keV x-ray energy for slot x-ray detectors using (a) SFS:PS, (b) SFS:Pb:5%, (c)SFS:Sn:10%, and (d) 150 μm thick CsI:Tl screen.

CHAPTER 6
CONCLUSIONS AND FUTURE WORK

6.1. Conclusions based on Results from Scatter Study

The widths of slot x-ray detectors that have been under investigation for scanning slot digital mammography ranging from about 4 mm to 20 mm. For this relatively small range, scatter to primary radiation ratios (S/P) showed a strong dependence on the selected slot detector widths. S/P ratios were found to decrease by a factor of greater than two when slot detector width is reduced from 20 mm to 4 mm at x-ray energies used in mammography. This shows that the use of a very narrow slot detector would efficiently reject scattered radiation from reaching the detector. As an example, S/P ratios for a 4 mm wide slot detector were found to be between ~0.10 to 0.17, which are similar to those encountered in conventional screen-film mammography when a 5:1 ratio grid is used. However, in a scanning slot imaging system, only the size of the x-ray field that is equal to the slot detector area is used at any moment during the image scan. The required x-ray tube output is therefore inversely proportional to the slot detector width. For very small detector width, this requirement in x-ray tube output generally results in either unacceptably high x-ray tube heat loading or long imaging time which is practically limited by patient motion and patient inconvenience. For example, given a short imaging time of about five seconds, the use of a 4 mm wide slot detector would require an x-ray tube output exposure rate which is about five times that when a 20 mm wide slot detector is used. This demands a very high x-ray tube power which approaches the limit of current x-ray tube technology. Efficient use of the x-ray tube output by the use of a wider slot detector would reduce the x-ray tube power requirement and could also reduce image

154

scan time and thereby minimize patient motion artifacts as well as patient discomfort. In addition, more efficient use of the x-ray beam would enable x-ray filters to be used to optimize the shape of the x-ray spectrum to better match the imaging needs in clinical situations. The selection of 10 mm width for the scanning slot detector approach in this study provides a tradeoff between scatter performance and x-ray tube power requirement.

Increasing slot detector width to 10 mm inevitably increases the amount of scatter to the detector, and the resulted S/P ratios was found to increase by a factor of about 1.8 compared to that of a 4 mm wide slot detector. It is necessary to investigate methods to reduce the scatter contribution at this relatively large slot detector width without compromising the x-ray tube loading. In this study, the use of an air gap introduced between the Lucite phantom and a 10 mm wide detector was found to be very efficient in rejecting scattered radiation. S/P ratios reduce by a factor of about two and three using 1.5 cm and 3.0 cm air gaps, respectively. S/P ratios are in the range of 0.05 to 0.13 with the use of a 3 cm air gap.

In conventional screen-film radiography, scattered radiation is rejected by the use of grids. The radiation exposure to the screen, however, needs to be maintained at a constant level to ensure that the resultant film density is satisfactory. This requires an increase in the x-ray tube output to compensate for any removed scattered and primary x-ray photons, and normally leads to an approximate doubling of the breast mean glandular dose. Use of a scatter reduction grid with a digital slot detector has been show to increase the mean glandular dose by between 30 and 40% as a result of the increased attenuation of the primary x-ray beam. The use of a grid also complicated the detector design. The use of air gaps can achieve scatter reduction without necessarily increasing the radiation dose and is an attractive option for use in a slot detector geometry particularly since the necessary air gap sizes (~ 3 cm) are much smaller than those (> 40 cm) normally considered in conventional screen-film mammography. The effect on the patient dose by the use of an air gap with a slot detector geometry will depend on both the characteristics

of the detector, and on the manner in which the air gap is introduced. If the detector is quantum noise limited, there will be no need to increase the primary exposure to maintain the same signal to noise ratio (SNR) providing the source to detector distance is kept constant. However, if there are significant electronic noise components from the detector, then an increase in the x-ray tube output would be needed to maintain the same SNR. For a 3 cm air gap introduced by moving the detector away from the patient, the patient dose would increase by about 10% because of the inverse square law fall off in x-ray beam intensity for a source to detector distance of ~60 cm. In summary, the use of a 10 mm wide slot detector with a 3 cm air gap geometry results in efficient scatter rejection with negligible increase in patient radiation dose.

In the slot detector geometry, S/P ratios decrease as x-ray photon energy increases. S/P ratios decreased about 33% between when x-ray energy increased from 15 and 50 keV for a 10 mm wide slot detector using 4 cm thick Lucite phantom as the scattering medium. This differs from the case of mammography performed with large area detectors where S/P ratios generally shown little dependence on the x-ray energy. The reason for this behavior is that in a slot detector geometry, it is only the forward scattered x-ray photons which contribute to the S/P ratio whereas in large area detectors, x-ray photons scattered through large angles will also contribute to the S/P ratio. The relatively constant energy dependence of the S/P ratio for area detectors is a result of the increasing contribution of Compton scattered photons which increase with photon energy. Coherent scattered photons are primarily forward scattered and their contribution to the S/P ratio generally decreases with increasing photon energy. The use of an air gap affects the relative contribution from coherent scatter and Compton scatter. At 20 keV, there are about four times more x-ray photons which undergo Compton scattering than coherent scattering in the Lucite phantom. Despite this fact, the contribution of coherent scatter to S/P ratio is larger than that of Compton scatter at energies below 25 keV with no air gap. This occurs because most coherently scattered photons have a small angular divergence

whereas the angular distribution of Compton scattered photons is approximately isotropic. This also explains why an air gap is more efficient in rejecting the Compton scattered photons and why the two processes make equal contributions at a higher x-ray energy (~36 keV) with the use of a 3 cm air gap

X-ray detection materials currently under investigation for scanning slot digital mammography include Gd_2O_2S:Tb phosphor, CsI:Tl crystal, plastic scintillating fiber screens, and hybrid photodiode array. The results in this study show that choice of x-ray detection material in a slot detector had very little effect on the resultant S/P ratio. In the case of area detectors, however, the S/P ratios of an ideal screen and a mostly used mammography (Kodak Min-R) screen show markedly different responses. In a slot detector geometry, the majority of scattered photons reaching the slot detector are photons scattered with very small angles. Their directions, and therefore energies, are very similar to those of the primary photons. As a result, the slot detector has very similar efficiencies in detecting the primary photons as well as scattered photons. S/P ratios will not change by changing the x-ray detection material. In an area detector geometry, the efficiency of a detector in detecting the scattered photons is higher than that in detecting primary photons due to the increased paths of scattered photons in the detection material. The efficiency in detecting scattered photons depends on the x-ray detection material. Thus, S/P ratios are different for different x-ray detection materials. This finding suggests that the results obtained in this study will be applicable to any type of detection material providing the geometry is similar to those investigated in this work.

6.2. Conclusions Based on Results from Signal Propagation Study

Even utilizing a 2 cm thick plastic scintillating fiber screen (SFS) made of polystyrene core material (SFS:PS), the x-ray interaction efficiency at 20 keV is about 40% and is much lower than that of about 70% for typical Gd_2O_2S:Tb phosphor screens

($\sim$ 50 μm thickness) used in screen-film mammography and early design of scanning slot digital mammography detectors. Loading high Z elements including lead and tin into the core materials of the plastic scintillating fibers significantly improves the x-ray interaction efficiency. The resultant x-ray interaction efficiencies nearly approach 100% at 20 keV. A 2 cm thick and 7.5% by weight tin loaded SFS results in sufficient x-ray interaction efficiency. Further increase in SFS thickness and tin concentration results in only slight increase in x-ray interaction efficiency, and may lead to other problems such as difficulty in the alignment of fibers to the direction of incident x-ray photons. For the 150 μm thick CsI:Tl screen, the x-ray interaction efficiency is about 80% at 20 keV, but reduces to about 40% at 30 keV. Although this x-ray interaction efficiency averaged about 20% greater than that of a Min-R screen used in screen-film mammography, there is a potential problem of low x-ray interaction efficiency for CsI:Tl screen based scanning slot digital mammography system since the use of high energy x-ray spectra have been proposed to reduce the x-ray tube power requirement. The optimal x-ray spectra to be used in such a scanning slot digital mammography system should be further studied.

The number of scintillation light photons output from the screen per interacted x-ray is generally in the range between 30 and 50 for all the SFS at x-ray energies normally encountered in mammography. This number improves to about 80 to 120 for a CsI:Tl screen. CsI:Tl screen therefore generates more than a factor of two more signals compared to a SFS. The resulted number of CCD electrons generated per 20 keV incident x-ray, N_e, is about 6 for slot x-ray detector using SFS:PS, and $\sim$ 12 for slot x-ray detector using high Z element loaded SFSs. This large difference between SFS:PS and high Z element loaded SFSs is mainly due to the large difference in their x-ray interaction efficiency despite of the fact that high Z element loaded SFSs produce less scintillation light output at $\sim$ 20 keV x-ray energies. There is negligible difference in N_e when tin concentration varies from 5% to 10% for a 20 mm thick SFS, and very small improvement in N_e for SFS:Sn:7.5% when its thickness increases from 15 to 25 mm.

These imply that a ~ 20 mm thick SFS loaded with concentration of tin in the range from 5 to 10% can provide significantly improved signal performance for a SFS based slot x-ray detector for mammography. For CsI:Tl screen based slot x-ray detector, N_e per 20 keV incident x-ray is about 18, about 50% increase compared to the slot x-ray detector using a high Z element loaded SFS. However, N_e at 30 keV for CsI:Tl screen is reduced to about 14 and is comparable to that for a high Z element loaded SFS based slot x-ray detector. One would expect to increase the CsI:Tl screen thickness to improve its x-ray interaction efficiency. This, unfortunately, will lead to a reduced number of scintillation light output per interacted x-ray and a reduction in spatial resolution. Experimental measurements were also performed to compare the signal performance between the CsI:Tl screen and Gd_2O_2S:Tb phosphor screen (Min-R screen) based slot x-ray detectors. It was found that the use of the CsI:Tl screen in a slot x-ray detector produces comparable signal intensity to the Gd_2O_2S:Tb phosphor based slot x-ray detector. In summary, a SFS based slot x-ray detector has poorer image signal performance at ~ 20 keV compared to a CsI:Tl screen based slot x-ray detector. However, the image signal performance of the CsI:Tl based detector depends strongly on the x-ray energy, and reduces significantly when the x-ray energy increases from 20 to 30 keV.

For all SFS investigated, their modulation transfer function MTF(f) are excellent and exceeds 60% at spatial frequency of 20 lp/mm. Loading high Z element into SFS resulted in a relatively small loss of spatial resolution even at x-ray energies above tin K-edge. MTF(f) values of the CsI:Tl screen are considerably less than that of the SFS at non-zero spatial frequencies. At 20 lp/mm, MTF(f) value of the CsI:Tl screen is about 10%. It was found that despite a significant reduction in CsI:Tl screen MTF(f) at x-ray energies above Iodine K-edge, scintillation light dispersion within the CsI:Tl screen limits the MTF(f) values at all spatial frequencies. This is the major difference between CsI:Tl screen and the SFS although the CsI:Tl crystals also have a columnar structure. A relatively large fraction of scintillation light emitted in CsI:Tl screen can travel through a

number of CsI:Tl crystals before reaching the screen output, whereas in a SFS extramural absorbing material (EMA) can be added between the fibers to reduce light dispersion within one fiber diameter (20 µm). The use of high x-ray energy spectra such as 40 KV was found to produce similar spatial resolution performance as that at 20 keV. This is because of the relatively small fraction of x-rays with energies above Iodine K-edge. The major problem of the CsI:Tl screen is again related to the tradeoff between its x-ray interaction efficiency and spatial resolution. Increasing CsI:Tl screen thickness to improve its image signal production at higher x-ray energies could lead to a significant loss of spatial resolution due to scintillation light dispersion. A CsI:Tl screen based slot x-ray detector will potentially have to stay with a low x-ray interaction efficiency to maintain its spatial resolution performance.

Measurement of limiting spatial resolution shows the CsI:Tl screen based slot x-ray detector is about 15 lp/mm for scanning speed ranging up to 4 cm/seconds. The limiting spatial resolution of a Gd_2O_2S:Tb based slot x-ray detector, however, is reduced from about 15 lp/mm to about 6 lp/mm when the scanning speed was increased from 1 cm/second to 4 cm/second. These results demonstrated that the use of a CsI:Tl screen in a scanning slot detector approach almost eliminates the dependence of spatial resolution on scanning speed which is the major problem associated with the initial design of scanning slot detectors for mammography. The use of a CsI:Tl screen in the scanning slot digital mammography approach produces better image signal and spatial resolution performance than the use of a Gd_2O_2S:Tb phosphor screen. Our preliminary measurements of a prototype pure plastic SFS based image intensifier imaging system demonstrated that the spatial resolution performance of a SFS is mainly determined by the scintillating fiber diameter used. The scintillation light production of a SFS, however, is low and needs to be greatly improved for use in mammography imaging applications.

6.3. Conclusions Based on Results from Noise Propagation Study

For SFS:PS, it was found that the Swank factor reduces from almost unity at 15 keV to about 0.6 at 30 keV. The use of high Z element loaded SFS largely improves the noise performance compared to SFS:PS. The Swank factor is close to unity from 15 to 50 keV for SFS:Pb:5%, and below tin K-edge for all tin loaded SFS. The Swank factor was found to improve slightly with increasing tin concentration from 5 to 10%, but shows little dependence on the SFS thicknesses. In the signal performance analysis, it was found that SFS:PS has the highest spatial resolution performance of all SFS. At typical x-ray energies (~ 20 keV) used in mammography, SFS:PS also produces the highest number of scintillation photons per interacted x-ray. It may appear that SFS:PS is the best SFS that should be used because one can always use a thicker SFS:PS to improve the x-ray interaction efficiency compared to those high Z element loaded SFS. It is by this Swank factor analysis that it is proved that loading high Z element in SFS is essential to reduce the secondary noise sources from x-ray to light conversion. When a particular imaging application requires the use of high energy x-ray, the emission and reabsorption of tin K-characteristic x-rays in a tin loaded SFS may contribute a significant noise component to the image. In mammography, because the majority of x-rays produced at even very high tube potential (greater than tin K-edge) have energies below tin K-edge, the effect of tin K-characteristic x-rays on image noise can be very small. Similarly, Swank factor of the 150 μm thick CsI:Tl screen is close to unity at x-ray energies below Iodine K-edge, and largely affected by the escape of Iodine or Iodine/Cesium K-characteristic x-rays at higher x-ray energies. The results also show that Swank factors of both high Z element loaded SFS and the CsI:Tl screen are significantly higher than that of about 0.7 for a Min-R screen.

The DQE(0) values of the 2 cm thick high Z element loaded SFSs are greater than 80% in the x-ray energy range from 15 to 30 keV. This is a factor of three higher than the

DQE(0) of the Min-R screen. The combination effect of improved x-ray interaction efficiency and swank factor with increasing tin concentration resulted in a much clear dependence of DQE(0) on tin concentration in the SFS. In the signal performance study, it was shown that the image signal has very little dependence on the tin concentration. The improvement of DQE(0) with increasing tin concentration, however, indicates that a higher tin concentration up to a maximum of 10% should be employed to improve the noise performance. DQE(0) of the CsI:Tl screen is about 80% at 20 keV but quickly reduces to about 40% at 30 keV. Again, the main problem with the use of CsI:Tl screen is its lower x-ray interaction efficiency at relatively high x-ray energies. The results show that this may lead to a higher quantum noise level in the image compared to current screen-film mammography operated at about 20 keV x-ray energies.

Variations of x-ray exposure to the detector and CCD electronic noise showed a relatively large effect on the SFS based slot x-ray detector than on the CsI:Tl screen based slot x-ray detector. This behavior is a result of lower x-ray energy conversion efficiency and scintillation light collection efficiency of a SFS compared to the CsI:Tl screen. At 20 keV, DQE(0) values of all x-ray detectors improves with increased x-ray exposure up to about 5 mR. This result indicates the additive electronic noise component in the slot x-ray detector is still significant. At 20 keV, it is seen that reducing the additive electronic noise level from the estimated 2704 electrons to about 1000 electrons can provide about 30%, and 10% improvement in DQE(0) values for two high Z element loaded SFSs and the CsI:Tl screen based slot x-ray detectors, respectively. Since there is a relatively large amount of noise existed in current CCD electronics, it is advantageous to use the CsI:Tl screen based slot x-ray detector despite of the better spatial resolution performance of the SFS.

For all slot x-ray detectors, DQE(f)s almost approach their maximum values (ideal situation where there is no CCD electronic noise) by reducing CCD electronic noise level from 2500 electrons to 400 electrons. This indicates that for a particular imaging system,

it may not be necessary to reduce the additive noise component in the detector to about zero level, which could considerably increase the complexity and cost of the imaging system. An analysis similar to that performed in this study may eliminate many design frustrations imposed by a poor understanding of the actual technical requirement.

The results shows that an idea optical coupling between the scintillation screen and the CCD is desirable to improve the DQE(f) of the slot x-ray detectors. Under the condition of relatively high image guide coupling efficiency, it is shown that DQE(f)s of all the slot x-ray detectors approach to their maximum values (as can be achieved with a 100% CCD quantum efficiency) at a practically achievable CCD quantum efficiency (~ 70%). This is a very useful conclusion that will help the design and optimization of CCD based x-ray imaging detectors. Whenever possible, an efficient coupling method should be employed. This allows the use of more economic CCDs which may have lower quantum efficiency than other expensive and specialized CCDs.

In this study, a new term which accounts for the spatial spreading of deposited x-ray energy is included in the cascaded analysis of noise propagation in an x-ray imaging system. Previous studies assumed x-ray interactions in the x-ray detectors are dominated by photoelectric effect, and therefore frequently overestimated the DQE(f) of the x-ray imaging systems where spatial spreading of deposited x-ray energy is significant. Calculations performed on the representing x-ray detectors demonstrated, in applications where the emissions of energetic characteristic x-rays are involved, that the existing cascaded noise propagation model could overestimate the detector DQE(f) by as high as 60%.

6.4. Future Work

One important task is to investigate methods to maximize the scintillation light output from a high Z element loaded SFS. The results in this study have shown that the

use of a high Z element loaded plastic scintillating fiber screen has the potential to produce a scanning slot x-ray detector with both very high spatial resolution and excellent noise performance for use in mammography. However, the major problem associated with a SFS has been demonstrated to be the very low scintillation light out from the SFS. During the course of this research project, three key advancements over current plastic scintillating fiber technology have been made: an improved x-ray energy conversion efficiency of 4.5% compared to that of 3% for polystyrene based scintillator; low refractive index polymer as the scintillating fiber cladding which could potentially increase the scintillation light collection efficiency from 3% to 7.5%; and a concentration of tin up to 10% by weight has been incorporated into the polystyrene based plastic scintillator with only 20% light loss due to quenching. This new tin loaded plastic scintillator is in thermoplastic from which scintillating fibers may be successfully produced. Continuing future work toward making plastic scintillating fibers with characteristics specified in this study should be carried out. The scintillation light output from the tin loaded SFS needs to be quantified and compared to that from other scintillation screens.

Additionally, the imaging performances including signal intensity, spatial resolution, and DQE of the CsI:Tl screen based slot x-ray detector should be studied using various combinations of x-ray tube anode and filter materials. It is shown that the DQE of the CsI:Tl based slot x-ray detector depends strongly on the x-ray energy. To reduce the x-ray tube loading requirement, x-rays with energies up to 40 keV have been considered for use in the scanning slot digital mammography approaches. A greatly reduced detector DQE is expected at x-ray energies just below the Iodine K-edge. The effects of different x-ray spectra on the detector imaging performances should be quantified from which optimal x-ray spectra for a range of breast thicknesses and compositions may be determined.

LIST OF REFERENCES

Arnold, B.A.; Bjarngard, B.E., "The effect of phosphor K x-rays on the MTF of rare-earth screens," Med. Phys. 6, 500-503, 1979.

Barnes, G.T.; Brezovich, I. A., "The intensity of scattered radiation in mammography," Radiology 126, 243-247, 1978.

Barnes, G.T., "Mammography Equipment: Compression, Scatter Control, and Automatic Exposure Control," Syllabus: A Categorical Course in Physics Technical Aspects of Breast Imaging, RSNA Publications, Oakbrook, IL, 59-68, 1992.

Barrett, H.H.; Swindell, W., Radiological Imaging-The Theory of Image Formation, Detection, and Processing, Academic, New York, 1981.

Beaman, S.A. and Lillicrap, S.C., "Optimum x-ray spectra for mammography," Phys. Med. Biol. 27, 1209-1220, 1982.

Becker, J., Eriksson, L. A., Moberg, L.C., "On the use of tin-loaded plastic scintillators in Mossbauer spectroscopy," Nuclear Instruments and Methods 123, 199-201, 1975.

Berger, M.J.; Hubbell, J.H., "XCOM: photon cross sections on a personal computer," Report No. NBSIR 87-3597, National Institute of Standards and Technology, Gaithersburg, MD, 1987.

Birks, J. B., The theory and Practice of Scintillation Counting, Pergamon Press, New York, 1964.

Blouke, M.M.; Janesick, J.R.; Elliot, T.; Hall, J.E.; Cowens, M.W.; May, P.J., "Current status of the 800 x 800 charge-coupled-device image sensor," Opt. Eng. 26, 864-874, 1987.

Boone, J.M.; Shaber, G.S.; Tecotzky, M., "Dual-energy mammography: A detector analysis," Med. Phys. 17, 665-675, 1990.

Boone, J.M., "Color mammography: Image generation and receiver operating characteristic evaluation," Investigative Radiology 26, 521-527, 1991.

Brettle, D.S.; Ward, S.C.; Parkin, G.J.S.; Cowen, A.R.; Sumsion, H.J., "A clinical comparison between conventional and digital mammography utilizing computed radiography," Br. J. Radiol. 67, 464-468, 1994.

Brisson, J.; Merletti, F.; Sadowsky, N.L.; Twaddle, J.A.; Morrison, A.S.; Cole, P., "Mammographic features of the breast and breast cancer risk," Am. J. Epidem. 115, 428-437, 1982.

Bunch, P.C., "Detective quantum efficiency of selected mammographic screen-film combinations," SPIE 1090, 67-77, 1989.

Carumbaya, K.D.; Albert, M.; Maidment, A.D.A., "Digital angiography of the breast," Abstract, Med. Phys. 23, 1107, 1996.

Chan, H.P. and Doi, K., "Studies of x-ray energy absorption and quantum noise properties of x-ray screens by use of Monte Carlo simulation," Med. Phys. 11, 37-46, 1984.

Chan, H.P.; Niklason, L.T.; Ikeda, D.M.; Lam, K.L., "Digitization requirements in mammography: Effects on computer-aided detection of microcalcifications," Med. Phys 21, 1203-1211, 1994.

Chan, H.P.; Vyborny, C. J.; MacMahon, H.; Metz, C.E., Doi, K., Sickles, E.A., "Digital mammography: ROC studies of the effect of pixel size and unsharp-mask filtering on the detection of subtle microcalcifications," Investigative Radiology 22, 581-589, 1987.

Cheung, L.; Coe, R., "Full-field, single exposure digital mammography," Medical Electronics, 13-21, October, 1995.

Choi, W.; Jing, Z.; Walker, J.K., "A high resolution digital x-ray imaging system based on scintillating plastic microfiber technology," SPIE 2163, 150-157, 1994.

Chotas, H.G.; Floyd, C.E. Jr; Ravin, C.E., "Technical evaluation of a digital chest radiography system that uses a selenium detector," Radiology 195, 264-270, 1995.

Court, L.E.; Speller, R., "A multiparameter optimization of digital mammography," Phys. Med. Biol. 40, 1841-1861, 1995.

Cowen, A.R.; Brettle, D.S.; Coleman, N.J.; Parkin, G.J.S., "A preliminary investigation of the imaging performance of photostimulable phosphor computed radiography using a new design of mammographic quality control test object," Br. J. Radiol. 657, 528-535, 1992.

Cunningham, I. A.; Westmore, M. S.; Fenster, , "A spatial-frequency dependent quantum accounting diagram and detective quantum efficiency model of signal and noise propagation in cascaded imaging systems," Med. Phys. 21, 417-427, 1994.

Dainty, J.C.; Shaw, R., Image Science, Academic, New York, 1974.

Dance, D.R.; Day, G. J., "The computation of scatter in mammography by Monte Carlo methods," Phys. Med. Biol. 29, 237-247, 1984.

Dance, D.R.; Persliliden, J.; Carlsson, G.A., "Calculation of dose and contrast for two mammographic grids," Phys. Med. Biol. 37, 235-248, 1992.

Desponds, L.; Despeursinge, C.; Grecescu, M.; Hessler, C.; Samiri, A.; Valley, J.F., "Influence of anode and filter material on image quality and glandular dose for screen-film mammography," Phys. Med. Biol. 36, 1165-1182, 1991.

Dick, C.E.; Motz, J.W., "Image information transfer properties of x-ray intensifying screens in the energy range from 17 to 320 keV," Med. Phys. 20, 1013-1021, 1993.

Dillon, P.L., Hamilton, J.F., Rabbani, M.; Shaw, R.; Van Matter, R.L., "Principles governing the transfer of signal modulation and photon noise by amplifying and scattering mechanisms," Proc. Soc. Photo. Instrum. Eng. 535, 130-139, 1985.

Drangova, M.; Rowlands, J.A., "Optical factors affecting the detective quantum efficiency of radiographic screens," Med. Phys. 13(2)150-157, 1986.

Eriksson, L.A., Tsai, C.M., Cho, Z.H., "Comparative studies of plastic scintillators - Applications to low energy high rate photon detection," Nuclear Instruments and Methods 122, 373-376, 1974.

Fahrig, R.; Maidment, A.D.A.; Yaffe, M.J., "Optimization of peak kilovoltage and spectral shape for digital mammography," SPIE 1651, 74-83, 1992.

Fahrig, R.; Mainprize, J.G.; Robert, N.; Rogers, A.; Yaffe, M.J., "Performance of glass fiber antiscatter devices at mammographic energies," Med. Phys. 21, 1277-82, 1994.

Fahrig, R.; Rowlands, J.A.; Yaffe, M.J., "X-ray imaging with amorphous selenium: Detective quantum efficiency of photoconductive receptors for digital mammography," Med. Phys. 22, 153-160, 1995.

Fahrig, R.; Yaffe, M.J., "A model for optimization of spectral shape in digital mammography," Med. Phys. 21, 1463-1471, 1994a.

Fahrig, R.; Yaffe, M.J., "Optimization of spectra shape in digital mammography: Dependence on anode material, breast thickness, and lesion type," Med. Phys. 21, 1473-1481, 1994b.

Feig, S.A.; Hendrick, R.E., "Risk, benefit, and controversies in mammographic screening," Syllabus: A Categorical Course in Physics Technical Aspects of Breast Imaging, RSNA Publications, Oakbrook, IL, 103-118, 1992.

Feig, S.A., "Mammographic evaluation of calcifications," Syllabus: A Categorical Course in Physics Technical Aspects of Breast Imaging, RSNA Publications, Oakbrook, IL, 93-105, 1995.

Feig, S.A.; Yaffe, M.J.; Plewes, D.B.; Maidment, A.D.A.; Jong, R.A., "Clinical evaluation of a scanned-slot, full-field digital mammography system," Proceeding of the Third International Workshop on Digital Mammography, Elsevier Science B.V., Amsterdam, The Netherlands, 71-79, 1996.

Fewell, T.R.; Shuping, R.E., Handbook of Mammographic X-ray Spectra, DHEW Publ. FDA. 79-8071, U.S. GPO, Washington, D.C., 1978.

Gagne, R.M.; Jafroudi, H.; Jennings, R.J.; Fewell, T.R.; Quinn, P.W.; Artz, D.E.S.; Vucich, J.J.; Freedman, M.T.; Mun, S.K., "Digital mammography using storage phosphor plates and a computer-designed x-ray system," Proceeding of the Third International Workshop on Digital Mammography, Elsevier Science B.V., Amsterdam, The Netherlands, 133-137, 1996.

Gambaccini; Marziani, M.; Rimondi, O., "Phantoms and dynamic range in mammography," Radiation Protection Dosimetry 49, 187-191, 1993.

Giger, M.L.; Doi, K., "Investigation of basic imaging properties in digital radiography. 1. Modulation transfer function," Med. Phys. 11, 287-295, 1984.

Giger, M.L., "Computer-aided diagnosis," Syllabus: A Categorical Course in Physics Technical Aspects of Breast Imaging, RSNA Publications, Oakbrook, IL, 257-270, 1992.

Ginzburg, A. and Dick, C.E., "Image information transfer properties of x-ray fluorescent screens," Med. Phys. 8, 337-346, 1981.

Gluer; D., Graeff, W.; Kupper, W.; Stellmaschek, K.H., "A fast low-noise line scan x-ray detector," Med. Phys. 16, 98-104, 1989.

Gravelle, I.H.; Bulstrode, J.C.; Bulbrook, R.D.; Wang, D.Y.; Allen, D.; Hayward, J.L.; "A prospective study of mammographic parenchymal patterns and risk of breast cancer," Br. J. Radiol. 58, 487-491, 1986.

Groot, P.M., "Image intensifier design and specifications," Specification, Acceptance Testing and Quality Control of Diagnostic X-ray Imaging Equipment, Proceedings of the 1991 AAPM Summer School, Santa Cruz, CA, 477-510, 1991.

Hammerstein, G.R.; Miller, D.W.; White, D.R.; Masterson, M.E.; Woodard, H.Q.; Laughlin, J.S., "Absorbed Radiation Dose in Mammography," Radiology 130: 485-491, 1979.

Haus, A.G., "Recent advances in screen-film mammography," Radiologic Clinics of North America 25, 913-927, 1987.

Haus, A.G., "Screen-film image receptors and film processing," Syllabus: A Categorical Course in Physics Technical Aspects of Breast Imaging, RSNA Publications, Oakbrook, IL, 69-84, 1992.

Henry, J. M.; Yaffe, M.J.; Pi, B.; Venzon, J.; Augustine, F.; Tumer, T.O., "Solid state x-ray detectors for digital mammography," SPIE 2432, 392-401, 1995.

Higashida, Y.; Moribe, N.; Morita, K.; Katsuda, N.; Hatemura, M.; Takada, T.; Takahashi, M.; Yamashita, J., "Detection of subtle microcalcifications: Comparison of computed radiography and screen-film mammography," Radiology 183, 483-486, 1992.

Holdsworth, D.W.; Gerson, R.K.; Fenster, , "A time-delay integration charge-coupled device camera for slot-scanned digital radiography," Med. Phys. 17, 876-886, 1990.

Huda, W., Sourkes, A.M.; Bews, J.A.; Kowaluk, R., "Radiation doses due to breast imaging in manitoba: 1978-1988," Radiology 177, 813-816, 1990.

Hyman M.; Ryan, J.J., "Heavy elements in plastic scintillators," IRE Tran. Nuclear Science 4, 87-90, 1958.

Jackson, V. and Bassett, L., "Stereotactic fine-needle aspirations biopsy for nonpalpable breast lesions," AJR 154, 1196-1197, 1990.

Jafroudi, H.; Jennings, R.J.; Muntz, E.P.; Freedman, M.T.; Mun, S.K., "Multiparameter optimization of mammography with alternative x-ray sources," SPIE 2432, 126-131, 1995.

Jing, Z.; Choi, W.; Walker, J.K.; Huda, W., "Design of a high resolution digital imaging system for mammography," Presented at 1994 AAPM annual meeting, Abstract, Med. Phys. 21, 875, 1994.

Johns, P.C.; Drost, D.J.; Yaffe, M.J.; Fenster, A., "Dual-energy mammography: initial experimental results," Med. Phys. 12, 297-304, 1985.

Johns, P.C.; Yaffe, M.J., "Coherent scatter in diagnostic radiology," Med. Phys. 10, 40-50, 1983.

Johns, P.C.; Yaffe, M.J., "X-ray characterisation of normal and neoplastic breast tissues," Phys. Med. Biol., Vol. 32, No. 6, 675-695, 1987.

Junck, K.L.; DeAlmeida, A.; Rezentes, P.; Wu, X.; Barnes, G.T., "Scatter and grid performance in mammography," Presented at 1996 AAPM annual meeting. Abstract, Med. Phys. 23, 1116, 1996.

Karellas, A.; Harris, L.J., "Charge-coupled device detector: Performance considerations and potential for small-field mammographic imaging applications," Med. Phys. 19, 1015-23, 1992.

Karssemeijer, N.; Frieling, J.T.M.; Hendriks, J.H.C.L., "Spatial resolution in digital mammography," Investigative Radiology 28, 413-419, 1993.

Kato, H., "Photostimulable phosphor radiology design considerations," Specification, Acceptance Testing and Quality Control of Diagnostic X-ray Imaging Equipment, Proceedings of the 1991 AAPM Summer School, Santa Cruz, CA, 860-898, 1991

Kosanetzky, J.; Knoerr, B.; Harding, G.; Neitzel, U., "X-ray diffraction measurements of some plastic materials and body tissues," Med. Phys. 14, 526-532, 1987.

Krol, A.; Bassano, D.A.; Chamberlain, C. C.; Prasad, S. C., "Scatter reduction in mammography with an air gap," Med. Phys. 23, 1263-1270, 1996.

Krupinski, E.A. and Roehrig, H., "Comparison of digital x-ray cameras for stereotactic breast needle biopsy: An observer performance study," ," Proceeding of the 2nd International Workshop on Digital Mammography, Elsevier Science B.V., Amsterdam, The Netherlands, 191-197, 1994.

Kuhn H; Knupfer, W., "Imaging characteristics of different mammographic screens," Med. Phys. 19, 449-457, 1992.

Leliveld, C.J.; Maas, J.G.; Bom, V.R.; Eijk, C.W.E.van., "Monte Carlo modeling of coherent scattering: influence of interference," IEEE Trans. Nuc. Sc., 1995.

Logan, W.W. and Norlund, A.W., "Screen-film mammography technique: compression and other factors," Reduced Dose Mammography, New York: Masson, 415-431, 1979.

Ma, L.; Fishell, E.; Wright, B.; Hanna, W.; Allen, S.; Boyd, N.F., "A controlled study of the factors associated with failure to detect breast cancer by mammography," J. Natl. Can. Inst. 84, 781-785, 1992.

Macovski, A., Medical Imaging Systems, Prentice-Hall, Inc, Englewood Cliffs, NJ, 1983.

Maidment, A.D.A.; Yaffe, M.J.; Plewes, D.B.; Mawdsley, G.M.; Soutar, I.C.; Starkoski, B.G., "Imaging performance of a prototype scanned-slot digital mammography system," Proc. SPIE 1896, 93-103, 1993a.

Maidment A.D.A.; Fahrig, R.; Yaffe, M.J. "Dynamic range requirement in digital mammography," Med. Phys., 20(6)1621-1633, 1993b.

Maidment, A.D.A.; Yaffe, M.J., "Analysis of signal propagation in optically coupled detectors for digital mammography: I. Phosphor screens," Phys. Med. Biol. 40, 877-889, 1995.

Maidment, A.D.A.; Yaffe, M.J., "Analysis of signal propagation in optically coupled detectors for digital mammography: II. Lens and fibre optics," Phys. Med. Biol. 41, 475-493, 1996.

Mainprize, J.G.; Yaffe M.J., "The effect of phosphor persistence on image quality in digital x-ray scanning systems," SPIE Vol. 2708, 85-94, 1996.

Metz, C.E.; Doi, K., "Transfer Function Analysis of Radiographic Imaging Systems," Phys. Med. Biol., 24(6) 1079-1106, 1979.

Metz, C.E.; Vyborny, C.J., "Wiener spectra effects of spatial correlation between the sites of characteristic x-ray emission and reabsorption in radiographic screen-film systems," Phys. Med. Biol. 28, 547-564, 1983.

Muntz, E.P.; Fewell, T.; Jennings, R.; Bernstein, H., "On the significance of very small angle scattered radiation to radiographic imaging at low energies," Med. Phys. 10, 819-823, 1983.

Namito, Y.; Ban, S.; Hirayama, H., "LSCAT: Low-energy photon-scattering expansion for the EGS4 code," KEK Internal 95-10, National Laboratory For High Energy Physics, Japan, 1995.

Neitzel, U.; Maack, I.; Kohfahl, S.G., "Image quality of a digital chest radiography system based on a selenium detector," Med. Phys. 21, 509-16, 1994.

Nelson, W.R.; Hirayama, H.; Rogers, D.W.O., The EGS4 code system, SLAC-Report-265, Stanford Linear Accelerator Ceneter, Stanford, LA, 1985.

Nishikawa, R.M.; Mawdsley, G.E.; Fenster, A.; Yaffe, M.J., "Scanned-projection digital mammography," Med. Phys. 14, 5, 717-727, 1987.

Nishikawa, R.M.; Yaffe, M.J., "Signal-to-noise properties of mammographic film-screen systems," Med. Phys. 12, 32-39, 1985.

Nishikawa, R.M.; Yaffe, M.J., "Effect of finite phosphor thickness on detective quantum efficiency," Med. Phys. 16, 773-780, 1989.

Nishikawa, R.M.; Yaffe, M.J., "Effect of various noise sources on the detective quantum efficiency of phosphor screens," Med. Phys. 17, 887-893, 1990a.

Nishikawa, R.M.; Yaffe, M.J., "Model of the spatial-frequency-dependent detective quantum efficiency of phosphor screens," Med. Phys. 17, 894-904, 1990b.

Nuclear Enterprise Technology Inc., Table of physical constants of scintillator, Manmouth Junction, 1993.

Okumura, K.; Sato, H.; Hino, T.; Takagi, K., "Study of FOS (fiber-optic plate with scintillator. for digital x-ray imaging," Hamamatsu Photonics K.K., Electron Tube Center, Simokanzo, Toyooka, Japan, 1995.

Prior, F.W.; Channin, D.S.; King, S.H.; Schaller, M.; Koch, R.; Sperner, W.; Kenney, R., "High resolution digital mammography using DLMA^{TM} and CR: Preliminary results," Proceeding of the 2nd International Workshop on Digital Mammography, Elsevier Science B.V., Amsterdam, The Netherlands, 143-151, 1994.

Qian, W.; Clark, L., "Adaptive multiple nonlinear filter and wavelets for the enhancement of medical image," Med. Phys 22, 989, 1995.

Rabbani, M.; Matter, R.V., "Analysis of signal and noise propagation for several imaging mechanisms," J. Opt. Soc. Am. A 6, 1156-1164, 1989.

Rabbani, M.; Shaw, R.; Matter, R.V., "Detective quantum efficiency of imaging systems with amplifying and scattering mechanisms," J. Opt. Soc. Am. A 4, 895-901, 1987.

Rothenberg, L.N., "Exposures and doses in mammography," Syllabus: A Categorical Course in Physics Technical Aspects of Breast Imaging, RSNA Publications, Oakbrook, IL, 113-119, 1994.

Sandler, S.R.; Tsou, K.C., "Quenching of the scintillation process in plastic by organometallics," J. Phys. Chem. 68, 300-304, 1964.

Schmitt, E.L.; Threatt, B., "Tumor location and detectability in mammography screening," Am. J. Roentgenol. 139, 761-765, 1982.

Schmitt, E.L.; Wolverton, D.E.; Vyborny, C.J., "Computer-aided diagnosis in mammography," Syllabus: A Categorical Course in Physics Technical Aspects of Breast Imaging, RSNA Publications, Oakbrook, IL, 199-208, 1995.

Sickles, E.A., "Breast imaging: A view from the present to the future," Diagnostic Imaging Clin. Med. 54, 118-125, 1985.

Skubic, S.E.; Fatouros, P.P., "The effect of breast composition on absorbed dose and image contrast," Med. Phys. 16, 544-552, 1989.

Smith, R.A., "The epidemiology of breast cancer," Syllabus: A Categorical Course in Physics Technical Aspects of Breast Imaging, RSNA Publications, Oakbrook, Il, 7-20, 1995.

Swank, R.K., "Absorption and noise in x-ray phosphors," J. Appl. Phys. 44, 4199-4203, 1973.

Swank, R.K., "Measurement of absorption and noise in an x-ray image intensifier," J. Appl. Phys. 45, 3673-3678, 1974.

Tapiovaara, M. J.; Wagner, R. F., "SNR and DQE analysis of broad spectrum x-ray imaging," Phys. Med. Biol. 30, 519-529, 1985.

Tapiovaara, M.J.; Wagner, R.F., "A generalized detective quantum efficiency (DQE) approach to the analysis of x-ray imaging," Proc. Soc. Photo-Opt. Instrum. Eng. 454, 540-549, 1984.

Technical Data TI0997-2-89, Eastman Kodak Company, Rochester, NY, 1989.

Toker, E.; Piccaro, M. F., "Design and development of a fiber optic TDI CCD-based slot-scan digital mammography system," SPIE 2009, 246-252, 1993.

Trauernicht, D. P. and Van Metter, R.L., "Conversion noise measurement for front and back x-ray intensifying screens," SPIE 1231, 262-270, 1990.

Whitehouse, G. H. and Leinster, S. J., "The variation of breast parenchymal patterns with age," Br. J. of Radiol. 50, 315-318, 1985.

Wong, H.; Yao, Y.L.; Schlig, E.S., "TDI charge-coupled devices: Design and applications," IBM J. Res. Develop, 36, 83-106, 1992.

Workman, A.; Cowen, A.R., "Signal, noise, and SNR transfer properties of computed radiography," Phys. Med. Biol., 38, 1789-1808, 1993.

Wunderly, S.W.; Kauffman, J.M., "New quench-resistant fluors for liquid scintillation counting," Appl. Radiat. Isot. 41, 809-815, 1990.

Yaffe, M.J., "Digital mammography," Syllabus: A Categorical Course in Physics Technical Aspects of Breast, RSNA Publications, Oakbrook, IL, 245-255, 1992.

Yaffe, M.J., "Direct digital mammography using a scanned-slot CCD imaging system," Medical Progress through Technology 19, 13-21, 1993.

Yaffe, M.J., "Technical aspects of digital mammography," Proceeding of the Third International Workshop on Digital Mammography, Elsevier Science B.V., Amsterdam, The Netherlands, 33-41, 1996.

Yester, M.V.; Barnes, G.T.; King, M.A., "Experimental measurements of the scatter reduction obtained in mammography with a scanning multiple slit assembly," Med. Phys. 8, 158-162, 1981.

Zhou, X.; Gordon, R., "Detection of early breast cancer: An overview and future prospects," Clinical Rev. in Biomedical Eng., 17, 203-255, 1989.

Zwieg, H.J., "Detective quantum efficiency of photodetectors with some amplifying mechanism," J. Opt. Soc. Am. 55, 525-528, 1965.
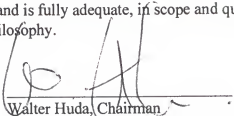
BIOGRAPHICAL SKETCH

The author finished his Bachelor of Science and Master of Science studies in nuclear physics from the Department of Engineering Physics, Tsinghua University, Beijing China. He worked as a R&D engineer for three years for China Nuclear Instrumentation & Equipment Cooperation, Beijing, China, before he was admitted into the medical physics program in the Department of Nuclear Engineering Sciences at the University of Florida in January, 1992. Since then, he has been working toward the doctoral degree. He worked on a research assistantship provided through the Department of Radiology from January, 1992 to August 1994. In August, 1994, he was offered a two years predoctoral fellowship to perform breast cancer research from the U.S. Army Medical Research And Development Command, receiving an exceptional evaluation score on his research proposal from a national scientific review panel. After passing the qualifying exam in April of 1995, he became an official Ph.D. candidate.

During the doctoral studies, he has nine published papers, one patent application, and eight presentations at national conferences. He received a student paper presentation award at the 1995 Florida Chapter of American Association of Physicists in Medicine annual meeting. One of his papers also received the Honorable Mention award at the 1996 SPIE Physics of Medical Imaging Conference.

He is a member of the American Association of Physicists in Medicine, and the IEEE Nuclear & Plasma Sciences Society.
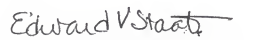
He is happily married to Guoying Qu, who always claimed to be his supervisor on his undergraduate thesis project. He is now in love with his son, Edward Xiaoshan Jing, born on February 4, 1996.

I certify that I have read this study and that in my opinion it conforms to acceptable standards of scholarly presentation and is fully adequate, in scope and quality, as a dissertation for the degree of Doctor of Philosophy.

Walter Huda, Chairman
Associate Professor of Nuclear and
Radiological Engineering

I certify that I have read this study and that in my opinion it conforms to acceptable standards of scholarly presentation and is fully adequate, in scope and quality, as a dissertation for the degree of Doctor of Philosophy.

Edward V. Staab, Cochair
Professor of Nuclear and Radiological
Engineering

I certify that I have read this study and that in my opinion it conforms to acceptable standards of scholarly presentation and is fully adequate, in scope and quality, as a dissertation for the degree of Doctor of Philosophy.

Raymond E. Andrew
Professor of Physics

I certify that I have read this study and that in my opinion it conforms to acceptable standards of scholarly presentation and is fully adequate, in scope and quality, as a dissertation for the degree of Doctor of Philosophy.
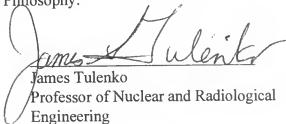
Janice C. Honeyman
Associate Professor of Computer and
Information Science and Engineering

I certify that I have read this study and that in my opinion it conforms to acceptable standards of scholarly presentation and is fully adequate, in scope and quality, as a dissertation for the degree of Doctor of Philosophy.

Thomas Mareci
Associate Professor of Physics

I certify that I have read this study and that in my opinion it conforms to acceptable standards of scholarly presentation and is fully adequate, in scope and quality, as a dissertation for the degree of Doctor of Philosophy.

James Tulenko
Professor of Nuclear and Radiological Engineering

This dissertation was submitted to the Graduate Faculty of the College of Engineering and to the Graduate School and was accepted as partial fulfillment of the requirements for the degree of Doctor of Philosophy.

May, 1997

Winfred M. Phillips
Dean, College of Engineering

Karen A. Holbrook
Dean, Graduate School